ABSTRACT

Title of dissertation: APPLICATION OF POROUS SILICON
IN TERAHERTZ TECHNOLOGY

Shu-Zee Alencious Lo,
Doctor of Philosophy, 2010

Dissertation directed by: Professor Thomas E. Murphy
Department of Electrical and
Computer Enginering

In this thesis, we discuss our efforts in developing porous silicon based devices for terahertz signal processing. In the first stage of our research, we demonstrate that porous silicon samples fabricated from highly doped p-type silicon can have adjustable refractive indices ranging from 1.5-2.1 and can exhibit a resistivity that is four orders of magnitude higher than that of the silicon wafer from which they were made. We show that the porous silicon becomes stable and relatively lossless after thermal oxidation. The partially oxidized porous silicon is shown to exhibit a smooth absorption spectrum, with low absorption loss of < 10 cm^{-1} over the entire terahertz spectrum.

As a proof of concept, we fabricated, for the first time, a porous silicon based multilayered Bragg filter with reflectance of 93% and full-width at half-maximum bandwidth of 0.26 THz. Compared with other multilayered filtering techniques, porous silicon has the advantage that it can be easily fabricated, and offers the possibility of forming multilayer and graded index structures for more advanced

filters. The large surface area of nanoporous silicon makes it an especially attractive platform for applications in biochemical detection and diagnostics

As part of our effort in developing terahertz waveguide for biosensing, we reported the world's first porous silicon based terahertz waveguide using the principle of surface plasmon polaritons. The effect of porous silicon film thickness on the propagation of surface plasmons is explained theoretically in this thesis and is found to be in good agreement with experimental results.

APPLICATION OF POROUS SILICON IN TERAHERTZ TECHNOLOGY

by

Shu-Zee Alencious Lo

Dissertation submitted to the Faculty of the Graduate School of the
University of Maryland, College Park in partial fulfillment
of the requirements for the degree of
Doctor of Philosophy
2010

Advisory Committee:
Professor Thomas E. Murphy, Chair/Advisor
Professor Chi H. Lee
Professor Robert W. Gammon
Professor Howard Milchberg
Professor Isaak D. Mayergoyz

Acknowledgments

I owe my gratitude to all with whom I was fortunate to interact and work during this important time of my life. Without all the comments, suggestions and help from all of them, this research would not be possible.

First and foremost, I owed my greatest gratitude to my advisor, Professor Thomas E. Murphy for providing me the opportunity for working on an exciting and interesting project. I learned so much from the helpful discussions I had with him that I will be forever in debt to him. The friendly and yet challenging research environment he had created helped shape me into the professional I always wished to be.

I am in debt to my thesis committee members, Professor Chi H. Lee, Professor Howard Milchberg, Professor Robert Gammon, Professor Isaac D. Mayergorz for their helpful discussions and comments on this thesis. In particular, I am greatly in debt to Professor Chi H. Lee for his generous support with laboratory equipment. Without his help, this research would not be possible.

I would like to thank my colleagues, Dr. Paveen Apiratikul, Dr. Andrea M. Rossi, Dr. Zhifu Liu, Sina Firouzabadi, Dr. Reza Salem, Ehren Huang for their helpful discussions, encouragement, and assistance. In particular, Dr. Andrea M. Rossi gave very helpful advice on porous silicon fabrication and Ehren Huang for the helpful discussions on surface plasmon. Dr. Paveen Apiratikul, Dr. Zhifu Liu, Sina Firouzabadi and Dr. Reza Salem for the wonderful and friendly interaction. They made me feel right at home when the home is far away.

Table of Contents

List of Tables

List of Figures

Chapter 1

Introduction

The terahertz region of the electromagnetic spectrum, also known as the terahertz gap is relatively unexplored. In Sec. 1.1, we discuss problems with using conventional electronics and optical techniques to generate, detect and manipulate radiation in this uncharted spectrum. Only in recent years with advances in femtosecond laser pumped time domain terahertz spectroscopy has research in this spectrum becomes popular.

Porous silicon has proved to be an interesting optical material for near and mid infrared applications for its potential in filtering and biochemical sensing application. It is hence interesting to see if porous silicon could be used as an optical material in the terahertz spectrum. In Sec. 1.1, we give a brief literature review on the current trends and status of terahertz technology with a focus on passive filtering. Later in Sec. 1.1, we introduce the terahertz spectroscopy system that we constructed for all the research conducted for this thesis. In Sec. 1.2, we discuss the general properties of porous silicon and our fabrication setup for porous silicon used in this research work.

1.1 Terahertz spectroscopy

1.1.1 Current status

The terahertz spectrum conventionally refering to the wavelength range from 10 μm to 1 mm has been gathering much interest recently for its potential applications in imaging [1–3], spectroscopy [2] and communication [2, 4]. While sources such as GUNN diodes, electronic frequency multipliers, IMPATT diodes, back wave oscillators [2, 4–6] are able to generate up to hundreds of mW in hundreds of gigahertz regime, it is often hard to scale the output frequency of these devices higher due to limitation of RC time constants, carrier transit times and other parasitic effects [5]. On the other end of the spectrum, quantum cascade lasers are able to generate down to a few terahertz but are facing difficulty operating at lower frequency and at room temperature due to phonon absorption [5, 7]. In the important range of 1-3 THz, pulsed terahertz systems pumped by femtosecond lasers remain the most practical method performing terahertz spectroscopy [3, 7].

The pioneering work on pulsed terahertz systems began with photoconductive switching [8–10]. It was found that the transient photoconductive respondse in these devices can be radiated out and be detected as picosecond electromagnetic pulses [11–13]. Therefore by using a pair of photoconductive switches, one biased with external electric DC voltage as the source, the other unbiased as the detector, a terahertz signal can be generated and detected. Nonlinear optical effects are also used for generating and detecting terahertz radiation. One popular scheme is to utilize the optical rectification effect in a second-order nonlinear crystal such as ZnTe to generate electromagnetic pulses with frequencies extending into the terahertz regime and then the electrooptic effect in a second ZnTe crystal for detection [14, 15].For the experiments reported here, we built a hybrid system with a semiconductor (InAs) as source for THz generation and E-O detection with a 1 mm thick $\langle 110 \rangle$-oriented ZnTe crystal. In this scheme, the terahertz pulse is generated by the photo-Dember effect at the surface of InAs wafer [16], and detected using the electrooptic effect

2

in ZnTe.

In the field of spectroscopy, pulsed THz systems allow a few advantages compared with competing technologies such as FTIR. A signal to noise ratio (SNR) as high as 10^7 can be achieved in these systems by using lock-in amplification. Pulsed THz systems can generate broad THz bandwidth at once, hence allowing detection of large amount of spectral information in a single scan [17–20]. It has been suggested that THz spectroscopy could be used to study biomolecular interactions because many biological and chemical molecules are known to exhibit macromolecular resonance behaviors in the THz region [21]. Furthermore, materials that are dry, nonpolar and insulating are relatively transparent in the THz domain. Combining transparency with the relatively harmless nonionizing characteristic of these sources allows the possibility of replacing X-rays as imaging sources in airport security scanning or medical diagnostics [1, 22].

1.1.1.1 Passive filtering of terahertz spectrum

In order to control and manipulate terahertz waves, it is obvious that manipulation devices that either actively switch, redirect the terahertz frequency or simple passive devices such as filter or waveguides are needed. Due to the long wavelength, low power and broad spectrum of commonly used terahertz sources, most conventional technique that are used in the optical and microwave technologies does not translate well to the terahertz spectrum. Acousto-optics, a commonly used technique that allow the steering or switching of optical signal is inefficient in the terahertz spectrum due to the f^2 dependent of the conversion efficiency on the frequency of the targeted signal [23]. Optical filtering technologies, conventionally based on the thin film vacuum deposition do not translate well due to the longer deposition time and the required thickness of the filter layers [24]. Conventional manufacturing techniques, used commonly for fabrication of microwave filters and cavities is hard to miniaturize. Conventional microwave waveguides are also difficult to realize due to the modal dispersion in the broad terahertz spectrum associated with pulsed terahertz

spectroscopy system [25]. Hence it is obvious that there are huge research opportunities to develop devices in the terahertz spectrum. In this sub-section, we will briefly review the current terahertz passive filtering technologies that have been reported. Active filtering technologies that modulating or switching terahertz signals, often based on photonics crystals [26–38], plasmonics [39–43] and metamaterials [44–48] technologies are outside the scope of this thesis and are not be discussed.

Powder scattering   Scattering from finely ground powder had been used as a low pass filter [49, 50]. At wavelengths far beyond the powder size, the medium acted like an effective medium and the losses are due to Rayleigh, Mie scattering or phonon absorption. As a wavelength approaches or below the powder particle size, the input electromagnetic wave would be diffracted by the powder, hence the medium becomes opaque to the electromagnetic wave of comparable wavelength or smaller then the mean size of the powder. This method had been used to filter out wavelength up to tens of microns, but for very large wavelengths, such as in the subterahertz, the size of the filter becomes unacceptable. Furthermore, this method only serves as a high-pass filter.

Reststrahlen zone of crystals   The Reststrahlen zone of biatomic crystals could be used for filtering terahertz signal [49, 51]. In the frequency range in between transverse optical frequency and longitudinal optical frequency of the crystal, the dielectric function becomes negative and hence the complex refractive index would becomes pure imaginary which causes reflection coefficient to have the magnitude of 1. Hence with a small oscillation damping in the crystal, the reflectivity of the crystal in this frequency range is very close to 100%. The obvious disadvantages of this method is that the reflected spectrum of the crystals depends on the material, and is not flexible. While the performance of these crystals could be improved with multilayered coatings, in general the ability to control the reflection spectrum is limited by the composition of the films that are used.

Photonic crystals   Photonic crystals have been utilized for terahertz filtering application. One dimensional photonic bandgap materials can be regarded as a multilayered structure in general and be analyzed as such [52, 53]. Two dimensional photonic bandgap materials for terahertz frequency are usually realized by patterning microscopic rods in the arrangement that mimic a conventional crystalline structure [54–59]where the photonics bandgap of the artificial crystal could be adjusted to exhibit reflection in targeted wavelength. Furthermore, by introducing defects in an otherwise periodic structure, one can construct waveguides and resonant cavities [57]. The fabrication of three dimensional photonic crystals for terahertz applications is considerably more complicated, but has been reported by locally laser heating and melting of plastic balls coated with metal or by etching lithographically patterned silicon wafers [60–62].

Periodic corrugated surface for filtering   Periodic planar structures are also developed for terahertz or far-infrared filter. The key advantages for these structures in comparison to multilayered structures is the relatively small thickness of such structures. Depending on the principal of operation, these structures could be grouped into different categories:

1. Plasmonic devices that typically consist of semiconductor or metal with corrugated grating structures patterned on transparent substrate [63–67]. When a terahertz wave impinges on a grating with subwavelength aperture(at normal incidence), the aperture diffracts the incident terahertz wave to broad angle. The scattered terahertz wave is then coupled to the surface plasmon mode of the conductor and is interfered by the grating. The resultant filtering behavior is determined by the periodicity of the grating. Pulse shaping of terahertz wave by plasmonic devices had been demonstrated by adjusting grating spacing [63].

2. Frequency selection structure consisting of metallic wire mesh [68–72] or periodic hole structures on a substrate. Depending on the desired filter application, different hole cell shape are used. While these devices have similar structure as plasmonic

5

devices that is described previously, these devices typically have dimension similar to the wavelength of the filtered terahertz signal, hence are explained by waveguiding and diffraction effects to the input terahertz beam. For circular [73–75], cross shape [75–81] and hexagonal holes [82] in a conductive film, the hole acts as short waveguide with cutoff frequency that limits the transmission at low frequency. At high frequency, diffraction due to the periodic geometry can introduce transmission loss and the higher frequency transmission(or zero-order diffraction) would settle at what is dictated by the fill factor. Better performance can be achieved by sequentially cascading more than one filter [75, 82]. For the same targeted frequency, the circular hole patterns have been shown to yield sharper low frequency cut off while cross shape patterns offer a narrower and more symmetric transmission window. Rectangular and I shaped slots [83, 84] are used as a notch filter . These filters have been used for rejecting undesired higher harmonics from subterahertz electronics frequency multipliers.

3. Planar metamaterials are comprised of either complete rectangular and circular rings [85, 86] on a metallic sheet [87–90]. These devices can be described by an electronic RLC circuit with transmission peak at the resonance frequency of the corresponding RLC circuit. A split ring resonator could be made as negative refractive index metamaterial. An ordinary split ring resonator, which is comprised of a metallic ring with gaps surrounded by dielectric is used to introduce a resonance peak while complementary split ring resonator which is comprised of dielectric gapped rings surrounded by metal is used to introduce an absorption peak [87].

Multilayered filtering   The principle of multilayered filtering is simple: by stacking multiple layered of materials with different indices with appropriate thickness, the transmitted spectrum will be filtered by interference between electromagnetic waves that are partially reflected and transmitted at each dielectric interface. The technique is attractive because of

6

the analytical solution it provides and the flexibility of filter design.

At terahertz frequencies, one important use of such technology is in developing good antireflection coatings for optical elements. By attaching a material of optical thickness $\frac{\lambda}{4}$ that has the refractive index close to the geometric mean of the two materials, the incoming electromagnetic wave would interfere in such a way that the reflection is minimized, while transmission is maximized. Such coating is particular important for terahertz applications, because many THz materials have high refractive index which leads to high reflection losses. Different variety of plastics and fused silica had been used for terahertz antireflection coatings, with excellent results. In some cases [49, 91], a thin sheet of plastic is put onto the optical component by vacuum suction to remove air bubbles follows by a heat treatment to attach the plastic sheet on the component. In other cases, direct vacuum deposition had been attempted [92, 93], however this method is limited to plastics that can be readily deposited. It is also possible to simply glue and machine the plastic material or fused silica [94–96] to the optical component but such methods are cumbersome, time-consuming, and ill-suited for large-scale manufacturing.

More sophisticated terahertz filters require multiple dielectric layers, one common method is to assemble polished float zone silicon wafers with air gaps created by inserting spacers in between wafers [53, 97–100]. This method works excellently in the low frequency regime due to the high refractive index contrast between silicon (n=3.4) and air (n=1), however such method is often time consuming and expensive, as the need for the slow polishing process and the need for precise micron-level machining of the spacer and the overall alignment precision. Furthermore, the method is difficult to scale to higher frequencies, because the thin free-standing silicon layers become fragile and difficult to handle. Vacuum deposition of fused silica and hydrogenated amorphous silicon had also been reported [101], and such technique have the advantage that the refractive index can be adjusted by controlling the film deposition parameters, but the slow vacuum deposition rate limits the use of such technique to relatively high frequency range. Ceramics of various kind [52, 102, 103]

had been found to work well. The advantages of Ceramic is in the possibility of mixing ceramic composites to achieve a variety of refractive indices, optimized for low loss. However, the inaccuracy of tape casting and the high scattering loss often plague ceramics at higher frequencies.

Kutz and Mittleman's groups had performed extensive research on polymer multilayer terahertz filters. Polymer stack [104] can be fabricated in a flexible, bendable form, which is important in certain consumer applications. However the low index contrast[1] means that many layers have to be stacked to achieve similar performance as that obtained with silicon and air gaps. In another experiment [105, 106], silicon wafer is placed in between polymer layer to improve the index contrast but with disadvantages of sacrificing the flexibility of polymer films. Polymer layers incorporating high refractive index ceramic nanoparticles [107, 108] have been successfully used to improve the refractive index contrast while retaining the advantages of a flexible substrate. Shao et al. [109] deposited ZnS coating on polymer sheet. As with other deposition methods, the vacuum deposition allows scalability to high frequency but is impractical for low frequency application.

In this work, we use porous silicon fabricated by electrochemical etching of silicon as a material for constructing multilayer terahertz filters. This approach has the intrinsic advantages that the filter is fabricated from the same piece of silicon wafer, which dramatically simplifies the construction by eliminating the need for thick film deposition or layer assembly. By changing the applied current, etchant concentration and substrate doping, it is also possible to change the refractive index of the porous silicon layer. Such flexibility in refractive indices allows complicated refractive index distribution and even graded index structures to be easily made. Table 1.1 shows summarizes the prior research on terahertz multilayered filter.

---

[1]polymers are typically constrained to have a refractive index between 1.5 and 2

Method	$\frac{n_H}{n_L}$	n tunability	Low frequency scalability	High frequency scalability	Fabrication complexity	Unique features
glue and polish fused silica on Ge (antireflection coating) [95, 96]	—	fixed	✓	✓	easy	—
PECVD of a-Si[H] and SiO$_2$ [93, 101]	$\frac{3.7}{2}$	2-3.4	✗	✓	easy	Could be applied to curved surface
Polymer (antireflection coating) [49, 91, 92, 94]	—	fixed	✓	✓	mixed	Could be applied to curved surface
Ceramic	$\frac{10.6}{3.4}$ [102], $\frac{4.8}{2.1}$ [52], $\frac{4.16}{3.17}$ [103]	fixed	✓	✗	complicated	—
Polymer + ZnS coating [109]	$\frac{3.0}{1.5}$	fixed	✗	✓	complicated	—
Polymer + nanoparticle [107, 108]	$\frac{3.5}{1.5}$	3.0-3.5	✓	✗	complicated	flexible
Polymer + Silicon wafer [105, 106]	$\frac{3.4}{1.5}$	fixed	✓	✗	complicated	—
Polymer only [104]	$\frac{1.8}{1.53}$	fixed	✓	✓	easy	flexible
Silicon with air gap [53, 97–100]	$\frac{3.4}{1}$	fixed	✓	✗	complicated	—
This work	$\frac{2.1}{1.5}$	1.5-2.1	✓	✓	easy	graded index possible

Table 1.1: Comparison between different multilayer filtering techniques in terahertz frequency

1.1.2 Experimental setup

A schematic diagram of our terahertz time domain spectroscopy setup is shown in Fig. 1.1. At the core of the THz setup is a Ti:Sapphire laser oscillator that generates pulses of 120 fs width at 810 nm with average power of 2 W and repetition rate of 82 MHz. This laser beam is then split into pump and probe beams with a 99:1 beamsplitter(BS). The higher intensity pump beam is then focused by a lens assembly L1 to a spot size of 1 mm onto the surface of a lightly doped p-type InAs wafer. A half-wave plate, HW is used to rotate the input polarization of the pump laser to TM polarization. The change of polarization was found to improve the generated THz power by a factor of 2, due to the difference in reflectivity between TE and TM polarization. On typical unbiased semiconductor, three effects can contribute to the THz generation. 1)Optical rectification, due to the second-order nonlinear susceptibility (χ_2), which depends on the crystal orientation and polarization state. 2) Acceleration of the photogenerated carriers by the built-in surface electric field. 3) Photo-Dember effects due to the discrepancy between the electron and hole mobilities. As shown by Ref. [110] of these three mechanisms, photo-Dember effect is found to be the dominant effects in InAs. The Terahertz pulse is generated and radiated from the wafer, then collimated and focused by off-axis parabolic mirrors pair GM1 and GM2. The polarization of the generated terahertz pulse, is found to be vertically polarized using a wire-grid polarized that is patterned on a ZnSe substrate. A 1.25 cm thick Teflon block is used to scatter and absorb the optical pump beam while transmitting the terahertz pulse. At the focal point of parabolic mirror GM2, where the sample is placed, the THz beam spot size is 1 mm. The attenuated and delayed THz pulse is then collected and focused by another parabolic mirrors pair (GM3 and GM4). A quarterwave plate QW is used to adjust the polarization of the probe beam such that it is circularly polarized. This circularly-polarized beam is then split into horizontal and vertically polarized beams by a Wollaston prism, W and differentially detected in a balanced photodiode pair. Since the intensities of both beams are the same, they generate the same photocurrent and hence the output of this detector pair is zero
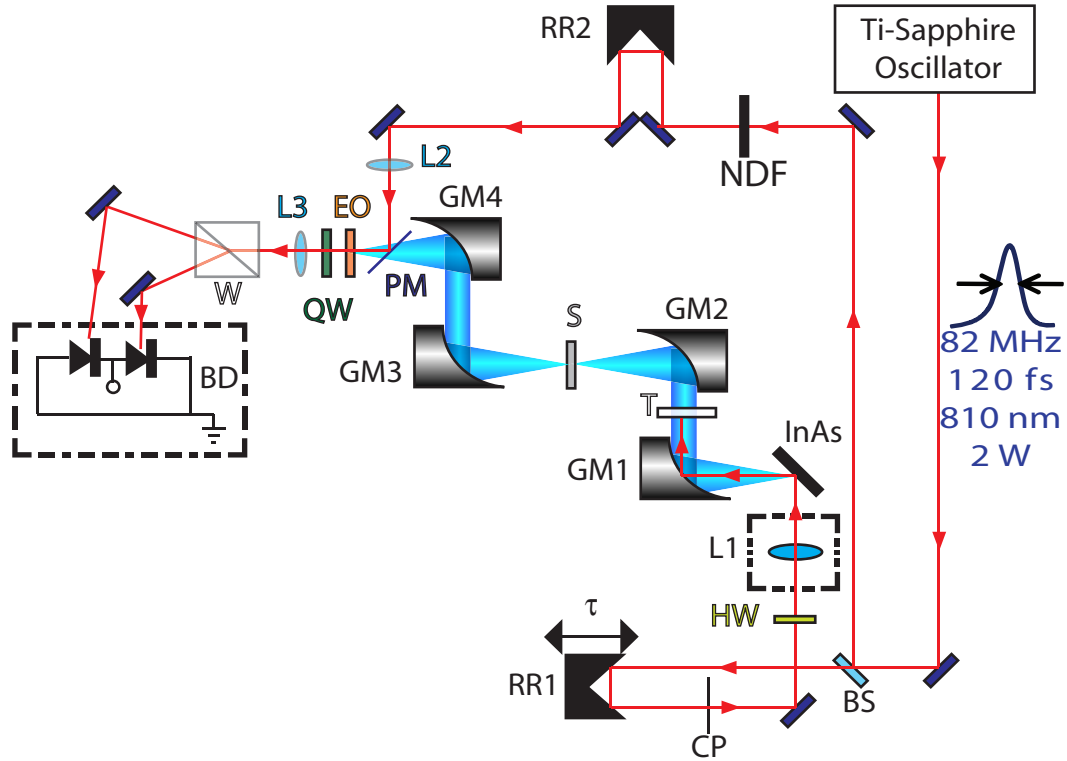
Figure 1.1: Transmissive THz setup. BS is a 99:1 beamsplitter, RR1 and RR2 are 1" retroreflectors, CP is a chopper blade that is set at 800 Hz, HW is a halfwave plate for 800nm, L1 is a lenses assembly to focus pump beam to 1 mm on InAs, GM1, GM2, GM3 and GM4 are f=2" off axis parabolic mirrors, InAs is a lightly doped p-type <100> InAs wafer, T is a 1.25cm thick Teflon block, S is the sample to be measured, NDF is a OD=1.5 neutral density filter, L2 is a f=100 mm focusing lens, PM is an uncoated pellicle mirror that has a splitting ratio of 92:8 at 632 nm, EO is the 1 mm <110> ZnTe EO crystal, QW is a quarterwave plate for 800 nm, L3 is a f=50 mm focusing lens, W is a wollaston prism and BD is a balanced silicon photodetector detector

under no THz field. In the presence of the THz field, the birefringence of the ZnTe crystal (EO) will be modified such that the two separately detected signals are no longer balanced and the differential current is linearly proportional in first order approximation to the THz field amplitude. Hence, with properly balanced photocurrent, we are able to detect the THz field distribution in time domain by scanning the delay between the probe beam and the THz beam. Fig. 1.2 shown a typical THz signal in the time domain and its corresponding frequency domain counterpart, calculated using the Fast Fourier transform(FFT).

Fig. 1.4, plots the peak terahertz signal and noise level as a function of the optical

11
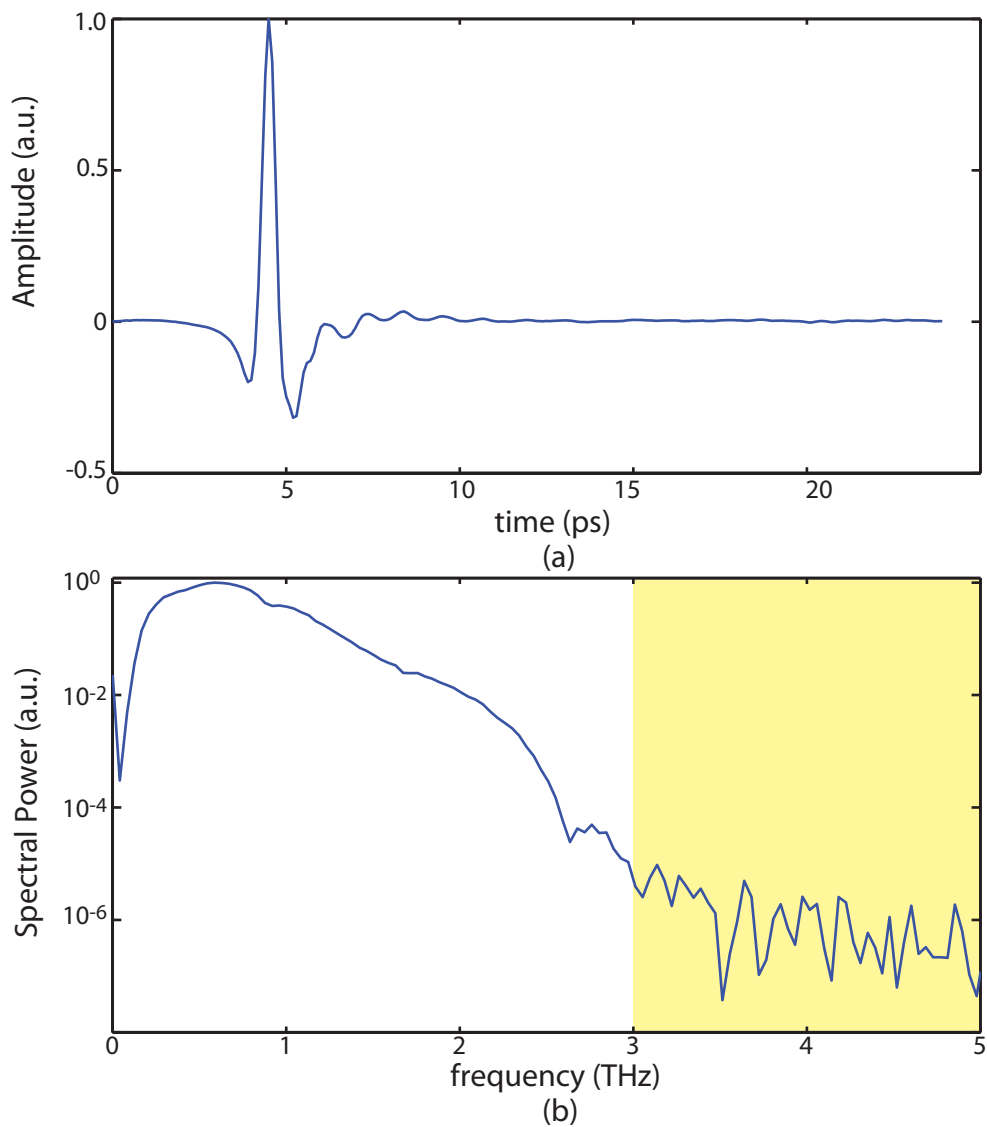
Figure 1.2: Typical THz signal generated from our setup.(a) THz signal without sample in Time domain. (b) The same THz signal in spectral domain. Yellow area illustrated the frequency below noise level.
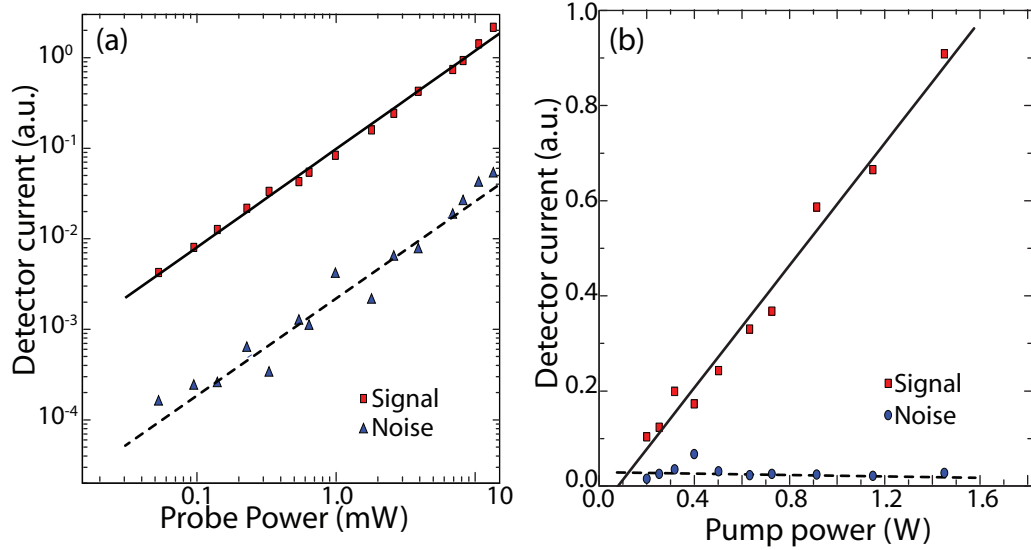
Figure 1.3: Comparison between signal and noise of the terahertz system. (a). Varied probe power with pump power held constant at 1.8 W. (b).Varied pump power with probe power fixed at 10 mW.

probe power and optical pump power. In each case, the noise was measured by observing the output photocurrent from the balanced photodiode prior to the arrival of the THz pulse. From the comparison between the varied pump power and varied probe power cases, the signal to noise of the system is sorely dependent on the pump power. One of the challenges faced by terahertz spectroscopy systems is the absorption caused by water vapor in the air.

Fig. 1.4 plots the measured absorption spectrum of water, obtained by comparing the transmitted THz spectrum under normal conditions to when the environment is purged with dry air. The whole setup is enclosed in an acrylic box with 15 mins dry air purging generated by drying compressed air with an $-40°F$ dew point commercial air dryer, Twin Tower HR3-12-058.

1.2   Porous silicon

Porous silicon is an interesting and versatile optical material that is fabricated by electrochemical etching of silicon. The pore size can be adjusted by changing the doping concentration of the starting silicon [112]. For highly/moderately doped p and n type silicon, the
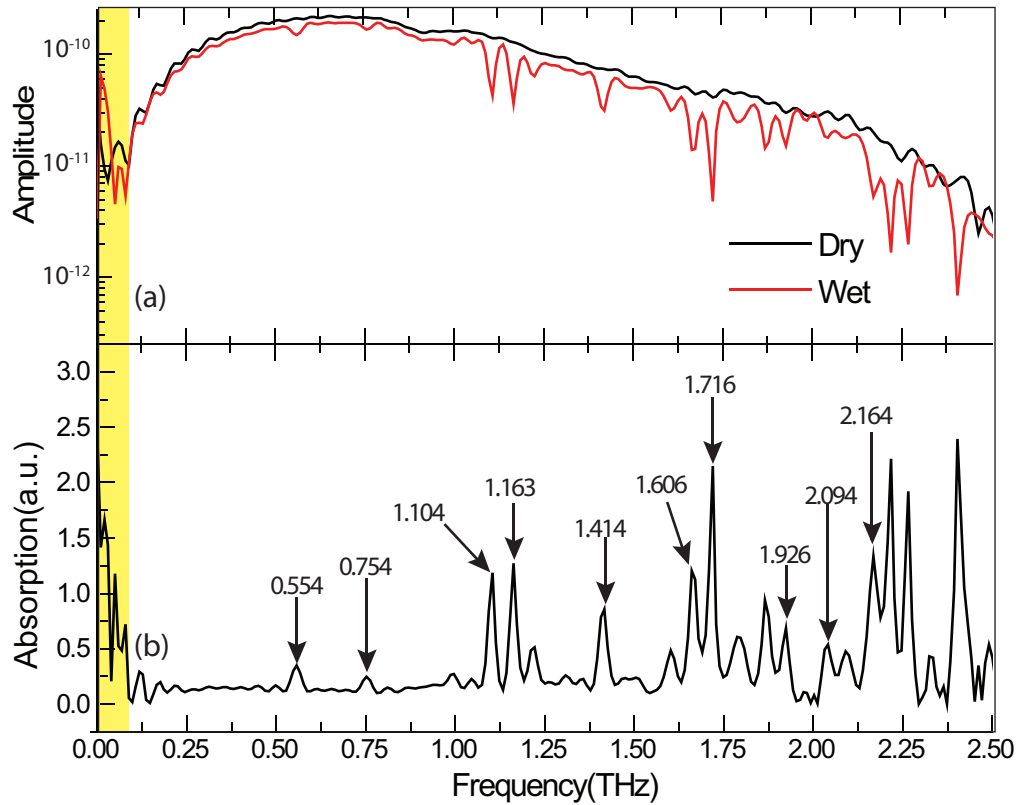
Figure 1.4: Water absorption peaks measured with our terahertz spectroscopy system.(a) Comparison between Fourier transformed terahertz trace measured in room environment and in dry compressed air.(b)The ratio of the two curves in (a). Known water absorption peaks from Ref. [111] are marked here.

pore size is in the range $10 - 100$ nm. For lightly doped p-type silicon, the pore size ranges $3 - 10$ nm and for lightly doped n-type silicon the pore size could be as large as microns. The reason for the variation in pore size is complicated with multiple possible hypothesis, but is believed to be related to the diffusion length of holes in the material [113]. The presence of electric holes in the starting silicon wafer is essential for the electrochemical etching process. In p-type silicon, the electric holes are naturally supplied by the dopants and are replenished by the applied current. In n-type silicon, optical illumination is often used to provide the required electric holes, hence by blocking the illuminating light with an optical mask laid on the silicon wafer by photolithography, one could fabricate the highly regular, high aspect ratio micron size pores [114, 115]. Nanoporous silicon has a very large internal surface area, and the ratio of the surface area to the volume can be as large as $200 - 500 \, \mathrm{m^2/cm^3}$. This makes porous silicon an attractive candidate for gas and humidity sensor application [116–119]. It is suggested that porous silicon is sensitive enough to be considered as a trigger for explosive [120, 121]. Because of its highly reactive nature, porous layers can be easily removed in basic solution such as KOH or NaOH [113, 122]. We take advantage of this feature to selectively etch the porous layers when characterizing the porosity and etch rate. This interesting property is also being explored for MEMS fabrication that often required high aspect ratio [123–125]. The surface could also be chemical activated by binding the surface molecules with biological or chemical reagent for biochemical sensing application as depicted in Fig. 1.5 [126–131].

An interesting property of the pore formation process, explained in subsection 1.2.1 is that the change in applied current affects only the porosity at the interface between porous silicon and bulk silicon. Using this unique property, it is possible to create complicated layered structures in porous silicon [132, 133]. As the applied current increased, not only does the etch rate increase but the porosity at the interface also increased. Hence according to the effective medium approximation [134, 135], a reduction of refractive index is seen. As the applied current could be modified on the fly, the porosity could varied either abruptly
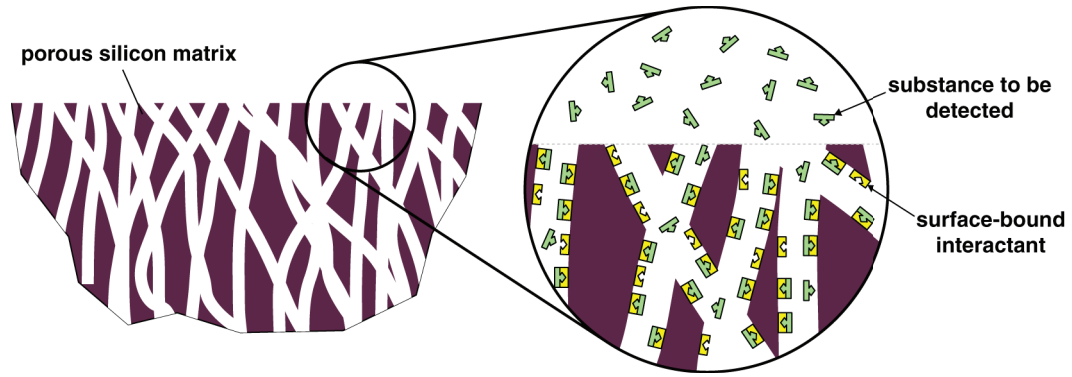
Figure 1.5: Biosensing with porous silicon.

or continuously [136–139] as depicted in Fig. 1.6. Typically, as we will see in Chap. 2 sub-Sec.2.1.1 , the porosity could be changed from $40-80\%$ and the resultant refractive index is adjustable from $1.5-2.1$.

The pore formation process also follows the crystalline structures of the starting silicon wafer [113]. In general, the pore formation usually follows the <100> axis of the silicon wafer. Hence pores formation on a <100> silicon would be perpendicular to the surface while pore formation on <111> wafer would aligned to the <100>axis and be at an angle to the surface. Such property is utilized for the creating of birefringent multilayered filters [140–142].

1.2.1   Fabrication process

The etching process of porous silicon [113, 122] is shown in the chemical formula in Fig. 1.7(a). The etchant used is usually concentrated hydrofluoric acid with ethanol for improving the etchant penetration into the pore. Without a supply of electric holes, the surface of the silicon is terminated by the Si-H bond formed from the hydrogen ions in the etchant. The introduction of holes supplied by the electric current breaks the Si-H bond and allow it to be replaced by Si-F bond, which is soluble in the etchant solution and combines with additional fluoride ions to become SiF_6^{-2} ions in the etchant. The mechanism by which columnar pores are formed is complicated with multiple hypotheses and hence will be ex-
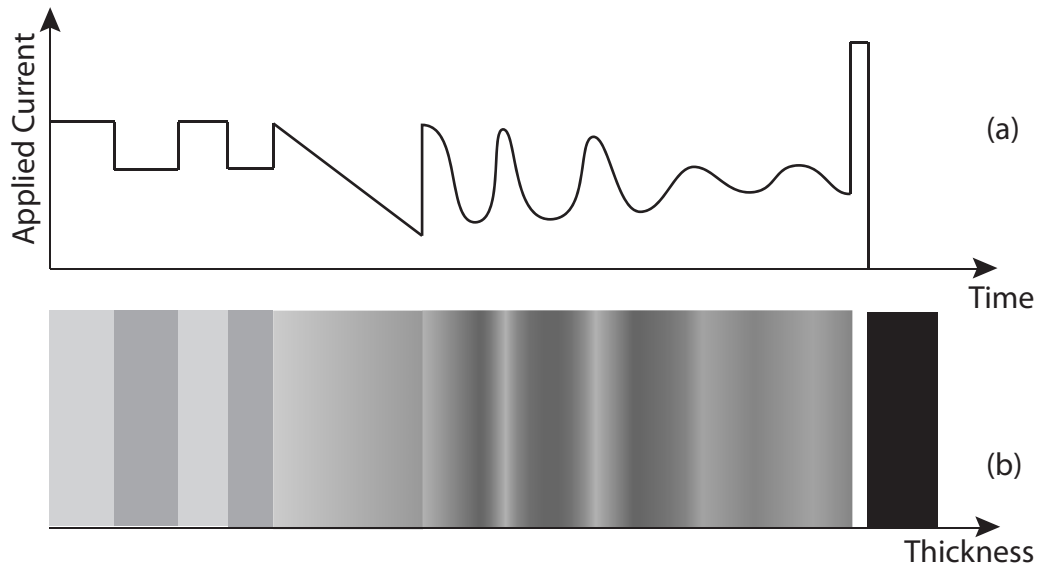
Figure 1.6: Variation in refractive index by changing the applied etching current. (a) applied current. (b) resultant porous silicon. The gray level of the sample illustrated the effective refractive index of the particular layer, with black being the refractive index of a bulk silicon and white being the refractive index of air.

plained here without the details. In the diffusion model, the formation of pore is illustrated in Fig. 1.7(b) [122]. At the tip of the pores, the incoming electric holes could either move to the etchant directly and participate in the chemical reaction or it could go through the porous silicon layer and react with the etchant later. Due to the increase of energy band gap by the formation of porous silicon, the holes has to overcome a potential barrier as it enter the porous silicon layer, while no such barrier from the bulk silicon to the etchant directly. Hence the majority of the holes would enter the the etchant directly, ensuring the propagation of pores.

The applied current and the concentration of the etchant solution obviously affect the etching process. The IV curve [113] shown in Fig. 1.8(a) gives information on the etching process. For low applied current, the etching is dominately toward the inside of the wafer with an increased of applied current increases the porosity of the porous silicon but maintains the pore size until the turning point that marks the beginning of transition region B. At the transition region, the etching begins to spread sidewise resulting in a broadening of the pore. As the current increases further, eventually the I-V curve reaches a peak at

17
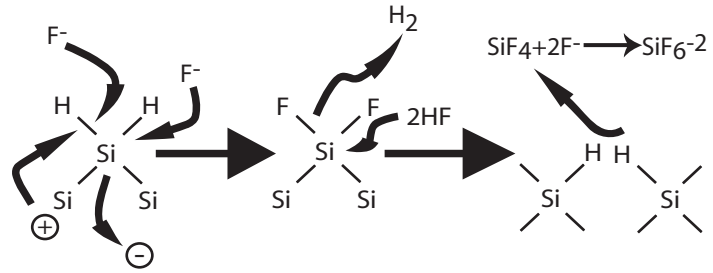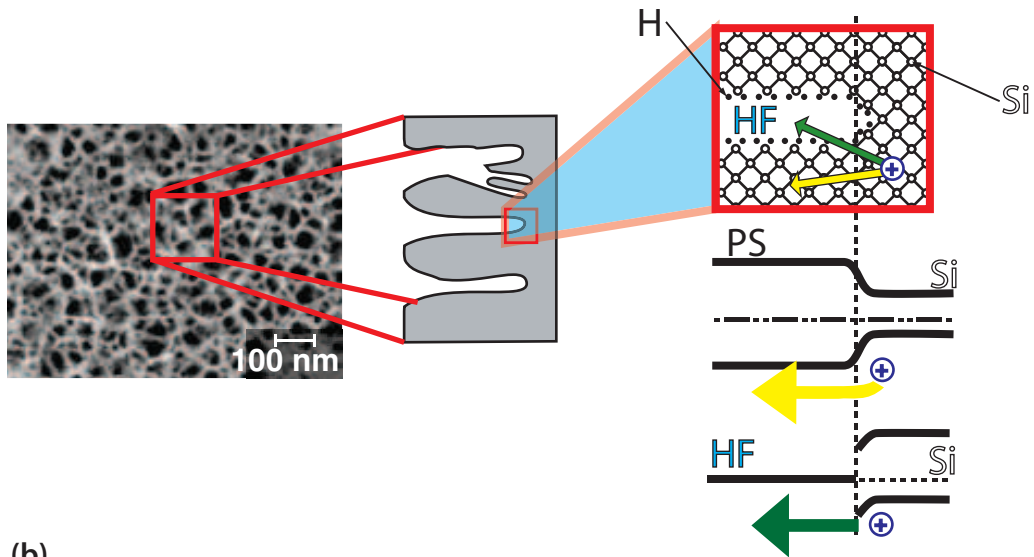
Figure 1.7: Formation of pore in porous silicon [113, 122]. (a) Chemical formula for the etching process. (b) Formation of pores in porous silicon.

which point etching becomes isotropic, resulting in complete removal of the silicon without the formation of porous layer. At this region the porosity of the etched region reaches 100%. The transition and electropolishing points are related by the concentration of the solution [113] as shown in Fig. 1.8(b).

In Fig. 1.9, we show a schematic diagram of the porous silicon etching setup we constructed for porous silicon fabrication. As concentrated hydrofluoric acid is corrosive to most metallic material and glass, the main body of the setup is made from Teflon with platinum meshs and wires serving as electrodes. The setup is divided into two identical chambers, each of which can hold approximately 150 ml of the etchant. The silicon wafer to be etched is clamped in between the two compartments with Viton O-ring to prevent etchant leakage. The size of the etch area is determined by the apertures between which the silicon wafer is clamped. In our design, these apertures are interchangeable, allowing us to easily change the size of the etched region. For the filtering experiment, we typically use an etching aperture of diameter 10 mm, while for the surface plasmon experiment, we used a larger aperture of diameter 25 mm. The electrochemical etching process produces hydrogen gas at the silicon interface. To prevent these hydrogen bubbles from collecting at the interface, the side of the opening that is away from the silicon wafer is designed to have a slope of $20°$ to the side wall. To prevent unintentional leakage, the whole setup is held on a separate PVC tray. Transfer of etchant to/from storage bottle is done by peristaltic pump with Cole-Parmer C-Flex tubing at a transfer rate of 10 ml/s. The setup is connected to a computer controlled galvanostat that is interfaced with a computer by a USB DAQ board. A home made LabVIEW based program is used to convert the etching instruction from a Matlab generated profile to applied currents at specific time slots.

For all of the samples reported here, we used the etchant mixture of hydrofluoric acid: water : ethanol in 1:1:2 volume ratio. All samples are fabricated by using heavily doped degenerate p-type silicon with resistivity of $\rho = 5 \, \text{m}\Omega \cdot \text{cm}$ which gives dopant concentration of around $10^{19} \, \text{cm}^{-3}$. While the starting silicon wafer is highly conductive due to its
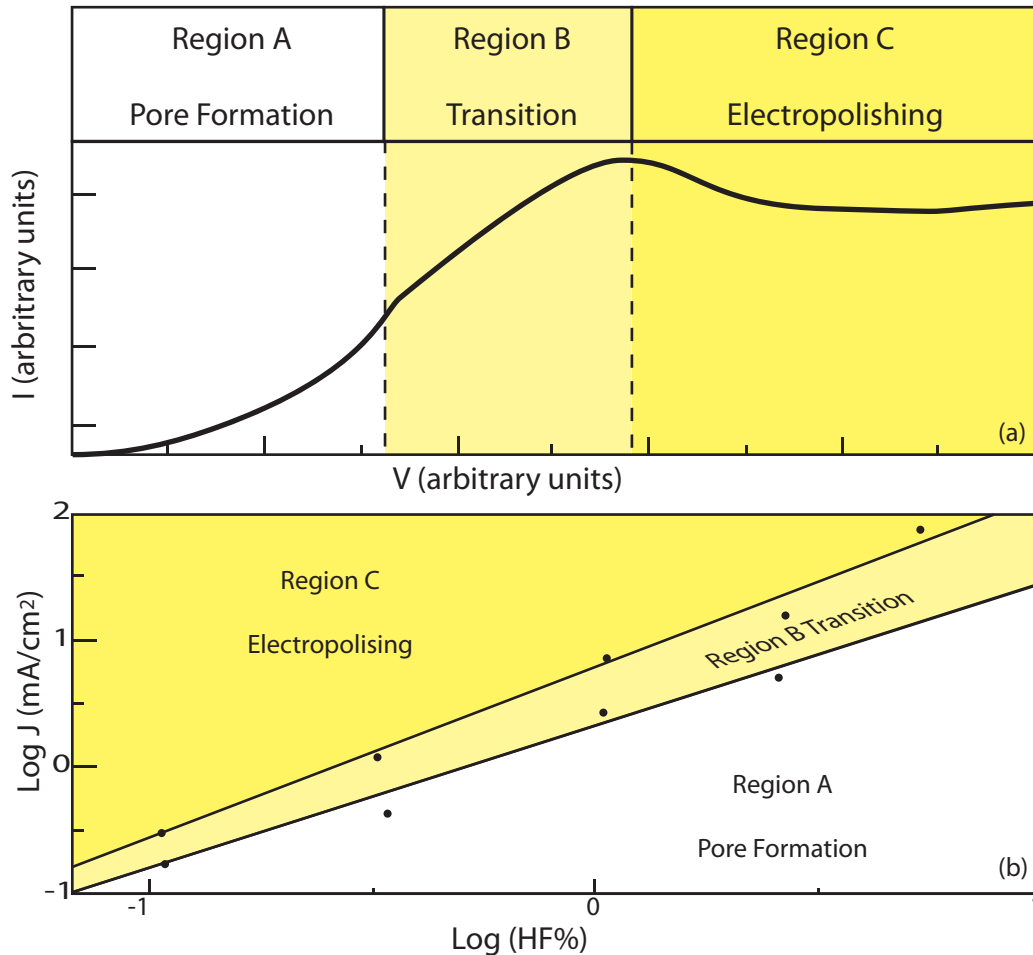
Figure 1.8: Etching parameters of porous silicon. [113] (a) I-V curve of the etching process. At low applied voltage, the applied current increase exponentially with the porosity gradually increase as the current is increased. As the voltage continue to increase to region B, both pore formation and electropolishing exist. While the etching is still preferentially deepen further into the silicon, the pore also broaden horinzontally. Beyond a certain applied voltage at the onset of region C, the etching becomes unpreferential, at this point the porosity becomes 100% and the etching happened isotropicly. (b) Dependent of the transition and electropolish points on the solution concentration.
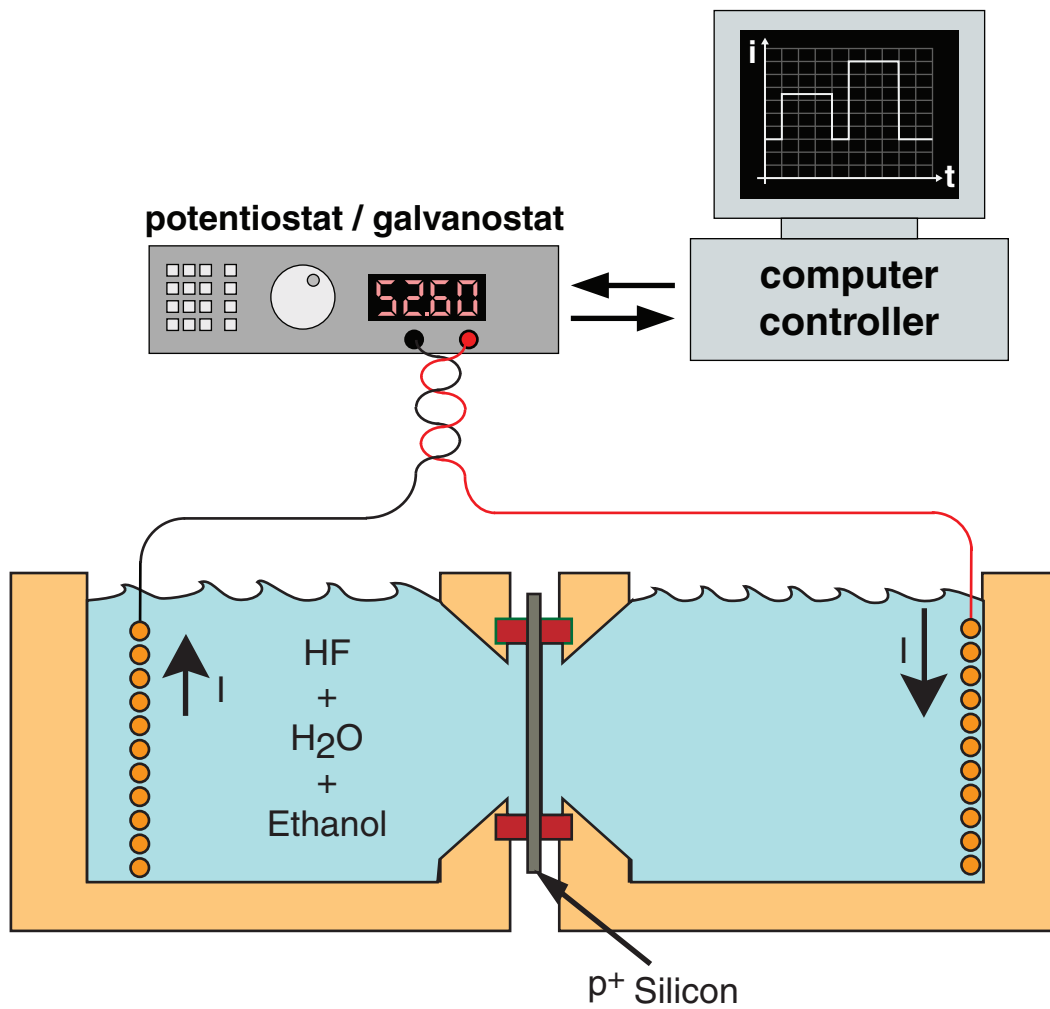
Figure 1.9: Schematics diagram of the porous silicon etching setup

high carrier concentration, the finished porous silicon has AC resistivity of a few tens or hundreds of $\Omega \cdot$ cm and is transparent to THz radiation, as we will show in Sec. 2.2.2. To allow for the etchant to replenish inside the porous matrix during the etching process, we typically apply the current in pulses. The pulse lengths and gaps between pulses is varied depending on the intended purpose of the porous silicon sample. For high quality thin layer of less then 10 μm, we usually apply pulses of 0.2 s with gaps of 10 s. On the other hand, for sample that is intended to be several hundreds of microns thick, a pulse length of 0.1 s with gaps of 0.3 s is used in order to reduce the total fabrication time. For p-type sample such as what we used for this thesis, no optical illumination is needed, however if the etching of n-type sample is required for their pore size or electric properties, the setup is designed to have a removable 1" diameter side hole that could be replaced by a Calcium Fluoride window that would allow optical illumination.

The porosity of fabricated samples is found by selectively removing of the porous silicon film in a solution of NaOH and comparing the reduced weight with its original weight before pore etching [143, 144]. Assuming that the weight of the silicon wafer before etching, after etching and after removal of porous layer are designated W_1,W_2,W_3 respectively, the porosity of the porous silicon, ρ is given by

$$\rho = \frac{W_1 - W_2}{W_1 - W_3}.$$

In Fig. 1.10, we shows the porosity and etch rate of this particular setup and etchant concentration. For this particular combination of etchant concentration and setup design, we found that the lowest porosity possible is around 40% primarily due to the slow etch rate at the low applied etching current. The setup is capable of electropolishing the sample at high current density . In practice, however, we find that porosities higher that 80% result in very fragile samples. Hence we typically limit the allowed porosity to be in between $40 - 80\%$. After the porous sample is removed from the etching system, it is rinsed in a sequence of deionized water, ethanol and isopropanol and left the sample to air dry in the
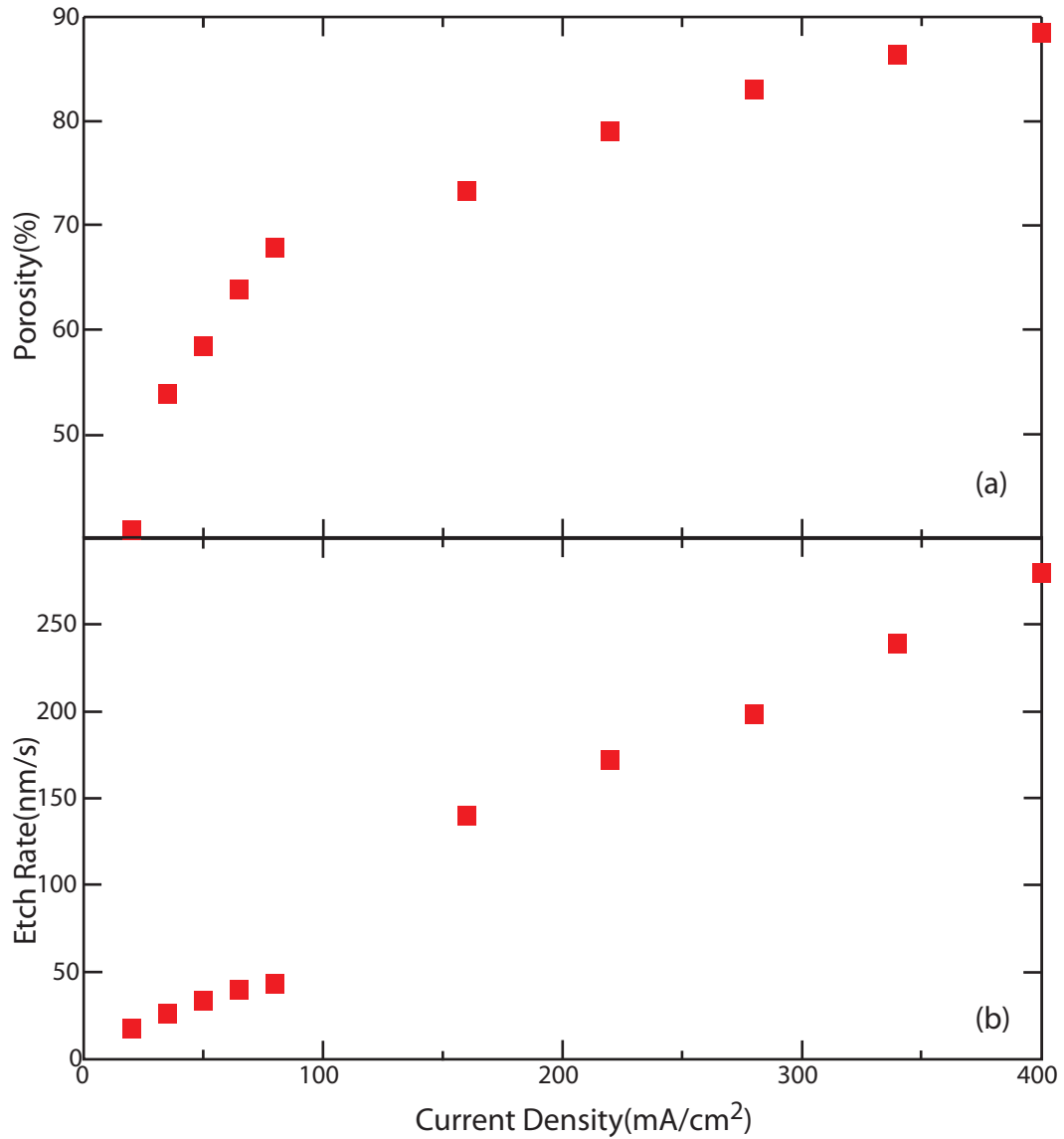
Figure 1.10: Porosity and etch rate dependent on applied current density.

laboratory environment.

1.3 Research motivations and summary

The purpose of this research work can now be listed as followed:

1. Porous silicon is a relatively unexplored material in the terahertz region, with only two prior studies reported [145, 146]. It is therefore required to determine whether

porous silicon is a viable material for fabricating multilayer structures for THz devices Some properties of interest are losses and stability of the material. For spectroscopy applications, it is also important to demonstrate that the transmission spectrum of porous silicon is relatively flat to avoid complication in analysis. In Chap.2, we found that the terahertz transmission spectrum of porous silicon is relatively featureless. Furthermore, we also found that by partially oxidizing the surface of porous silicon, it is possible to achieve low loss and stability.

2. With the proof that porous silicon is a viable terahertz material, we fabricated a 467 μm thick 13 layer porous silicon based Bragg grating with porous silicon etched within a single silicon wafer in Chap.3 as a proof of concept for terahertz filtering. The targeted frequency is designed at 1.17 THz with peak power reflectivity of 93% and full width half maximum of 0.26 THz. We describe the theoretical modeling, measurement, and fabrication of this device. Experimentally obtained transmission and reflection spectrum of the fabricated THz Bragg grating is found to be an excellent match to the theory. The fabrication of this Bragg filter also shows that it is possible to fabricate thick a porous silicon layer of hundreds of microns thick.

3. As part of the ongoing effort on using porous silicon as a waveguide material for spectroscopy , we conducted a preliminary experiment on the effect of porous silicon layer on surface plasmon propagation on the surface of highly doped silicon wafer. In Chap. 4, detailed explanation on the theoretical explanation of the phenomenon is provided with comparison to experimental results conducted on highly doped silicon with porous silicon of different thicknesses.

Hence, we show in this thesis that porous silicon is a viable material for terahertz application. This work demontrated the first ever porous silicon based filter and guided-wave devices for terahertz frequency.

Chapter 2

Porous silicon as a terahertz material

In this chapter, we discuss our effort in developing porous silicon as a optical material for applications in terahertz frequency. As explained in Chap. 1 Sec. 1.2, porous silicon is an attractive optical material as it is easy to fabricate, contains a large active surface area, and can be fabricated with a range of refractive indices. For most proposed applications, porous silicon as a terahertz material is only attractive if it is proven to have low loss, high stability and relatively featureless absorption spectrum in the terahertz regime. In Sec. 2.1, we discuss our effort to develop a theoretical understanding of the dielectric function of porous silicon in terahertz frequency and provide brief review of prior measurements in far-infrared regime. We begin with effective medium models that can be used to estimate the dielectric function of porous silicon based on the porosity. As we would find out later, the dielectric function of porous silicon is more complicated than that predicted by a simple effective media approximations. A few key contributions are summarized from literature and we try to explain the connections between measurements conducted by other groups in Fourier transform infrared spectroscopy(FTIR), Raman scattering measurements, and our results. In Sec. 2.2 we will report our finding on measurement of dielectric function of the porous silicon samples we fabricated and comparing these result with similar experiments by other groups [145, 146].

2.1 Dielectric function of porous silicon

In subsection 2.1.1, we introduce several commonly used effective medium approximation models. The detailed explanation of the model is beyond the scope of this thesis, hence only the model assumptions and their numeric expressions are given here. A comparison between different theoretical models and the actual terahertz measurement is also shown. While none of the theoretical models give perfect estimation of the refractive index, the Bruggeman model of spherical inclusion is found to be the closest to our measurement. Nonetheless, these models provide good estimation as the starting point for experiment. In subsection 2.1.2, we will discuss the prior measurements of terahertz absorption features of bulk silicon. For undoped bulk silicon, literature suggests that the spectrum is dominated by the phonon resonance peaks of Si-Si bond. For moderately or heavily doped silicon, it is found that free carrier absorption dominates the dielectric function. Only at low temperature when the carriers are bound do the resonance peaks of silicon and impurities appear. In porous silicon, not only do we expect to see the inherent absorption peaks of silicon, but we also expect additional impurity peaks associated with the etching process. Prior measurement with FTIR and Raman scattering are summarized here, with the intention of providing a reference for interpretation of the measurement we performed, which is discussed in Sec. 2.2.

2.1.1 Estimation of effective refractive index

The problem of estimating effective refractive index from a compound mixture of different dielectric materials is a problem of averaging dielectric functions of all materials. Assuming that the embedded materials are spherical inside a host medium of ε_h, the effective dielectric constant is given by Clausius-Mossotti equation as [134, 135, 147]

$$\varepsilon_{eff} = \varepsilon_h \left(\frac{1 + 2\langle \alpha \rangle}{1 - \langle \alpha \rangle} \right), \tag{2.1}$$

where the polarizability per unit volume $\langle \alpha \rangle$ is given by

$$\langle \alpha \rangle = \left\langle \frac{\varepsilon_i - \varepsilon_h}{\varepsilon_i + 2\varepsilon_h} \right\rangle = \sum_i \frac{\varepsilon_i - \varepsilon_h}{\varepsilon_i + 2\varepsilon_h} f_i, \tag{2.2}$$

with the index i representing different materials with dielectric constant of ε_i embedded as minuscule spheres in the host and f_i represented the filling factor of the material. ε_h represents the dielectric function of the host material into which the spheres are embedded. Depending on how the host material and the filling factor are defined, we could derive a variety of effective medium models for different situations. In the case when one define ε_h to be the same as the effective dielectric constant $\varepsilon_h = \varepsilon_{eff}$, then we see from Eq. 2.1 that

$$\frac{1 + 2\langle \alpha \rangle}{1 - \langle \alpha \rangle} = 1,$$

which could only be true if $\langle \alpha \rangle = 0$, hence

$$\sum_i \frac{\varepsilon_i - \varepsilon_{eff}}{\varepsilon_i + 2\varepsilon_{eff}} f_i = 0. \tag{2.3}$$

Which is the expression for Bruggeman effective medium model. For an air-filled porous silicon sample, we could visualize this model as spheres of air and spheres of silicon evenly distributed in a host of ε_{eff}. From a practical point of view, this assumption works well in the case where all elements of the mixture have similar filing factor. Hence for a porous silicon film of porosity p filled with nothing but air the effective permittivity is found by solving the equation

$$(1 - p) \cdot \left(\frac{\varepsilon_{Si} - \varepsilon_{eff}}{\varepsilon_{Si} + 2\varepsilon_{eff}} \right) + p \cdot \left(\frac{1 - \varepsilon_{eff}}{1 + 2\varepsilon_{eff}} \right) = 0. \tag{2.4}$$

Here we rewrite f_{Si} as $(1 - p)$ and f_{air} as p, the porosity that can be experimentally measured by the gravimetric method [1] .

---

[1] Alternative definition such as in Lorentz-Lorenz model [135] define f_i as the volume ratio $f_i = \frac{N_i n_i^{-1}}{\sum_j N_j n_j^{-1}}$

In the case where one element in the mixture is much more abundant then the others, $f_B \gg f_A$, the effective dielectric constant is better estimated by the Maxwell-Garnett model [134]. This model replaces the host dielectric constant as $\varepsilon_h = \varepsilon_B$, the dielectric constant of the material that is most abundant. Then for air-filled porous silicon of either very high or very low porosity, we find

$$\langle \alpha \rangle = \left(\frac{\varepsilon_A - \varepsilon_B}{\varepsilon_A + 2\varepsilon_B} \right) f_A, \tag{2.5}$$

which could be substituted into Eq. 2.1 to find ε_{eff},

$$
\varepsilon_{eff} = \varepsilon_B \left\{ \frac{1 + 2f_A \left[\frac{(\varepsilon_A - \varepsilon_B)}{(\varepsilon_A + 2\varepsilon_B)} \right]}{1 - f_A \left[\frac{(\varepsilon_A - \varepsilon_B)}{\varepsilon_A + 2\varepsilon_B} \right]} \right\}
$$

$$
= \begin{cases} \frac{1 + 2(1-p)\left[\frac{\varepsilon_{Si}-1}{\varepsilon_{Si}+2} \right]}{1 - (1-p)\left[\frac{\varepsilon_{Si}-1}{\varepsilon_{Si}+2} \right]}, & p \approx 1 \\[3ex] \varepsilon_{Si} \left\{ \frac{1 - 2p\left[\frac{\varepsilon_{Si}-1}{1+2\varepsilon_{Si}} \right]}{1 + p\left[\frac{\varepsilon_{Si}-1}{1+2\varepsilon_{Si}} \right]} \right\}, & p \approx 0 \end{cases} \tag{2.6}
$$

Strictly speaking, Eqs. 2.4 and. 2.6 are only true for minuscule sphere embedded in host material. For different geometry, one could arrived at different form of Eqs. 2.3 and 2.6. In the more general case of ellipsoid embedded in host for example, we have [134]

$$\frac{\varepsilon_{Si} - \varepsilon_{eff}}{\varepsilon_{eff} + L_j(\varepsilon_{Si} - \varepsilon_{eff})}(1-p) + \frac{1 - \varepsilon_{eff}}{\varepsilon_{eff} + L_j(1 - \varepsilon_{eff})}p = 0, \qquad \text{(Bruggeman)} \tag{2.7}$$

and

---

with N_i as the numbers of atom/molecules in the mixture and n_i^{-1} is the volume each atom/molecules would occupied. However, the definition by weighting method has the advantages of easily applicable in practice.

$$\varepsilon_{eff} = \begin{cases} \frac{(1-p)(\varepsilon_{Si}-1)(1-L_j)+\left[L_j\varepsilon_{Si}+(1-L_j)\right]}{L_j\varepsilon_{Si}+(1-L_j)-(1-p)(\varepsilon_{Si}-1)L_j}, & \text{Maxwell-Garnett } p \approx 1 \\ \frac{p\varepsilon_{Si}(1-\varepsilon_{Si})(1-L_j)+\varepsilon_{Si}\left[L_j+(1-L_j)\varepsilon_{Si}\right]}{L_j+(1-L_j)\varepsilon_{Si}-p(1-\varepsilon_{Si})L_j}, & \text{Maxwell-Garnett } p \approx 0 \end{cases} \tag{2.8}$$

where L_j is a dimensionless number that ranges from 1/3 to 1 depending on the eccentricity of the ellipsoid. For the special case of spherical inclusions, we take $L_j = 1/3$, in which case Eqs. 2.7 and 2.8 resolve to the same expressions given earlier.

Fig. 2.1 shows the measured refractive index of porous silicon as a function of the measured porosity, in comparison to the different theoretical models based on the effective medium approximation. The experimental result are measured with our terahertz spectroscopy system with sample fabricated with different etching currents in similar procedure as will be described in Sec. 2.2, intrinsic dielectric constant of bulk silicon is used for these models rather then the dielectric function predicted by Drude model and the reason would be explained in subsection 2.1.2. Theoretically, the porosity and hence the refractive index can be adjusted continuously from $p = 1$, (completely porous, $n = 1$) to $p = 0$, (bulk silicon, $n = 3.4$). In practice, it is found that porosity range of porous silicon is limited by two factors. 1) At the low porosity range, the etch rate of the sample reduced as the etching current reduced. In order to obtain an acceptable etch rate, we found that $\sim 40\%$ is the lowest practically achievable porosity. 2) As the porosity becomes closer to 100%, the sample becomes too fragile to handle. Typically, at porosity higher than 90%, we discovered that the silicon skeleton would collapse if left when the solvent evaporates from the porous skeleton. Hence the practical porosity range is around 40-80%, which translated to a porosity range from 1.3-2.4 by using the Bruggeman effective medium approximation. Given that porous silicon is highly anisotropic with long, columnar pores, it is surprising that the prediction from spherical inclusions($L_j = 1/3$)show better agreement than the ellipsoid geometry models of $L_j = 0.9$. One possible explanation is that while the porous silicon pores are column like, the side wall are irregularly shape, hence the end result is that the geometry is more likely to resemble ellipsoid with small long/short axis
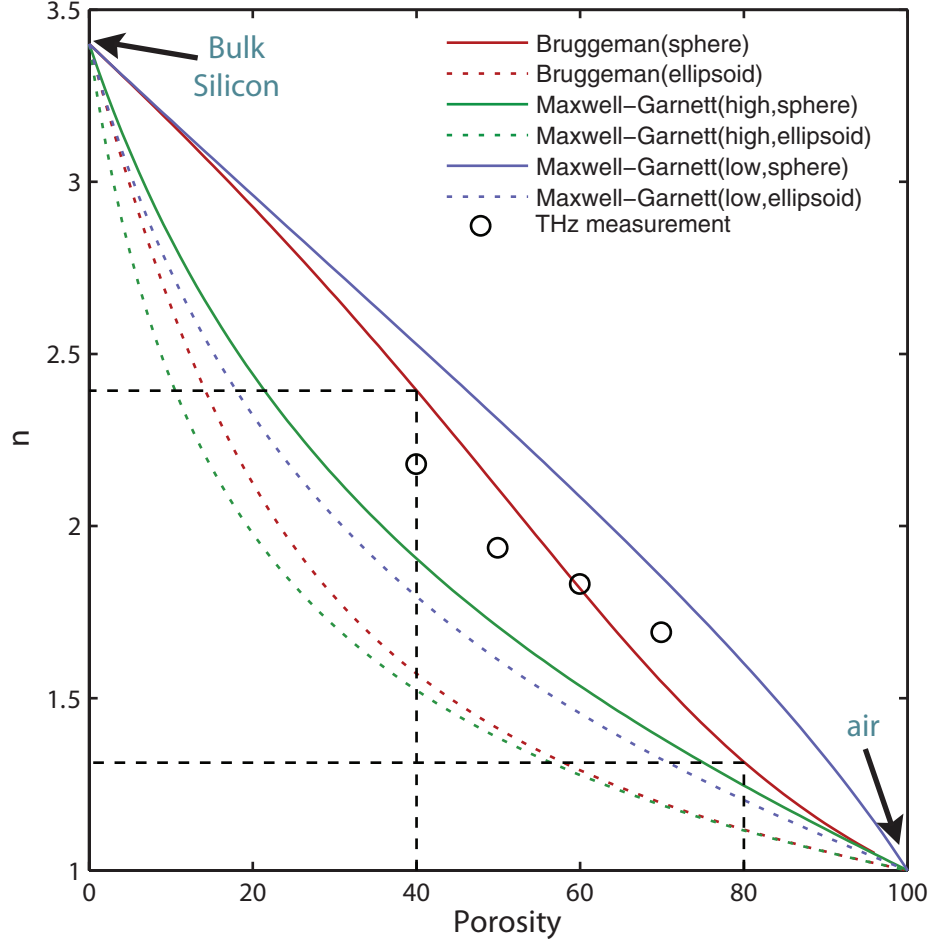
Figure 2.1: Porosity versus refractive index. Different effective medium approximation models are used to predict the resultant refractive index. The sphere geometry curves are calculated by solving Eqs. 2.4 and 2.6 while the ellipsoid geometry curves are calculated by Eqs.2.7 and 2.8 using L=0.9. Circles indicated actual terahertz measurement of porous silicon sample with different porosities. The practical achievable porosity (40-80%) and the corresponding refractive index (1.3-2.4) is shown by the dash lines.

ratio (i.e. more like a string of spheres). On the other hand, it is not surprising that the Bruggeman method give better agreement then the Maxwell-Garnett method as the porosity of our samples are generally outside of the range where the Maxwell-Garnet theory is expected to hold.

2.1.2 Phonons and free carrier absorption in silicon and porous silicon

The refractive index and absorption coefficient of a semiconductor are affected by multiple phenomena, related to both the intrinsic properties of the semiconducor, and the extrinsic properties of any impurities that are introduced. In the optical and near infrared domain, intrinsic properties such as direct/indirect bandgap absorption, generation of excitons near the bandgap dominated the dielectric function [148]. In the terahertz domain, the dieletric function is governed by the lattice phonon vibrations, the defect states of impurities and free carrier absorption. Depending of the doping level of the impurities, different effects can dominate the dielectric function. For an intrinsic semiconductor, the principal contributions to the dielectric function in the terahertz frequency regime are due to phonon absorptions. The dielectric function can be described as a sum of Lorentzian peaks due to each individual phonon absorption mode:

$$\varepsilon(\omega) = \varepsilon_\infty (1 - \sum_i \frac{\omega_{p,i}^2}{\omega_{0,i}^2 - \omega^2 + j\omega\Gamma_i}), \tag{2.9}$$

where the index i numbers each of the phonon absorption peaks centered at $\omega_{0,i}$, $\omega_{p,i}$ and Γ_i describe the center frequency, absorption strength, and peak width, respectively. For II-VI and III-V semiconductors, ω_0 represented the frequency where the incident EM wave is coupled to the optical phonon in the transverse direction ω_{TO}. For a single resonance peak, Eq. 2.9 could be rewritten as

$$\varepsilon(\omega) = \varepsilon_\infty (1 - \frac{\omega_{LO}^2 - \omega_{TO}^2}{\omega_{TO}^2 - \omega^2 + j\omega\Gamma}). \tag{2.10}$$

ω_{LO} here indicates the frequency at which the EM wave can coupled to the optical phonon oscillating in longitudinal direction. In the range of $\omega_{TO} < \omega < \omega_{LO}$, the dielectric function $\varepsilon(\omega)$ becomes negative hence the semiconductor becomes highly reflective in between ω_{TO} and ω_{LO}, a phenomenon that is used in filtering as described in Sec. 1.1. For group IV semiconductors, individual phonon does not couple to the optical dielectric

Measured peak frequency [cm^{-1}]	Measure peak frequency [THz]	Identification
371.8	11.15	TO-TA
566.2	16.99	LO+TA
609.8	18.29	TO+TA
739.7	22.19	LO+LA
818.7	24.56	TO+LA
896.1	26.88	TO+LO
963.9	28.92	2TO
1301.9	39.05	TO+2LO

Table 2.1: List of major multiphonon absorption peaks of silicon (table adapted from Ref. [149]).

constant directly. Instead, each vibrational peak $\omega_{o,i}$ contributes to the coupling between multiple phonons. In most cases, one phonon mode do breaks the crystal inversion symmetry and induced changes to two atoms in the primitive cell and the other causes these two atoms to oscillate and couple with the incident EM wave [148]. Table. 2.1 listed phonon absorption peaks of intrinsic silicon measured with far-infrared monochromator as reported in Ref. [149]. Among all of the major peaks in this spectrum, the one in 18.20 THz is the most significant and is associated with the $Si - Si$ bond seen in FTIR and Raman scattering measurements of porous silicon. In the terahertz regime, Dai et al [150] had performed the measurement from 0.5 THz to 4.5 THz and it was found that for a float zone silicon with resistivity of $10\,\text{k}\Omega\,\text{cm}$, the real part of the refractive index is essentially flat at 3.417 except at a minor absorption peak at 3.6 THz. The absorption coefficient increased monotonously from $\sim 0.01\,\text{cm}^{-1}$ at 0.5 THz to $\sim 0.225\,\text{cm}^{-1}$ at 4.5 THz is believed to be caused by the side tail of the two minor absorption peaks at 3.66 THz and 4.68 THz [151][2].

For moderate and highly doped silicon, the contributions from free carrier absorption become significant. At low temperature, the free carrier absorption contribution is suppressed and hence the dielectric function is dominated by absorption peaks associated with impurities in addition to the peaks of Si lattice vibrations [152]. In a highly-doped mate-

[2]Not listed in Table 2.1 as they are much weaker compared with other peaks listed.

rial at low temperture, the impurities pull the Fermi level very close to the conduction or valence band of silicon, it becomes possible for a EM wave in the far-infrared spectrum to be energetic enough to cause the jumping of electrons/holes from the defect states of the impurities to conduction/valence band of the base semiconductor, hence the EM wave is absorped [148]. On the other hand, the absorption due to free carriers is shown to be the dominant effect [153–158] for moderately to heavily doped degenerated silicon at room temperature. In both terahertz or far-infrared spectroscopy measurements [154–158], it is shown that the simple dielectric function predicted by Drude model fit well with the experimental data. In its simplest form, Drude model manifest itself similar to the phonon absorption peak in Eq. 2.9 that is centered at $\omega_0 = 0$ THz,

$$
\begin{aligned}
\varepsilon(\omega) &= \varepsilon_\infty + \frac{i\sigma(\omega)}{\omega\varepsilon_0} = \varepsilon_\infty - \frac{\omega_p^2}{\omega(\omega + i\Gamma)}, \\
\sigma(\omega) &= \sigma_{dc}\frac{i\Gamma}{\omega + i\Gamma} = \frac{i\varepsilon_0\omega_p^2}{\omega + i\Gamma},
\end{aligned}
\tag{2.11}
$$

with Γ being the scattering rate by phonon and impurities in the doped silicon, σ_{dc} is the conductivity of the sample measured in dc. For heavily doped silicon, the mobility is affected by the doping concentration and the temperature of the sample as Eq. 2.12 [159].

$$
\begin{aligned}
\mu_h &= 54.3T_n^{-0.57} \\
&+ \frac{1.36 \times 10^8 T^{-2.23}}{1 + [N/(2.35 \times 10^{17}T_n^{2.4})]0.88T_n^{-0.146}}, \\
\rho &= \frac{1}{qN\mu_h} \\
T_n &= T/300.
\end{aligned}
\tag{2.12}
$$
$$
\tag{2.13}
$$

Hence one can calculate the scattering time $\tau = \frac{1}{\Gamma}$ by using the expression $\tau = \frac{\mu_H m*}{q}$, with $m* = 0.37\,m_e$ the effective mass of hole in p-doped silicon, q is the charge of a single
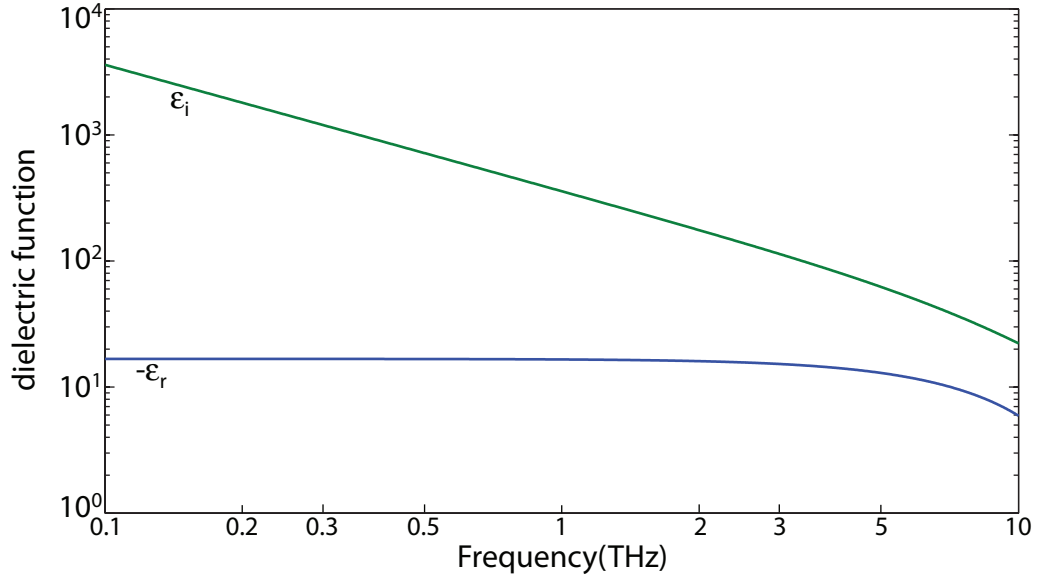
Figure 2.2: Calculated dielectric function of heavily p-doped silicon with resistivity of $\rho = 5$ mΩ cm. Mobility of hole is calculated from Eq. 2.12. and the effective hole mass is taken from Ref. [158] as 0.37 m_e, the calculated Γ and ω_p are 7.99×10^{13} s^{-1} and 1.25×10^{14} s^{-1}.

electron. Furthermore, the plasma frequency ω_p is given by $\sqrt{\frac{Nq^2}{\varepsilon_\infty \varepsilon_0 m*}}$ with N the number of carrier obtained by solving Eq. 2.13. Hence, using the room temperature of 300 K, $\varepsilon_\infty = 3.4^2$, the resistivity of 5 mΩ cm, we estimate $\Gamma = 8 \times 10^{13}$ s^{-1} and $\omega_p = 1.3 \times 10^{14}$ s^{-1}. The resultant dielectric function is plot in Fig. 2.2. Note that the calculation does not include the contribution of phonon and impurities, hence it should only be used as an estimation. Nonetheless, it had been shown that the free carrier absorption model matches well with experimental data [154–158].

The dielectric function of porous silicon is a lot more complicated. Intuitively, one might think that a simple application of the effective medium model to the dielectric function of silicon would predict the dielectric function behavior of porous silicon. This assumption is however proven to be too simplistic [160–169]. First of all, the etching process introduces a few more absorption peaks due to the binding of impurities from the etchant to the silicon [160, 163, 166–169]. During the etching process, silicon atoms on the surface bind with hydrogen to form the SiH_x bonds. Hence, not only would one see the absorp-

tion peaks of $Si - Si$ at 615 cm^{-1} (18 THz) and the bulk $Si - O - Si$ bond at 1108 cm^{-1} (33 THz) that originally existed due to natural oxidation of the surface, new peaks would appeared in between $2090 - 2141$ cm^{-1}($63 - 64$ THz), 915 cm^{-1} (27.5 THz) and in between $615 - 666$ cm^{-1} (18.5-20 THz). If the porous silicon is then oxidized as we will describe in Sec. 2.2, then these SiH_x bonds will be shifted, reduced and eventually disappear and new absorption peaks, associated with replacing the $Si - H$ bond to $Si - OH$, $-O_y Si - H_x$ and $Si - O - Si$ bonds will appear. The location of these bonds and their associated bonding is tabulated in Table. 2.2. Note that these absorption peaks are far beyond the measurable frequency range of our current terahertz spectroscopy system.

The second effect is that while a straightforward application of effective medium model to Eq. 2.11 would predict a free carrier absorption of the same order, the etching of porous silicon reduces the number of majority carriers and the scattering time τ [167]. Hence while the starting silicon wafer is completely reflective due to its high conductivity, the porous silicon would have about 2 orders of magnitude reduction in conductivity and if the surface of this porous silicon is partially oxidized, the conductivity would reduced by another 2 orders of magnitude as we will show in Sec. 2.2. Hence although the dielectric function of the starting wafer is very different from intrinsic silicon, we found that the dielectric properties of intrinsic silicon($\varepsilon = \varepsilon_\infty = 11.7$) gives better prediction and model the additional absorption phenomenologically in order to fit the observed data.

Thirdly, when the silicon is etched away from the pore sites, the remaining silicon could have dimension of a few to tenths of nanometer. The crystal Brillouin zone would change for these nanocrystalline structures, and the phonons would be confined and hence the original absorption peaks of silicon listed on Table. 2.1 would be shifted and broadened toward low frequencies. If the bulk phonon linewidth is known, one could use this effect and the absorption peaks of the starting silicon wafer and obtain an estimate of the silicon skeleton size, $[161, 162, 164, 165]$

Fresh porous silicon (Hydrogen terminated)			Oxidized porous silicon (oxide and hydroxide terminated)		
Bonding	k_{0i} (cm^{-1})	f_{0i}(THz)	Bonding	k_{0i} (cm^{-1})	f_{0i} (THz)
$Si-Si$	615	18	$SiOH$	3745	112
$Si-O-Si$	1108	33	$-O_y-Si-H_x$	2276, 877	68, 26
SiH_3	2141	64	$Si-O-Si$	1168, 1050	35, 31.5
SiH	2115	63.5	$Si-Si$	615	18
SiH_2	2090, 915	63,27.5			
SiH_x	666, 622, 615	20, 18.5, 18.5			

Table 2.2: Major absorption peaks for freshly made porous silicon, oxidized porous silicon (data from Ref. [166]).

$$I(\omega) = \int_0^1 \frac{\exp(-q^2 L^2/4a^2)}{[\omega - \omega(q)]^2 + (\Gamma_0/2)^2} d^3 q$$

where $q = 2\pi/a$, a is the lattice constant of silicon, Γ_0 is the linewidth of LO phonon of the bulk silicon, L is the size of the silicon skeleton and $\omega^2(q) = A + B\cos(\pi q/2)$ is the dispersion of the LO phonon with $A = 1.714 \times 10^5$ cm^{-2} and $B = 1.000 \times 10^5$ cm^{-2}. While we do not use this equation for fitting the experimental data in Sec. 2.2 and Sec. 3.2 due to the complicated fitting process, the model we used $\varepsilon(\omega) = A + iB\omega$ in Sec. 3.2 could be either thought of as the expression for the side tail of a far away phonon absorption peak that is extended to terahertz range by phonon confinement .

2.2   Experimental results

In this section, we will discuss our effort in measuring the dielectric function of porous silicon. During the experiment, we discovered that freshly made porous silicon is both lossy and unstable for practical optical application, however an oxidation process that partially oxidizes the surface improves the resistivity and stability considerably. While the fitting model we used here only incorporates the simple Drude model, we found that it still describes the dielectric function quite well for the thin sample we fabricated in this experiment. Later on, in Chap. 3 Sec. 3.2, we found that the model does not give good prediction for thicker sample, hence a different model was adopted.

For these measurements, we limited our observations to porous silicon samples made by applying pulses of 80 $\frac{mA}{cm^2}$ with pulse width of 2 minutes and 1 minute interval between each pulses but we expected similar behavior for porous silicon etched with different current density. Such pulses are applied for a total etch time of 20 minutes after which the resulting film is separated from the wafer by applying a 7 second pulse of 360 $\frac{mA}{cm^2}$. The sample is then rinsed with ethanol and dried in room air The starting wafer is a <100> highly degenerately boron doped p-type silicon wafer with resistivity of $\rho = 1 - 5\,\text{m}\Omega\,\text{cm}$ with

corresponding dopand concentration of 10^{19} cm^3 and total thickness of around $500\,\mu$m. The resulting porous silicon membrane has porosity of 67% and a total thickness of approximately $65\,\mu$m.

2.2.1 Characteristic of highly doped porous silicon in THz spectrum

Fig. 2.3(a) shows a comparison between time domain THz traces measured with and without the freshly made porous silicon sample inserted into THz system. The freshly made P^+ porous silicon transmits only 30% of the THz amplitude. Furthermore, by monitoring the peak amplitude over a period of 1 hour, we found that the peak amplitude of the transmitted THz pulse decreases further to only 19% for this particular sample. Such behavior is not due to shift in peak position in time domain or laser power drift but is due solely to an increase in the sample attenuation over time. This was confirmed by taking a time domain scan of the terahertz signal before and after a one-hour period at the terahertz pulse peak on Fig. 2.3(b) where the THz peak amplitude returns to its unattenuated value after removal of sample from the THz beam path.

The attenuation varied from sample to sample, but was usually measured to be about 10-50% when measured less then 24 hours after fabrication. Similarly, the time dependent reduction varied from sample to sample but is usually at around 10-20% less from its initial value 1 hour after the sample was illuminated. If the sample is measured daily, we found that the transmission of the sample gradually increased and also became more stable until 13 days after the sample is made where the transmission reached a maximum value of about 90% .

We had also observed that if the sample was moved such that the THz beam illuminates a previously unilluminated portion of the sample, the peak amplitude will return to its initial value and then undergo a similar decay in transmission (Fig. 2.5(a)). Furthermore, by purging the environment surrounding the sample with dry air, we see a slow drift in the absorption associated with the change in ambient humidity (Fig. 2.5(b)). This behavior
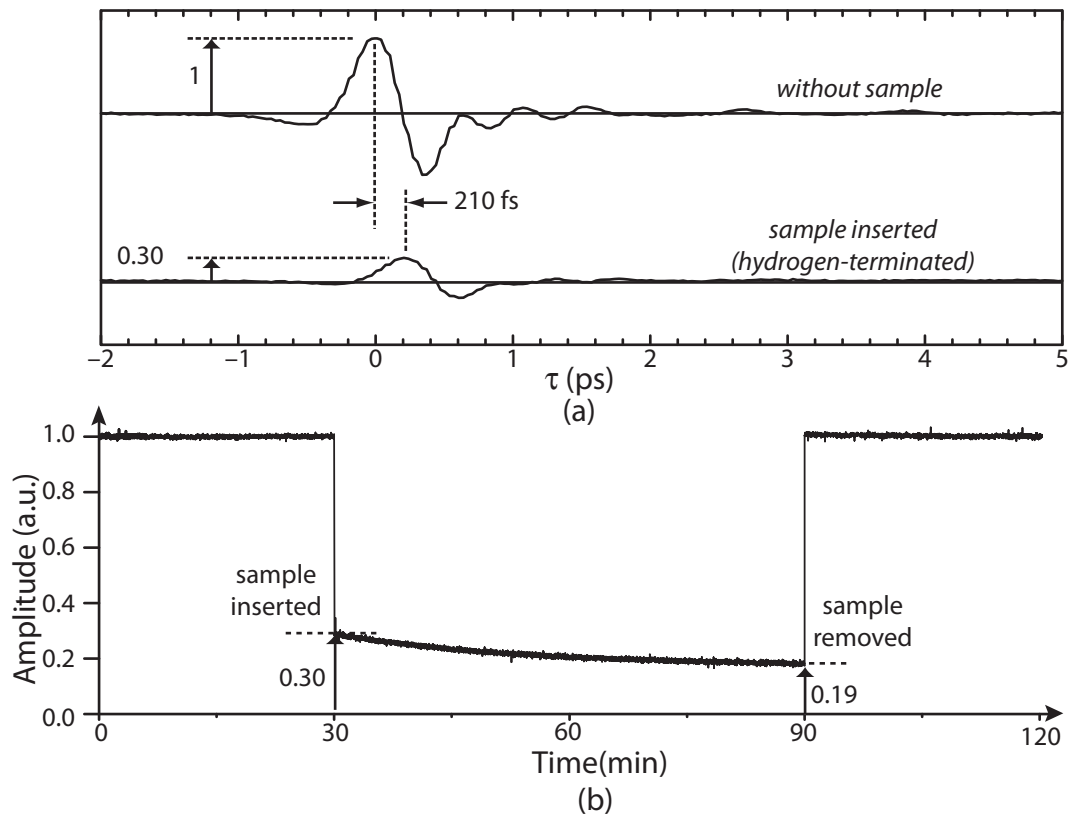
Figure 2.3: (a)Comparison between reference signal and signal transmitted from freshly made porous silicon at the beginning of measurement (b) Continue monitor of the terahertz signal peak over a period of 120 minutes. A reduction trend in the sample transmission amplitude from 30% to 19% is clearly observed.

39
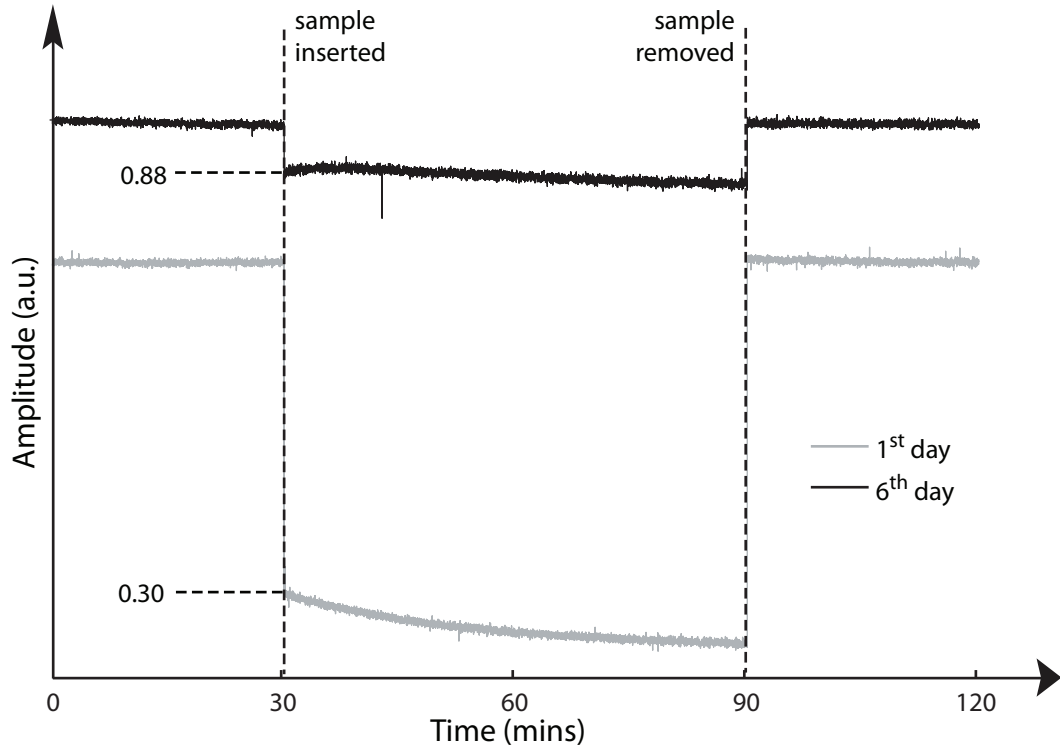
(a) Comparison between the stability of terahertz signal peak for a 1 day sample and the same sample 6 days after.
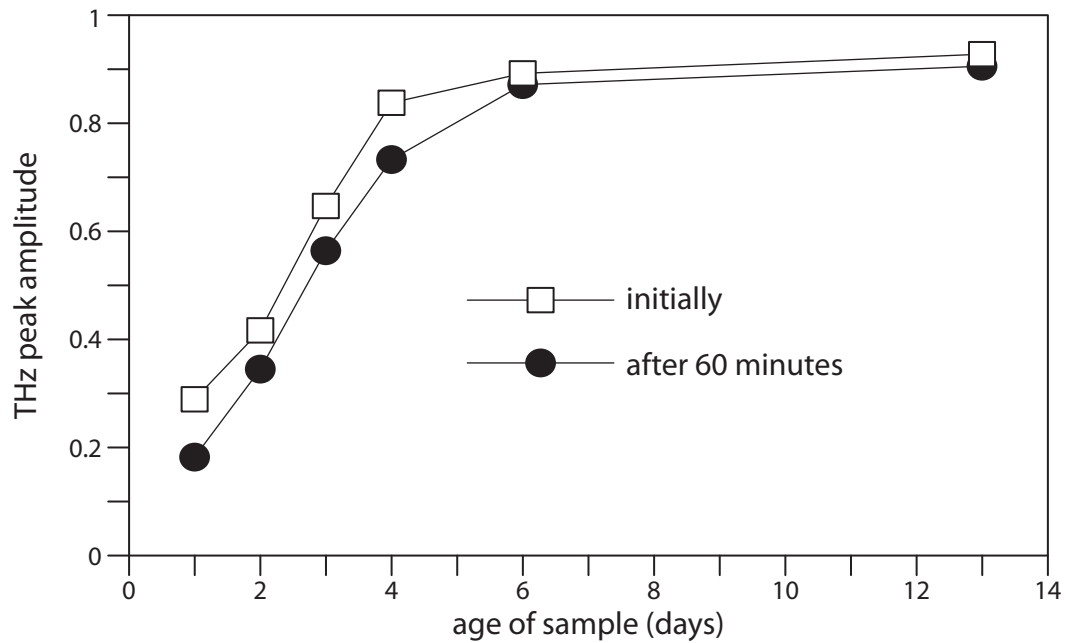
(b) Natural aging of a sample over time.

Figure 2.4: Aging effect on THz transmission of porous silicon. (a) Change in terahertz transmission from the same sample 1 day and 6 days after fabrication. The change in reduction rate of the transmission coefficient and the different in transparency are clearly seem. 1 day sample trace is shifted for clarification. (b) Daily increase of transmission of the same sample. The gap between initial and later measurement after 60 minutes of illumination is reduced as well.

strongly suggests that the time dependent trend is photon-induced and is dependent on chemical bonding at the porous silicon surface.

It is well known that the surface of a freshly made porous silicon sample is terminated by unstable Si-H bond and such bond will be gradually replaced by the more stable O-Si-H and Si-O-Si bond as the sample is slowly oxidized in air [168, 170–172]. Thus, the optical properties of porous silicon become more stable with age, as the exposed surfaces slowly oxidize in air. To prove that such behavior is indeed the reason for reduction of attenuation as the sample aged, we thermally oxidized a sample in a furnace at 450^oC for 1 hour. Such temperature will oxidize the surface of porous silicon (to a depth of a few nanometer), but will not fully oxidize the sample. Fig. 2.6 compares the transmitted terahertz amplitude before and after oxidation of the surface. As one can seen clearly from this figure, highly doped porous silicon sample will becomes highly transmissive and stable after oxidation process is completed.

2.2.2   Effect of oxidation on porous silicon transmission spectra

To gain additional knowledge on unoxidized and oxidized porous silicon sample, we converted the time domain scan of both sample to spectral domain and obtain their corresponding complex transmission coefficient in spectral domain by dividing the measured spectral domain signal with sample in THz beam path to the signal without sample in the beam path (Fig. 2.7). As unoxidized porous silicon is unstable, we left the sample under THz illumination for 3 hours before measuring the corresponding time domain traces.

2.2.2.1   Unoxidized porous silicon

The refractive index and absorption coefficient could be obtained by weighted least square fitting the theoretical tranmission coefficient Eq. 2.14 (will be derived in Sec. 3.1) calculated with the dielectric function for free carrier absorption Eq. 2.11 to the measured transmission coefficient , obtained by taking the ratio between a terahertz measurement with the
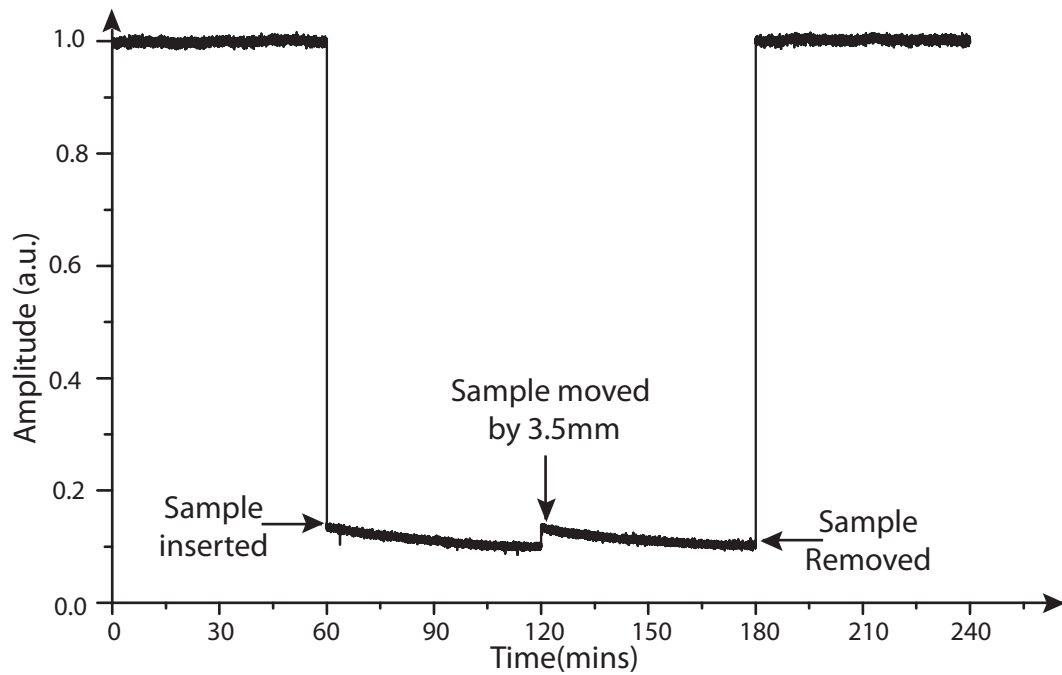
(a) Localization of the time dependent reduction of terahertz peak amplitude. The sample is moved by 3.5mm in the middle of measurement and is found to have similar transmission as initially then trace a similar trend of reduction.
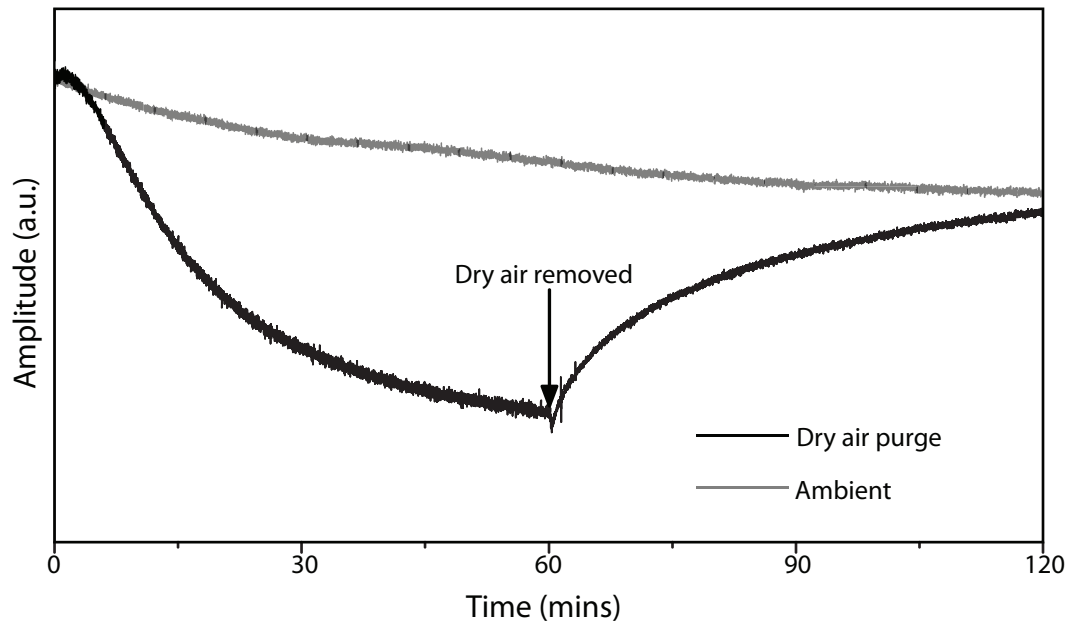
(b) Humidity dependent of the terahertz peak amplitude reduction. After purging and illumination for 1 hour, dry air was removed from the THz chamber (black line). The peak amplitude is observed to slowly approach to its ambient environmental value (Grey line) after dry air removed

Figure 2.5: Localization and humidity sensitive of peak amplitude
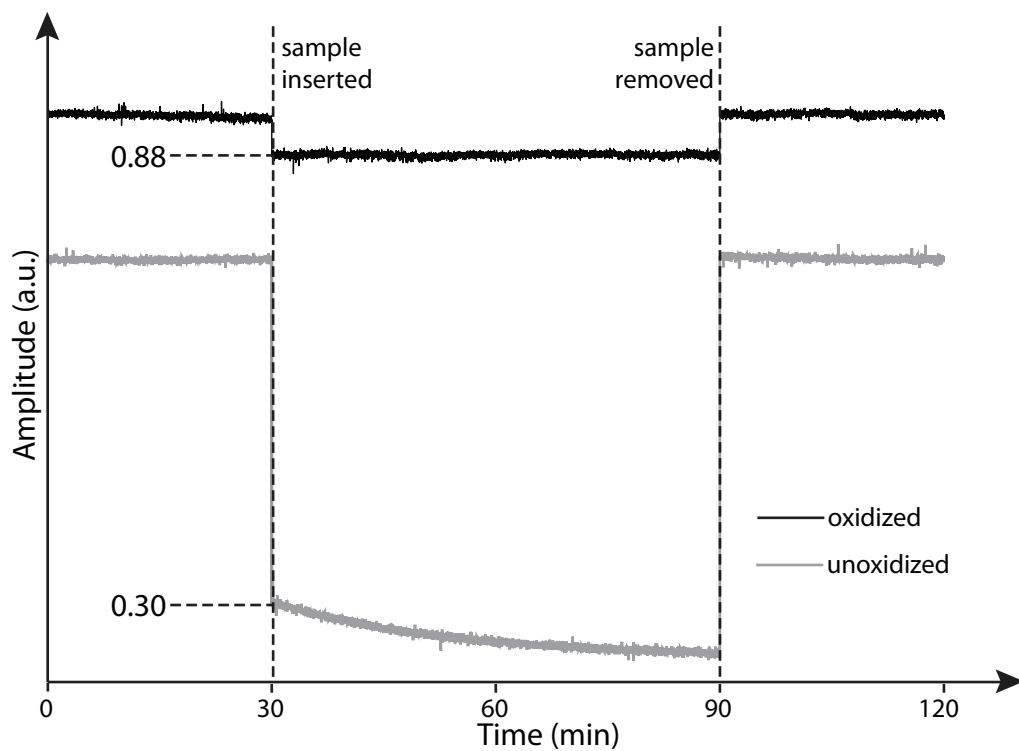
Figure 2.6: Comparison between an unoxidized sample and a thermally oxidized sample. The sample becomes transparent and stable after thermal oxidation.The oxidation curve is shifted vertically for clarification.
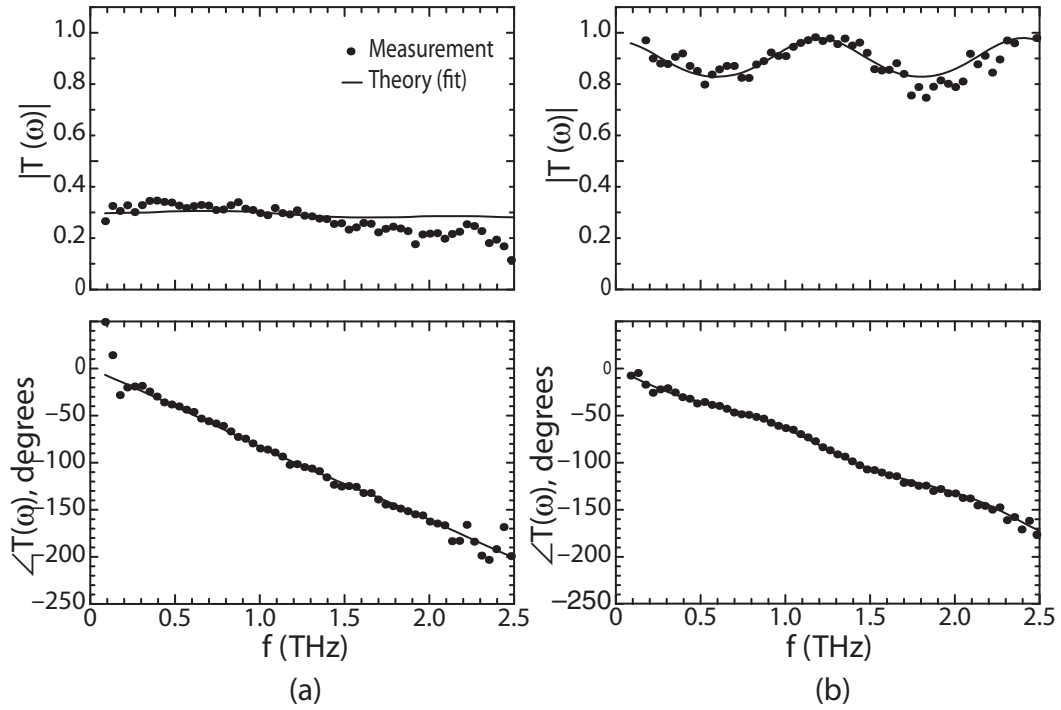
Figure 2.7: THz Transmission and phase shift due to unoxidized and oxidized samples. solid circles are measured data while lines are theoretical value generated with best fit parameters. For unoxidized sample, the best fit parameters are found to be $\varepsilon_\infty = 4.24 \pm 0.08$ and $\rho = 0.50 \pm 0.01\,\Omega \cdot \text{cm}$. For oxidized sample, the best fit parameters are $\varepsilon_\infty = 3.32 \pm 0.07$ and $\rho = 35 \pm 9\,\Omega \cdot \text{cm}$.

sample and a terahertz measurement without the sample. A set of paramaters comprised of high frequency dielectric constant ε_∞ and the DC resistivity $\rho = 1/\sigma_{dc}$ are chosen as the fitted parameters. We seek to minimized the error between fitted transmission coefficient $T_{calc}(\omega, \rho, \varepsilon_\infty)$ and the measured transmission coeffcient $T_{meas}(\omega)$ over the entire measurable spectrum with emphasized on the frequency range that have the highest signal to noise ratio (ie. weighted by terahertz spectrum without sample, $W(\omega) = E_{Ref}(\omega)$). In mathematic forms, Eq. 2.15.

$$
\begin{aligned}
\frac{E_{Sam}(\omega)}{E_{Ref}(\omega)} &= T_{meas}(\omega, \rho, \varepsilon_\infty) e^{j\frac{\omega}{c}l} \\
&= \frac{4n(\omega, \rho, \varepsilon_\infty)}{[n(\omega, \rho, \varepsilon_\infty) + 1]^2} \frac{e^{-j[n(\omega, \rho, \varepsilon_\infty) - 1]\frac{\omega}{c}l}}{1 + \left[\frac{n(\omega, \rho, \varepsilon_\infty) - 1}{n(\omega, \rho, \varepsilon_\infty) + 1}\right]^2 e^{-j2n(\omega)\frac{\omega}{c}l}},
\end{aligned}
\tag{2.14}
$$

$$
Minimize\{\sum_\omega W(\omega) \cdot [T_{calc}(\omega, \rho, \varepsilon_\infty) - T_{meas}(\omega)]^2\}.
\tag{2.15}
$$

Using Eq. 2.15, we found that the unoxidized sample has a resistivity of around $500\,\text{m}\Omega\cdot\text{cm}$ which is about 2 orders of magnitude larger than the original bulk silicon value and is consistent with other measurements [146, 173]. The resultant refractive index and absorption coefficient are shown in Fig. 2.8. For this particular sample, the thickness is found to be 63μm.

2.2.2.2 Oxidized porous silicon

Unsurprisingly, the transmission of the oxidized sample in spectral domain is around 90% for a sample thickness of 68 μm as shown in Fig. 2.9. The ripple in the amplitude transmission spectrum is due to Fabry-Perot effect, as evidenced from comparison with theoretical values generated with the best fitted parameters to Eq. 2.14 that taking account of the multiple reflection from the two surfaces. After oxidation, the equivalent resistivity of the
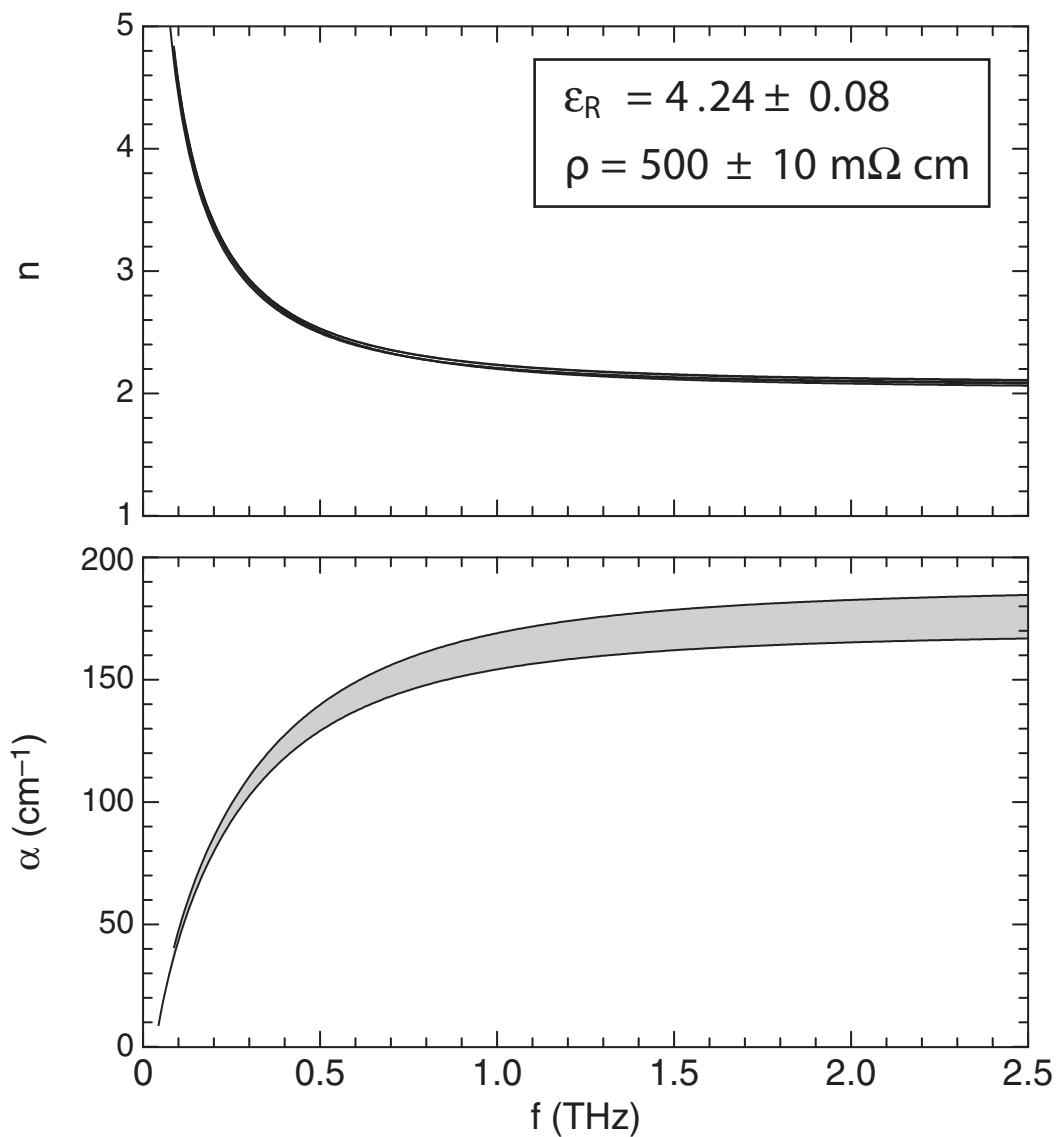
Figure 2.8: Experimentally derived refractive index and absorption coefficient of unoxidized porous silicon. Generated with best fitted parameter of Eq. 2.11, where $\varepsilon_\infty = 4.24 \pm 0.08$ and $\rho = 0.50 \pm 0.01\,\Omega \cdot \text{cm}$. Grey area represented the standard deviation of calculated refractive index and absorption coefficient

sample is further increased to around $35\,\Omega\cdot$cm which is about 2 orders of magnitude larger than the unoxidized value and 4 orders larger than in the bulk silicon. Fig. 2.9 shows the extracted real part of the refractive index and absorption coefficient of the oxidized porous silicon. The vastly reduced absorption and improved stability implied that porous silicon made from highly doped silicon could be good material for terahertz devices after surface treatment with oxidation. The strong change in conductivity is also seen in dc conductivity and optical absorption spectrum in visible range [167, 174, 175].

2.3 Conclusion

We had conducted literature research on the behavior of dielectric function of porous silicon in far-infrared frequency and experimentally measured the refractive index and absorption coefficient in terahertz spectroscopy system. Although literature reviews suggested that there should be multiple absorption peaks in the tenths of terahertz range due to phonon absorptions of silicon and impurities, none of these absorption peaks are found within the detectable range of our terahertz setup. In comparison to measurements conducted by other groups, the relative higher loss reported in [146] seem to fit in between our measurements of unoxidized and oxidized porous silicon. Furthermore, we also found that unoxidized porous silicon is unstable in terahertz transmission. By partially oxidized the surface of porous silicon, we found that the resistivity of the porous silicon increased by 2 order of magnitude and the overall absorption coefficient is reduced to $< 10\,\text{cm}^{-1}$, which prove that porous silicon could be made low loss in the terahertz regime. The reason for this dramatic difference between the unoxidized and oxidized porous silicon is unclear, but we speculated that it is due to the replacement of the unstable Si-H bonds on the surface of porous silicon by the more stable oxide bonds introduced in the themal oxidation process [166]. The measurement reported in Ref. [145] on the other hand is conducted on porous silicon fabricated from silicon wafer with lower doping concentration, hence it is difficult to make
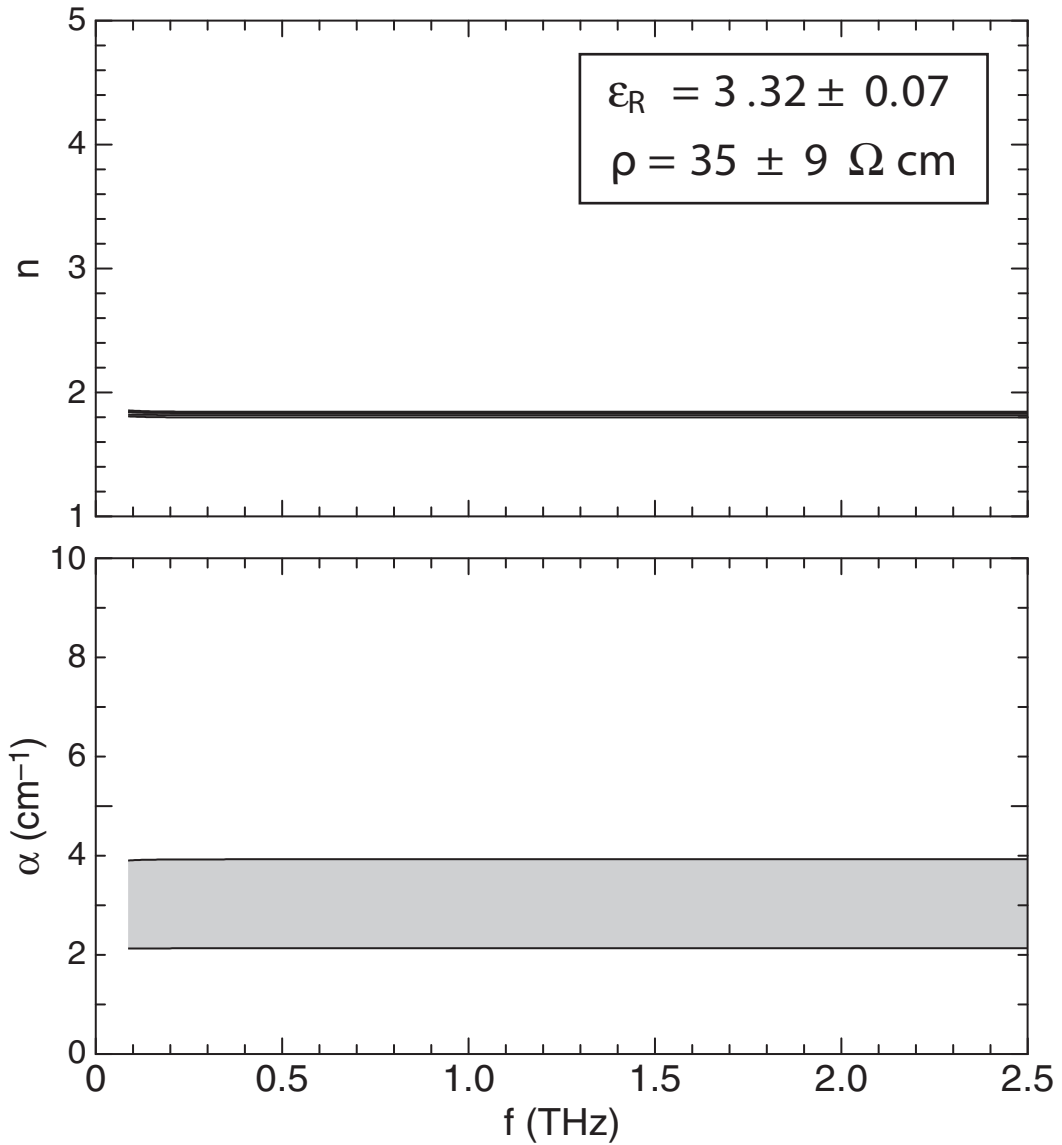
Figure 2.9: Experimentally derived refractive index and absorption coefficient of oxidized porous silicon. Generated with best fitted parameter of Eq.2.11, where $\varepsilon_\infty = 3.32 \pm 0.07$ and $\rho = 35 \pm 9\,\Omega \cdot \text{cm}$. Grey area represented the standard deviation of calculated refractive index and absorption coefficient

a direct comparison between their result and ours. However, their report also suggested that microporous silicon is transmissive in terahertz domain($\alpha \sim$tenths of cm^{-1}). Hence we see that oxidized porous silicon made from highly doped silicon is stable, surprisingly low loss and featureless in the terahertz spectrum which in turn show that it could be an excellent optical material for terahertz applications.

Chapter 3

Multilayered Terahertz Filters

In this chapter, we report our research in utilizing porous silicon as a material for multilayered filtering. We start in Sec. 3.1 by giving an overview of the transfer matrix method, which is the standard method for analyzing multilayered filters. While we only discuss the case of distinct layers, the method can also be applied to graded-index layers for which there is no distinct boundary by dividing the graded index layers into thin regions that are each modeled as homogeneous layer. This is important as one of the key advantages of porous silicon as filtering material of choice versus other materials described in Sec. 1.1 is that the refractive indices of porous silicon can be continuously adjusted by changing the applied current, as explained in Sec. 1.2. In Sec. 3.2, we describe our effort in demonstrating the filtering capability of porous silicon material. As a proof of concept, we demontrate a simple Bragg grating bandpass filter, however the method is expected work with more complicated filtering structures as well.

3.1   Transfer matrix method

When an electromagnetic(EM) wave is traveling in multilayered structure, each interface it encounters can reflect a certain amount of the field while allowing the other portion to be transmitted through the interface. Depending on the thickness of the layer, the reflected

waves from successive interfaces can interfere constructively or destructively, leading to a frequency-selective reflection spectrum, the net effect is that certain frequencies of the incident field spectrum could be reflected completely while others would be partially reflected or transmitted completely. This effect could then be used for filtering purpose or to create nearly lossless dielectric mirror.

In this section, we give a summary on the transfer matrix method that is used for the analysis of multilayered structures. The complete derivation, while outside the scope of this thesis, could be found in Ref. [176], and alternative methods could also be found in Refs. [177, 178]. For ease of discussion, we first restrict the propagation angle to normal incidence, later in this section, we will extend the discussion to the more general case of oblinque angles of incidence.

We first assume an overall transverse field $E_T(z)$ and $H_T(z)$ which are defined in terms of a left propagating field $E_{T+}(z)$ and a right propagating field $E_{T-}(z)$. Here, the z-axis marked the propagation direction. The plane x-z is the incident plane with y-axis perpendicular to the incident plane and is pointing outward as shown in Fig. 3.1.

$$
\begin{aligned}
E_T(z) &= E_{T+}(z)\exp(-j\beta z) + E_{T-}(z)\exp(j\beta z) \\
H_T(z) &= \frac{1}{\eta_T}[E_{T+}(z)\exp(-j\beta z) - E_{T-}(z)\exp(j\beta z)],
\end{aligned}
\tag{3.1}
$$

where E_{T+}, E_{T-} are the electric field propagating in the forward and backward direction respectively and the transverse impedance η_T is given by $\eta_T = \frac{\eta_0}{n}$ with vacuum impedance $\eta_0 = 376.7\ \Omega$, and n is the refractive index of the material of interested.

We consider first the case of propagation of a normal incident wave as depicted in Fig. 3.1, we look at the case of a wave traveling from left to right while trying to calculate the electric field at a particular point z in reference with a later point z'.

Two additional parameters are introduced here for the convenience of calculation. The
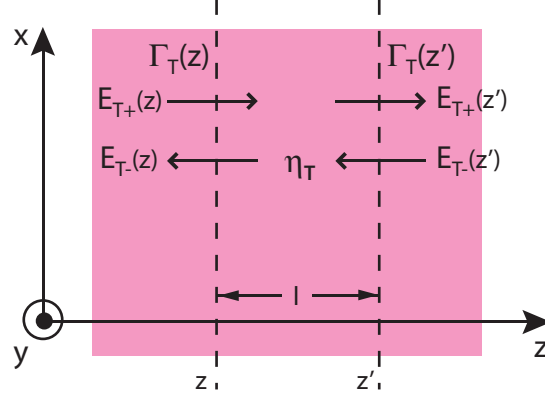
Figure 3.1: Propagation of a transverse electromagnetic field in a medium with impedance η

Parameters	Equations
$\begin{bmatrix} E_{T+}(z) \\ E_{T-}(z) \end{bmatrix}$	$\begin{bmatrix} e^{j\delta} & 0 \\ 0 & e^{-j\delta} \end{bmatrix} \begin{bmatrix} E_{T+}(z') \\ E_{T-}(z') \end{bmatrix}$
$\begin{bmatrix} E_T(z) \\ H_T(z) \end{bmatrix}$	$\begin{bmatrix} \cos\delta & j\eta\sin\delta \\ j\eta_T^{-1}\sin\delta & \cos\delta \end{bmatrix} \begin{bmatrix} E_T(z') \\ H_T(z') \end{bmatrix}$
$\Gamma_T(z)$	$\Gamma_T(z')e^{-2j\delta}.$
$Z_T(z)$	$\eta_T \frac{Z_T(z')+j\eta\tan\delta}{jZ_T(z')\tan\delta+\eta_T}$

Table 3.1: Equations for transverse field propagation in a single medium of impedance η_T

overall transverse wave impedance $Z_T(z) = \frac{E_T(z)}{H_T(z)}$, which allows us to visualize EM wave propagation in multilayered structures in terms of equivalent electric circuit and the overall transverse reflection coefficient $\Gamma_T(z) = \frac{E_{T-}(z)}{E_{T+}(z)}$ describes the overall reflection from an interface. Note that the terms $Z_T(z)$ and $\Gamma_T(z)$ define the contribution of all fields transmitted or reflected to the layer of interest and should not be confused with the material's transverse impedance η_T and the reflection coefficient ρ_T. Table 3.1 shows the propagation of the fields E_T, H_T from point z' to point z and the corresponding forward and backward fields E_{T+} and E_{T-}, impedance and reflection coefficient Z_T and Γ_T are transformed from z to z', as described in Ref. [176]. Here we also introduce the phase shift $\delta = \beta(z'-z) = \frac{2\pi}{\lambda}n(z'-z)$ with λ as the wavelength of the incident light.

At the interface between two mediums of impedance $\eta_{T,1}$ and $\eta_{T,2}$ as illustrated in Fig. 3.2, we assumed again a left propagating incident EM wave and calculate the fields at

medium 1 adjacent to the interface from adjacent fields at medium 2. The overall transmitted and reflected waves can be viewed as a combination of the effect of the transmission and reflection of a left incident wave (case 1 in Fig. 3.2) and the transmission and reflection of a right incident wave (case 2 in Fig. 3.2) by the interface and is shown in case 1+2 in Fig. 3.2. A summary of the fields vector , the corresponding E_+,E_- , $Z(z)$ and $\Gamma(z)$ are listed in Table 3.2 with the individual transverse transmission coefficient τ_T and the individual transverse reflection coefficient ρ_T given as

$$
\begin{aligned}
\tau_{T,1,2} &= \frac{2\eta_{T,2}}{\eta_{T,2}+\eta_{T,1}} \\
&= \frac{2n_{T,1}}{n_{T,1}+n_{T,2}} \\
&\equiv \frac{E_{T,2+}}{E_{T,1+}},
\end{aligned}
\tag{3.2}
$$

and

$$
\begin{aligned}
\rho_{T,1,2} &= \frac{\eta_{T,2}-\eta_{T,1}}{\eta_{T,2}+\eta_{T,1}} \\
&= \frac{n_{T,1}-n_{T,2}}{n_{T,1}+n_{T,2}} \\
&\equiv \frac{E_{T,1-}}{E_{T,1+}},
\end{aligned}
\tag{3.3}
$$

found by satisfying the boundary conditions of electromagnetic wave. Also note the following useful identities $\tau_{T,1,2} = 1+\rho_{T,1,2}$, $\rho_{T,2,1} = -\rho_{T,1,2}$, $\tau_{T,2,1} = 1+\rho_{T,2,1} = 1-\rho_{T,1,2}$ and $\tau_{T,1,2}\tau_{T,2,1} = 1-\rho_{T,1,2}^2$.

Strictly speaking, the results we shown so far is only valid for normal incidence, however one can prove that the result is equally applicable to fields that are incident in oblique angle by redefining the impedance and refractive index using Eqs. 3.4 and 3.5 and redefining the phase shift as $\delta = \beta l = \frac{2\pi}{\lambda}nl\cos\theta$ with l being the thickness of a layer and θ is the
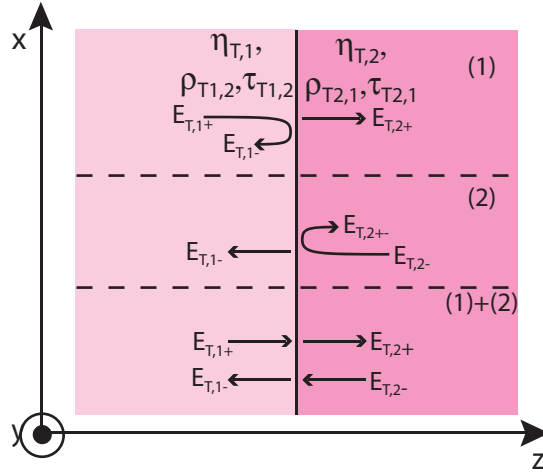
Figure 3.2: Transmission and reflection from an interface between two mediums with transverse impedance $\eta_{T,1}$ and $\eta_{T,2}$. Case 1: Transmission and reflection of a left incident wave only. Case 2: Transmission and reflection of a right incident wave only. Case 1+2: Transmission and reflection of an electromagnetic wave with left and right incident components.

Parameters	Equations
$\begin{bmatrix} E_{T,1} \\ H_{T,1} \end{bmatrix}$	$\begin{bmatrix} 1 & 0 \\ 0 & 1 \end{bmatrix} \begin{bmatrix} E_{T,2} \\ H_{T,2} \end{bmatrix}$
$\begin{bmatrix} E_{T,1+} \\ E_{T,1-} \end{bmatrix}$	$\frac{1}{\tau_{T,1,2}} \begin{bmatrix} 1 & \rho_{T,1,2} \\ \rho_{T1,2} & 1 \end{bmatrix} \begin{bmatrix} E_{T,2+} \\ E_{T,2-} \end{bmatrix}$
$Z_{T,1}$	$Z_{T,2}$
$\Gamma_{T,1}$	$\frac{\rho_T + \Gamma_{T,2}}{1 + \rho_T \Gamma_{T,2}}$

Table 3.2: Equations for fields matching in between interface of two mediums of impedance $\eta_{T,1}$ and $\eta_{T,2}$

propagating angle to the normal of the interface.

$$
\eta_T =
\begin{cases}
\dfrac{\eta_0}{n}\cos\theta & \text{TM polarization} \\[3mm]
\dfrac{\eta_0}{n\cos\theta} & \text{TE polarization.}
\end{cases}
\tag{3.4}
$$

We can also define a transverse refractive index,

$$
n_T =
\begin{cases}
\dfrac{n}{\cos\theta} & \text{TM polarization} \\[3mm]
n\cos\theta & \text{TE polazation.}
\end{cases}
\tag{3.5}
$$

Hence, the behavior of a multilayered filter can be obtained by using the propagation and matching matrix for $\begin{bmatrix} E_T \\ H_T \end{bmatrix}$ or $\begin{bmatrix} E_{T+} \\ E_{T-} \end{bmatrix}$ recursively. The solution for $\begin{bmatrix} E_{T+} \\ E_{T-} \end{bmatrix}$ is particularly attractive as we could obtain the overall transmission or reflection coefficients from the resulting matrix easily. From table 3.1 and table 3.2,

$$
\begin{bmatrix} E_{T,i+}(z) \\ E_{T,i-}(z) \end{bmatrix}
=
\begin{bmatrix} e^{j\delta_i} & 0 \\ 0 & e^{-j\delta_i} \end{bmatrix}
\begin{bmatrix} E_{T,i+}(z') \\ E_{T,i-}(z') \end{bmatrix},
\qquad \text{Propagation matrix} \tag{3.6}
$$

$$
\begin{bmatrix} E_{T,i+} \\ E_{T,i-} \end{bmatrix}
=
\frac{1}{\tau_{Ti,i+1}}
\begin{bmatrix} 1 & \rho_{Ti,i+1} \\ \rho_{Ti,i+1} & 1 \end{bmatrix}
\begin{bmatrix} E_{T,(i+1)+} \\ E_{T,(i+1)-} \end{bmatrix},
\qquad \text{Matching matrix} \tag{3.7}
$$

with δ_i, the propagation phase shift in the i layer as

$$
\delta_i = \frac{\omega}{c} n_i l_i \cos\theta_i = \frac{2\pi}{\lambda} n_i l_i \cos\theta_i = \frac{2\pi}{\lambda} l_i n_i \sqrt{1 - \frac{n_a^2 \sin^2\theta_a}{n_i^2}}, \qquad i = 1, 2, \ldots M \tag{3.8}
$$

Fig. 3.3 illustrates a wave incident on an M-layer multilayer structure from the left, at
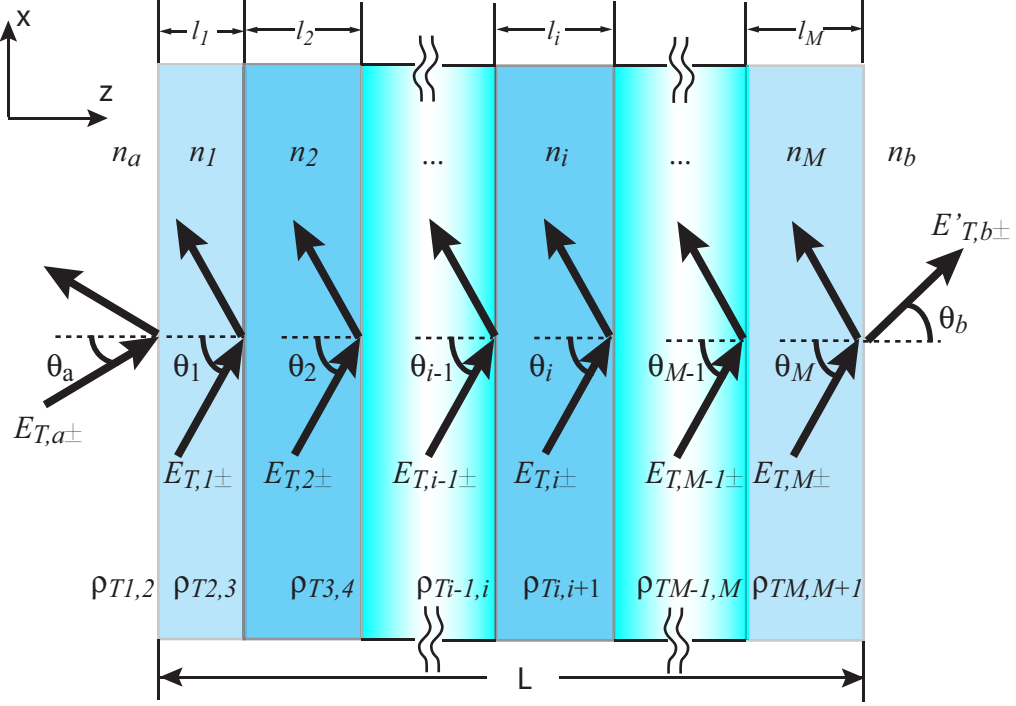
Figure 3.3: Oblique incidence on multilayer dielectric structure.

an angle of incidence θ_a. On the left side, part of the input wave E_{Ta+} is being reflected by the structure as E_{Ta-}. As there is no incident wave at the right side, the output vector could be written as $\begin{bmatrix} E'_{T,b,+} \\ 0 \end{bmatrix}$, which is exiting from the structure at an output angle of θ_b.

At any interface $i-1$ the field amplitudes can be calculated from the field amplitudes in the i layer using Eq. 3.6 and 3.7 ,

$$\begin{bmatrix} E_{Ti-1+} \\ E_{Ti-1-} \end{bmatrix} = \frac{1}{\tau_{Ti-1,i}} \begin{bmatrix} 1 & \rho_{Ti-1,i} \\ \rho_{Ti-1,i} & 1 \end{bmatrix} \begin{bmatrix} \exp(j\delta_i) & 0 \\ 0 & \exp(-j\delta_i) \end{bmatrix} \begin{bmatrix} E_{Ti,+} \\ E_{Ti,-} \end{bmatrix}, \quad (3.9)$$

with $i = 1, 2, \ldots, M$ denotes the different layers, a represents the input medium and b represents the output medium. The reflection coefficient ρ_i at each interface, is given by

56

Eq. 3.3 as

$$\rho_{Ti-1,i} = \frac{n_{T,i-1} - n_{T,i}}{n_{T,i-1} + n_{T,i}} \qquad i = 1, 2, \ldots, b.$$

With $i - 1, i$ represents the interface between layer $i - 1$ and layer i, $n_{T,0} = n_a$ and $n_{T,M+1} = n_b$. The transverse index of refraction of the i-th layer is given by

$$n_{Ti} = \begin{cases} \frac{n_i}{\cos \theta_i}, & \text{TM polarization} \\ \\ n_i \cos \theta_i, & \text{TE polarization} \end{cases}$$

Hence the relationship between the forward and backward fields $\begin{bmatrix} E_{T,a+} \\ E_{T,a-} \end{bmatrix}$ at $z = 0$

and the forward and backward fields $\begin{bmatrix} E_{T,b} \\ 0 \end{bmatrix}$ at $z = L$ is given by the matrix product

$$\begin{bmatrix} E_{T,a+} \\ E_{T,a-} \end{bmatrix} = \frac{1}{\tau_{Ta,1} \tau_{T1,2} \cdots \tau_{Ti,i+1} \cdots \tau_{T,M+1}} \begin{bmatrix} 1 & \rho_{Ta,1} \\ \rho_{Ta,1} & 1 \end{bmatrix} \begin{bmatrix} e^{j\delta_1} & 0 \\ 0 & e^{j\delta_1} \end{bmatrix}$$

$$\times \begin{bmatrix} 1 & \rho_{T1,2} \\ \rho_{T1,2} & 1 \end{bmatrix} \begin{bmatrix} e^{j\delta_2} & 0 \\ 0 & e^{j\delta_2} \end{bmatrix} \cdots \begin{bmatrix} 1 & \rho_{Ti-1,i} \\ \rho_{Ti-1,i} & 1 \end{bmatrix} \begin{bmatrix} e^{j\delta_i} & 0 \\ 0 & e^{j\delta_i} \end{bmatrix}$$

$$\times \cdots \begin{bmatrix} 1 & \rho_{TM,M+1} \\ \rho_{TM,M+1} & 1 \end{bmatrix} \begin{bmatrix} E_{T,b,+} \\ 0 \end{bmatrix}$$

$$= \begin{bmatrix} Q_{11} & Q_{12} \\ Q_{21} & Q_{22} \end{bmatrix} \begin{bmatrix} E_{T,b,+} \\ 0 \end{bmatrix} \tag{3.10}$$

The overall reflection coefficient of the multilayered structure can then be found by $\Gamma = \frac{E_{T,a-}}{E_{T,a+}} = \frac{Q_{21}}{Q_{11}}$ and the overall transmission coefficient is given by $T = \frac{E_{T,b+}}{E_{T,a+}} = \frac{1}{Q_{11}}$.

A similar procedure can be applied for lossy materials with some slight modifications.

For a lossy material, the dielectric constant and refractive index are given by

$$\varepsilon_i(\omega) = \varepsilon_{Ri}(\omega) - j\varepsilon_{Ii}(\omega)$$

$$n_i(\omega) = \sqrt{\frac{\varepsilon_i(\omega)}{\varepsilon_0}} = \sqrt{\frac{\varepsilon_{Ri}(\omega) - j\varepsilon_{Ii}(\omega)}{\varepsilon_0}} = n_{Ri}(\omega) - jn_{Ii}(\omega). \qquad (3.11)$$

As the refractive index of the layer is complex, the derived propagation angles inside layers are also complex. This problem can be solved by simply rearranging the term in Eq. 3.8 to be in term of the incident angle θ_a, which by definition is real,

$$\delta_i = k_{zi}l_i = 2\pi\frac{f}{f_0}\frac{l_i}{\lambda_0}\sqrt{n_i^2 - n_a^2\sin^2\theta_a}$$

$$\cos\theta_i = \sqrt{1 - (\frac{n_a}{n_i}\cos\theta_a)^2}$$

We can the substitute the calculated complex phase shift that incorporates loss and the complex refractive index into Eqs. 3.6 and 3.7 as with the lossless case.

3.1.1 Transmission of EM wave from a single dielectric layer

As was discussed in Sec. 1.1, the refractive index of a sample is measured by dividing the measured fourier transformed E-field with the sample inserted into the beam path $E_{Sam}(\omega)$ by the measured fourier transformed E-field without the sample $E_{Ref}(\omega)$. Here we consider the well-known problem of transmission of radiation through a single dielectric slab of known thickness l, surrounded on both sides by air (n=1). Because the terahertz time-domain measurements provide the real and imaginary transmission coefficient, the experimental measurements can be used to extract the complex refractive index of the sample of interest. The transfer matrix method introduced in this section can of course be used to obtain an expression for the transmission through a single-layer dielectric, but a more

insightful derivation is obtained by tracing the propagation of EM wave with multiple reflections and summing all of the emerging fields at output interface as depicted in Fig. 3.4.
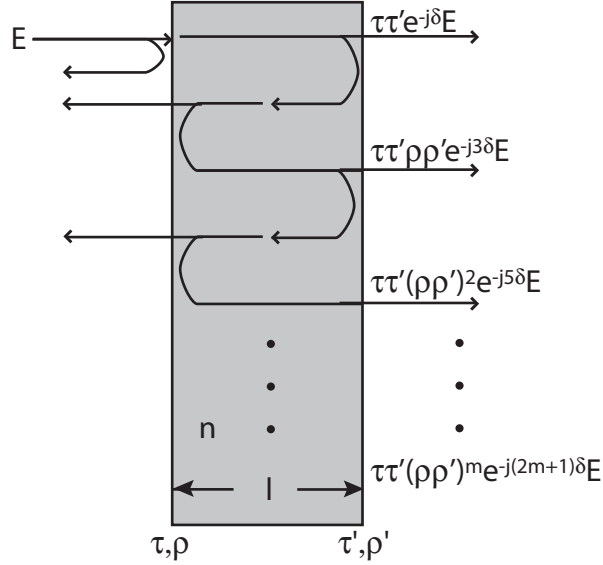
Figure 3.4: The propagation of an EM wave through a single dielectric layer. At the output interface, part of the beam is transmitted and the other part reflected. The reflected EM wave is then partially reflected at the input interface and is partially transmitted then at the output interface again with the cycle continuous until all the EM wave exitted from the sample either from input interface or output interface or in the case of lossy material, absorbed by the sample.

From Fig. 3.4, we can immediately see that the transmission coefficient of the sample is given by

$$
\begin{aligned}
T(\omega) &= \tau(\omega)\tau'(\omega)e^{-j\delta(\omega)}\{1 + \rho(\omega)\rho'(\omega)e^{-j2\delta(\omega)} + \left[\rho(\omega)\rho'(\omega)e^{-j2\delta(\omega)}\right]^2, \\
&+ \cdots \left[\rho(\omega)\rho'(\omega)e^{-j2\delta(\omega)}\right]^m + \cdots\} \\
&= \tau(\omega)\tau'(\omega)e^{-j\delta(\omega)}\sum_{m=0}^{m=\infty}\left[\rho(\omega)\rho'(\omega)e^{-j2\delta(\omega)}\right]^m,
\end{aligned}
\tag{3.12}
$$

where $\tau(\omega)\tau'(\omega) = \frac{4n(\omega)}{[n(\omega)+1]^2}$, $\rho(\omega)\rho'(\omega) = -\left[\frac{n(\omega)-1}{n(\omega)+1}\right]^2$ and $\delta(\omega) = n(\omega)\frac{\omega}{c}l$. We also see that the bracketed part of Eq. 3.12 is a geometric series with sum identity for infinite

59

series $\sum_{k=0}^{\infty} ar^k = \frac{a}{1-r}$ for $|r| < 1$, we get

$$
\begin{aligned}
T(\omega) &= \tau(\omega)\tau'(\omega)\frac{e^{-j\delta(\omega)}}{1+\rho(\omega)\rho'(\omega)e^{-j2\delta(\omega)}} \\
&= \frac{4n(\omega)}{[n(\omega)+1]^2}\frac{e^{-jn(\omega)\frac{\omega}{c}l}}{1+\left[\frac{n(\omega)-1}{n(\omega)+1}\right]^2 e^{-j2n(\omega)\frac{\omega}{c}l}},
\end{aligned}
\tag{3.13}
$$

We see that the comparison between measured E-field with sample ($E_{Sam}(\omega)$) and measured E-field without sample ($E_{Ref}(\omega)$) is basically the comparison between transmission of a sample with thickness l and unknown refractive index $n(\omega)$ and another sample of same thickness l and refractive index $n(\omega) = 1$, we have

$$
\frac{E_{Sam}(\omega)}{E_{Ref}(\omega)} = \frac{4n(\omega)}{[n(\omega)+1]^2}\frac{e^{-j[n(\omega)-1]\frac{\omega}{c}l}}{1+\left[\frac{n(\omega)-1}{n(\omega)+1}\right]^2 e^{-j2n(\omega)\frac{\omega}{c}l}},
\tag{3.14}
$$

which gives the complex transmission function of the sample. In the time-domain, the effect of multiple reflections gives rise to multiple echos in the observed temporal response (Fig. 3.5). In practice, it is impossible to measure all of the echos, especially for an optically thick sample. When a limited number of echos are used, then the transmission function can be instead be modeled by replacing the infinite summation with a finite summation, depending on how many echos can be observed:

$$
\frac{E_{Sam}(\omega)}{E_{Ref}(\omega)} = \frac{4n(\omega)}{[n(\omega)+1]^2}e^{-j[n(\omega)-1]\frac{\omega}{c}l}\sum_{0}^{m}(-1)^{2m}\left[\frac{n(\omega)-1}{n(\omega)+1}\right]^2 e^{-j2n(\omega)\frac{m\omega}{c}l},
\tag{3.15}
$$

where m is the numbers of reflected pulses in the time domain trace of the field $E_{sam}(t)$.
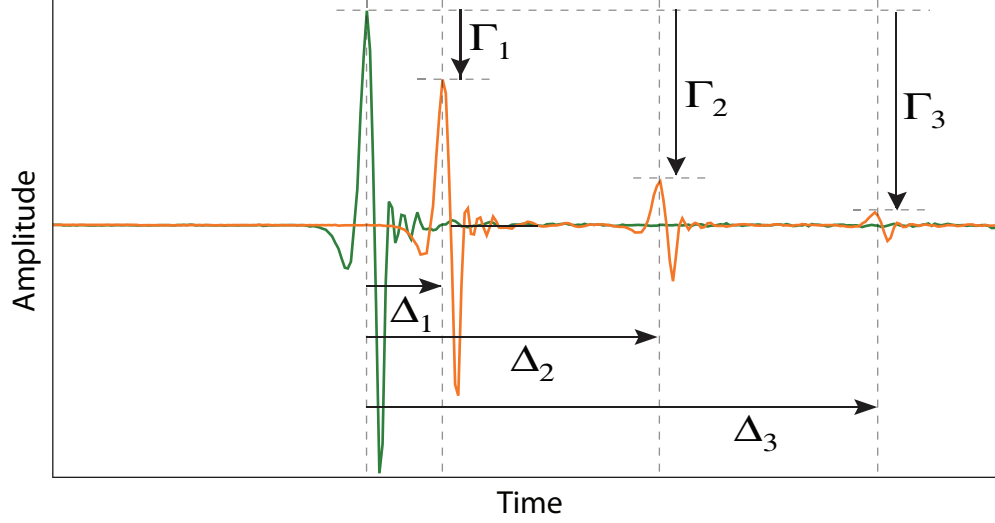
Figure 3.5: Simulated terahertz respondse from a single lossless dielectric sample. The layer has a dielectric constant of $\varepsilon = 11.7$ and thickness of $300\,\mu$m. Green line illustrates the terahertz measurement without the sample in the beam path. Orange line illustrates the terahertz signal with the sample inserted into the beam path. Multiple pulses in the sample trace is clearly seen and are attributed to multiple reflections at both interfaces of the sample. The time delayed, Δ_m for each reflected pulse numbered $m = 1, 2, 3$ is given by the expression $\Delta_m = \frac{(m \cdot \sqrt{\varepsilon} - 1)}{c} l$, the reduces in amplitude Γ_m is given by $\Gamma_m = 1 - \tau \tau' (\rho \rho')^{m-1}$.

3.1.2 Quaterwave and halfwave stacks

The case of dielectric layers with thickness of $\frac{\lambda}{4n}$ and $\frac{\lambda}{2n}$ is very important for the design of multilayered filters. From Eq. 3.8, the resultant phase terms in Eq. 3.9 are -1 for $l = \frac{\lambda}{4n}$ or 1 for $l = \frac{\lambda}{2n}$. Hence we could immediately see that at the designated wavelength, all EM fields propagating in the quaterwave stacks($l = \frac{\lambda}{4n}$) would interfered destructively as the EM field propagated through the stack. If the number of layers is large, all of the incident EM field is reflected by the stack and no transmission is possible at this wavelength. On the other hand, for the halfwave stack($l = \frac{\lambda}{2}$), if the numbers of layers is large, all EM fields are interfered constructively and all of the incident EM field is transmitted as if the halfwave stack did not exist. Hence, one can use the quaterwave stack for creating near perfect dielectric mirror while using the halfwave for creation of a resonance cavity or using combination of quaterwave and halfwave plates as filter or matching element between materials with different refractive index. The list of applications is outside the scope of
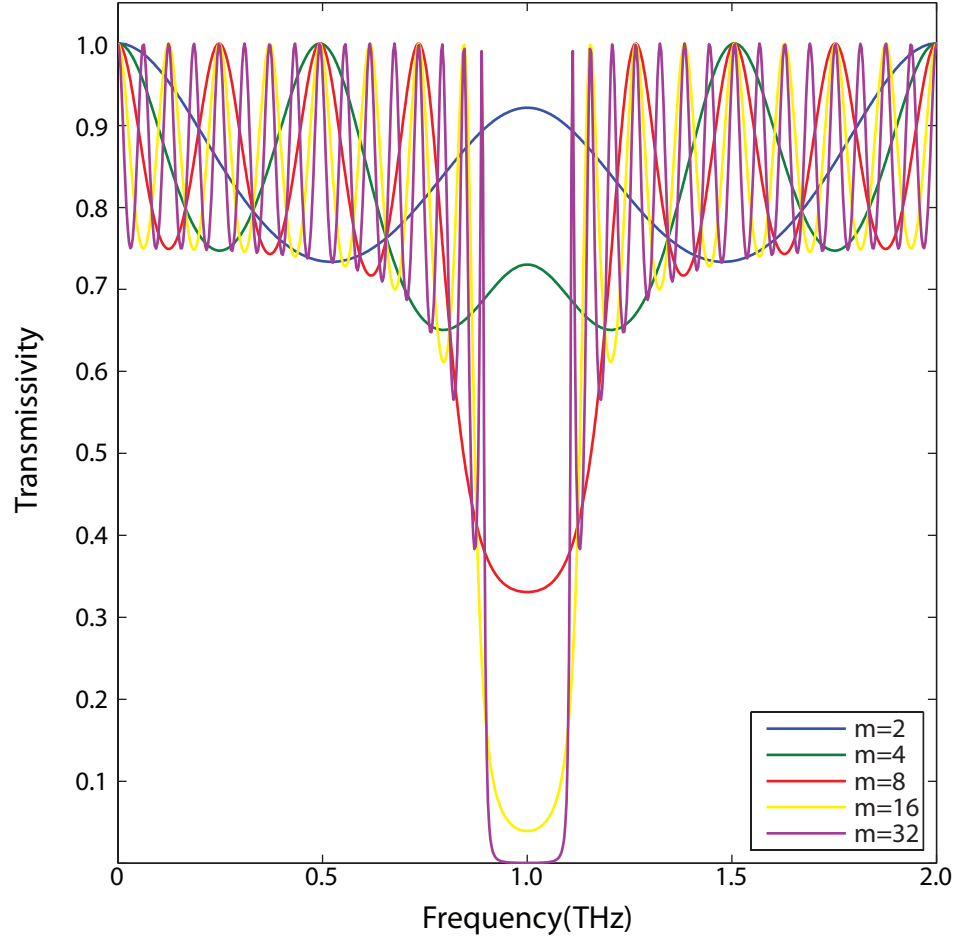
Figure 3.6: Power transmission ratio of alternative quaterwave layers of $n_H = 2.0$, $n_L = 1.5$ and $f_0 = 1$ THz of different numbers of layers.

this thesis, but Refs. [176, 177] give some examples of particular applications. Here in this thesis, our interest lies solely on the proving that porous silicon could be used as a multilayered filtering material, hence we only consider the simplest case of alternating quaterwave stacks with refractive indices of n_H and n_L.

In Fig. 3.6, we show the transmissivity of quaterwave stacks with the $n_H = 2.0$ and $n_L = 1.5$ with different number of layers. For the design frequency of 1 THz, we could calculate that the desired thickness for $n_H = 2.0$ and $n_L = 1.5$ are $l = \frac{300\,\mu\text{m}}{4\cdot 2} = 37.5\,\mu\text{m}$ and $l = \frac{300\,\mu\text{m}}{4\cdot 1.5} = 50\,\mu\text{m}$, respectively. As the numbers of layers increased, the transmissivity of the quaterwave stack at the designated frequency decreased from 0.92 for $m = 2$ to 0.0004 for $m = 32$ as more waves is being reflected due to the increased number of interfaces.
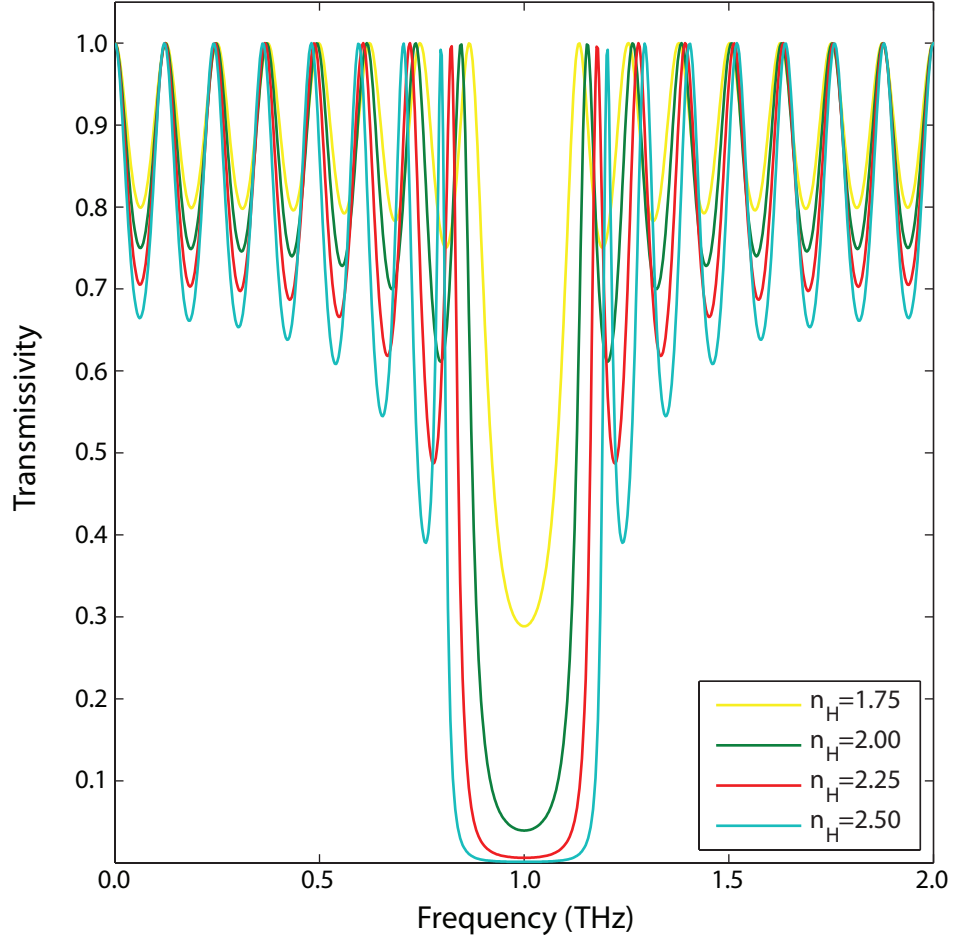
Figure 3.7: Power transmission ratio of alternative quaterwave layers with the same number of layers $m = 16$, $n_L = 1.5$ and $f_0 = 1$ THz and variable n_H from $1.75 - 2.50$.

On the other hand, by increasing the ratio $\frac{n_H}{n_l}$, we increased the reflection at each interface, hence the overall reflection is increased although the number of layers remains the same. The situation is shown in Fig. 3.7, with $n_L = 1.5$, $f_0 = 1$ THz, n_H is varied from 1.75 to 2.5 in steps of 0.25, as the quaterwave lengths are inversely proportional to the refractive indices, d_H changed from 42.86 μm for $n_H = 1.75$ to 30 μm for $n_H = 2.50$. At the designated frequency, the transmissivity reduced from 0.2885 for $n_H = 1.75$ to 0.0011 for $n_H = 2.5$ for the same number of layers $m = 16$.

An analytical expression is derived in Ref. [177], for a quaterwave stacks, the maximum reflectivity is given by

$$\Gamma^2 = \frac{1 - \left(\frac{n_H}{n_L}\right)^m \frac{n_H^2}{n_a n_b}}{1 + \left(\frac{n_H}{n_L}\right)^m \frac{n_H^2}{n_a n_b}}. \tag{3.16}$$

3.2   Experimental results

As a proof of concept [24], we had constructed a porous silicon based Bragg grating filter for terahertz frequencies. We first start with two single-layer samples etched with two different current densities $J_H = 18\,\mathrm{mA/cm^2}$ for the high index sample and $J_L = 90\,\mathrm{mA/cm^2}$ for the low index sample. The etching current was applied in pulses of 0.1 s with delay of 0.3 s and the etchant solution is mixed with volume ratio of hydrofluoric acid:water:ethanol = 1:1:2. The thickness of both samples was 285 μm. The etch rate for J_H was found to be around 0.3 μm/s and for J_L is around 1.0 μm/s. After completion of the etching process, a high current of $226\,\mathrm{mA/cm^2}$ is applied to the sample for 7 s such that samples are separated from the bulk silicon substrate. The samples are then rinsed in DI water, flushed clean with DI water, ethanol and isopropanol and left air dried. Following the procedure developed in Chap. 2, we oxidized the surface of these samples by Rapid Thermal Oxidation at $400\,^\circ$C for 5 mins before measuring their dielectric properties in terahertz frequency.

Fig. 3.8 shown the terahertz transmission spectrum of the two samples. A downward trend is observed in the transmission amplitude and is believed to be due to the broadening of phonon absorption peak by phonon confinement effect in porous silicon skeleton. Due to its off peak nature, we can model such behavior by simply using a two parameter models which could be obtained by Taylor expansion of the proper phonon absorption model Eq. 2.9.

$$\varepsilon(\omega) = A + iB\omega. \tag{3.17}$$

The simpler model of Eq. 3.17 is prefered then the more complicated Eq. 2.9 due to the restriction of the measurable frequency range of the system. As the phonon peak is far from
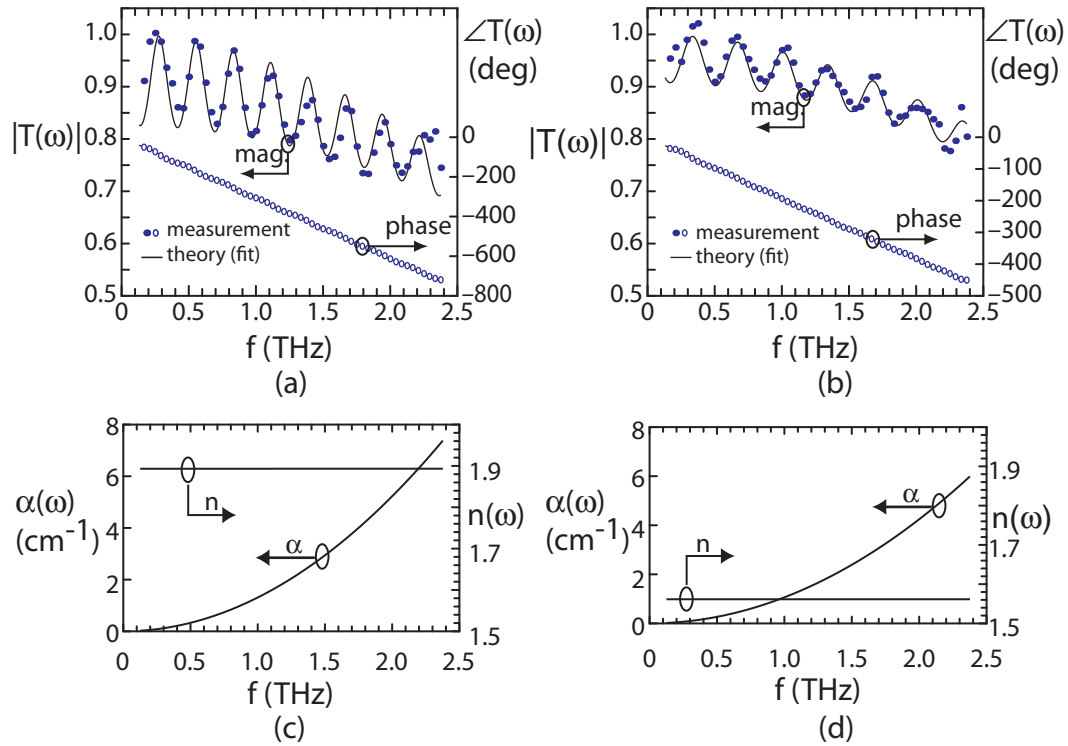
Figure 3.8: Measured and theoretical terahertz transmission spectrum for free-standing single layer porous silicon samples with (a) low porosity(~40%) and (b) high porosity(~62%). The theoretical curves were obtained by fitting to the experimental observations, using the index model given in Eq. 3.17. (c), (d) The corresponding refractive indices and attenuation coefficients determined from the theoretical fits shown in (a) and (b), respectively.

the measured frequency range, it is much difficult to achieve reliable fitting with Eq. 2.9. We determined the coefficients A and B with the transmission coefficient Eq. 3.15, using the dielectric function give in Eq. 3.17 and in similar procedure as in Sec. 2.2.2 except for the dielectric model.

As shown in Fig. 3.8(a),(b), the theoretical fits are found to give excellent agreement with the experiemental data, both in amplitude and phase. Using these two sets of A and B parameters, we can then calculate the estimated refractive indices and absorption coefficients of the two samples as shown in Fig. 3.8(c),(d). Hence , we found that the refractive index for sample etched with J_H is $n_H = 1.9$ and for sample etched with J_L is $n_L = 1.56$. The absorption coefficient, increases with frequency, but remains below 10 cm^{-1} for the entire detectable range of our terahertz setup.

Using these two sets of parameters, we then designed and fabricated a 13 layer sample by alternating between J_H and J_L. The thickness of each layer is designed such that $d_{H,L} = \frac{\lambda_0}{4n_{H,L}}$ where λ_0 is the targeted center wavelength, which is 1.17 THz in this case and hence the thickness for $d_H = 34\ \mu$m and for $d_L = 41\ \mu$m. Fig. 3.9 shown an SEM cross section view of the sample fabricated under this design. For this particular sample, we observed that the layer thicknesses decrease slightly as a function of depth into the sample. This reduction is atributed to the reduced etchant flow rate to the etchant into the deeper layers. A method to remedy such unwanted trend is by slightly increase the delay between applied pulses when etching the deeper layers. Rather than applying a strong current pulse to separate the multilayer from the substrate, we instead etched all the way through the substrate until the electrochemical cell showed a strong conduction between the two chambers, indicating that the etching had completed. Because the etching stopped immediately when any of the pores reach the other side of the wafer, we found thata thin layer of bulk silicon is often left-behind at the back side of the wafer. This bulk silicon layer can be removed by reactive ion etching with a CF_4/O_2 plasma until all the bulk silicon is visibly removed.

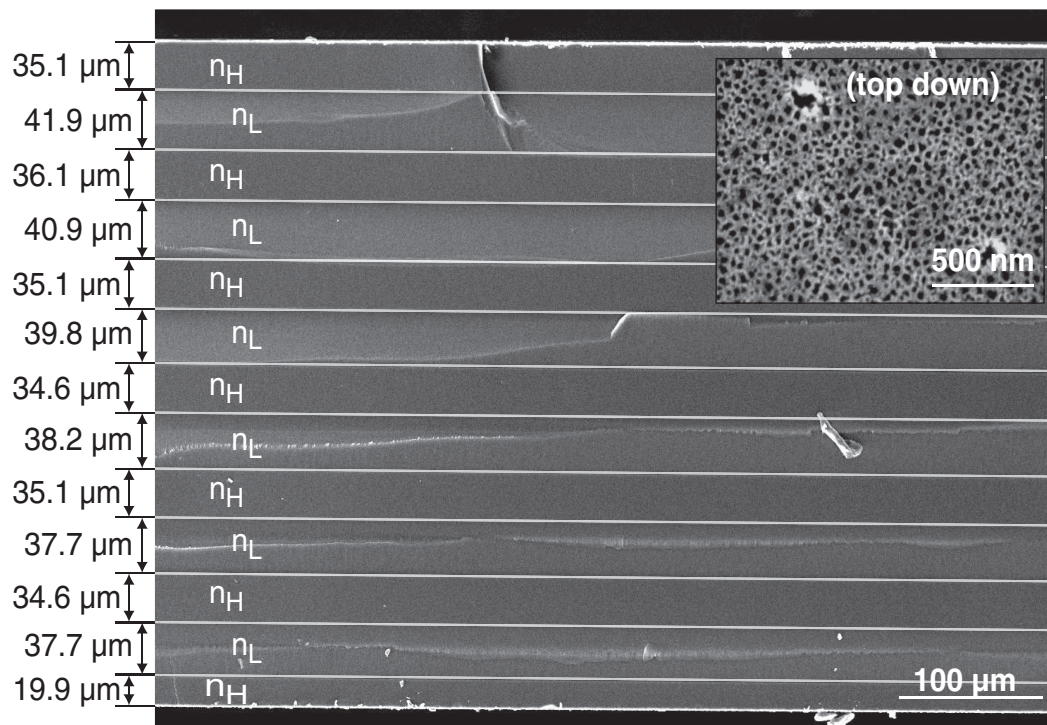Fig. 3.10 shown the two THz configurations for measuring the transmission and re-

Figure 3.9: Cross-sectional scanning electron micrograph of 13-layer porous silicon Bragg grating filter, comprised of alternating high and low refractive index layers. Inset: top-down scanning electron micrograph showing nanoscale structure of porous material.

flection spectrum of our porous silicon Bragg grating. For the transmission setup, the configuration is the same as described in Fig. 1.1. For the reflection spectrum, we rearrange the THz optics such that the incoming THz beam is at an angle of $\sim 20°$ to the normal of the sample in TE polarization. The reflected signal is then collected by a second parabolic mirror that is pointing to the sample at the same angle but opposite to the incoming mirror.

In Fig. 3.11, we show the spectrum of the reflective spectrum of the reflective setup, measured by putting a gold mirror in place of the sample. Comparison between Fig. 3.11 and Fig. 1.2(b) verified that the reflected THz signal is unobstructed.

Fig. 3.12 shown the transmission and reflection coefficient of the 13 layer Bragg grating shown in Fig. 3.9. The theoretical lines are calculated using transfer matrix method described in Sec. 3.1 and the dielectric constant model of Eq. 3.17 with the two sets of A and B from our single layer measurements. Slightly better result could be obtained by using the two sets of A and B from single layer measurement as the starting value and least-square fit the calculated transmission to the experimental one to determined the best set of A and B for each individual layer. In mathematics form, we seek to minimize the error between the measured transmission and the calculated transmission from Eq. 3.10,

$$\frac{E_{Sam}(\omega)}{E_{Ref}(\omega)} = T_{meas}(\omega)e^{j\frac{\omega}{c}L}, \tag{3.18}$$

$$T_{calc}(\omega, A_i, B_i) = \frac{1}{Q_{11}(\omega, A_i, B_i)}, \tag{3.19}$$

$$Minimized \sum_{\omega} W(\omega) \cdot (T_{calc}(\omega, A_i, B_i) - T_{meas}(\omega))^2, \tag{3.20}$$

with L the total thickness of the multilayered filter, Q_{11} obtained from Eq. 3.10, $W(\omega)$ the weighted function, usually the THz spectrum of the E-field without sample is used, A_i, B_i are A and B for each layer i with starting value found by single layer measurement previously mention.

68
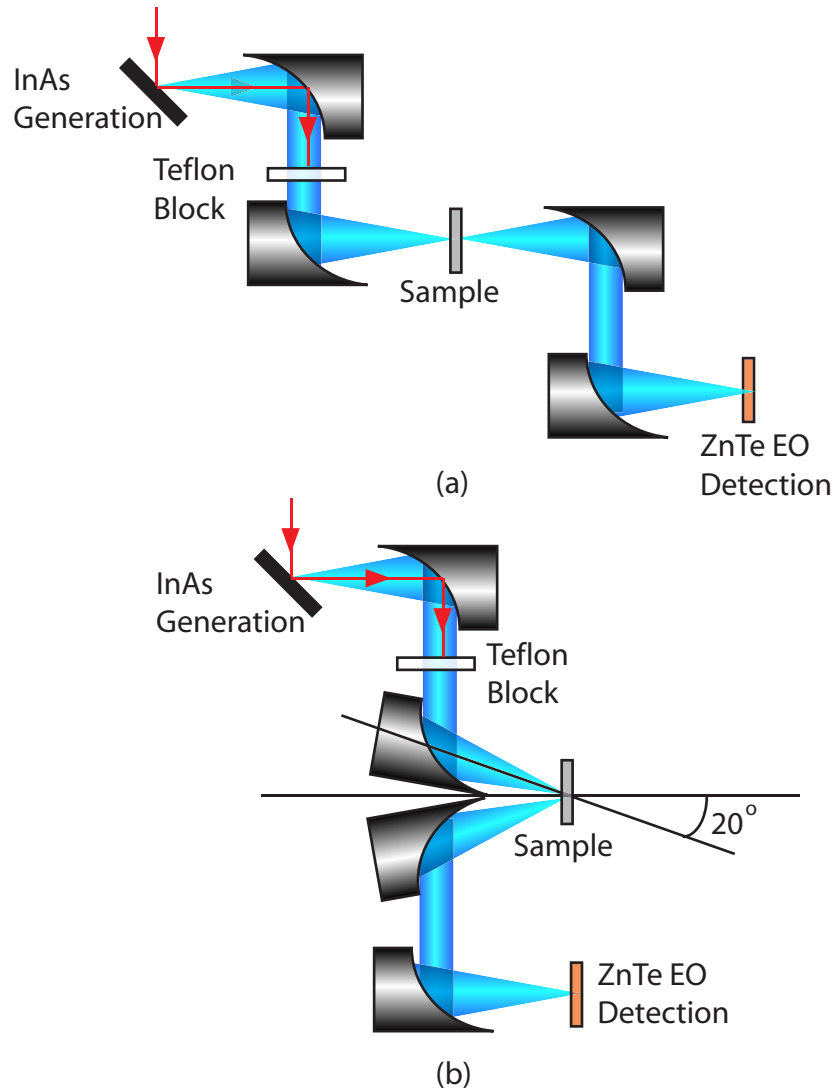
Figure 3.10: Simplified Terahertz setup diagram for measurement of transmission and reflection spectrum of porous silicon multilayer Bragg Grating. a. Transmission setup similar as Fig. 1.1. b. Reflective setup with two parabolic mirrors at 20° to the sample.
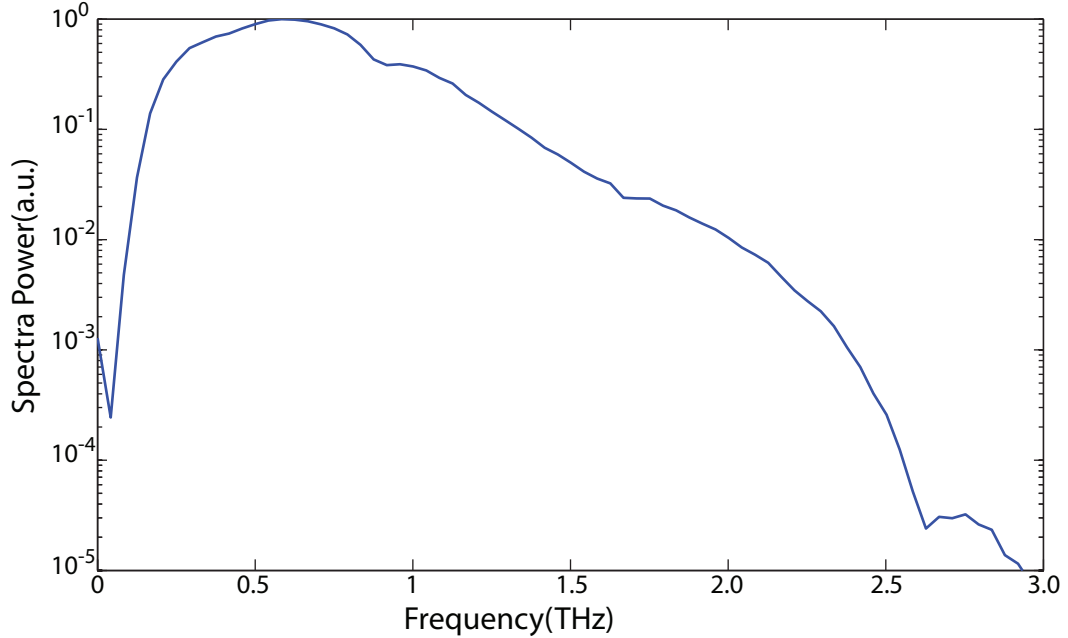
Figure 3.11: Reflection spectrum of a gold mirror measured with reflective setup shown in 3.10(b)

For the reflection curves, we calculated the case for normal incident and $20°$ for TE-polarization. The peak reflection occurred at 1.17 THz with $|R|^2 = 1 - (0.21)^2 = 93\%$ THz signal reflected. The full wave half maximun of this reflection peak is ~ 0.26 THz.

3.3   Conclusion

We demonstrated the capability of porous silicon as a multilayered filter at terahertz frequencies. As the loss in low frequency is low as suggested in Fig. 3.8, it is believed that such filter could work well at lower frequency of subterahertz as long as a filter can be fabricated. For very low targeted frequency, the thickness of the starting silicon wafer could becomes an issue. The problem could be remedied, however by stacking and assembling several multilayered stacks. The possibility of using porous silicon as filter for higher frequency could be limitted by the stronger absorption in high frequency. It is unclear whether the increase in absorption is due to the fundamental silicon phonon peak at 18 THz or other absorption peaks of silicon or impurities as our measurement is bounded by the detectable

70
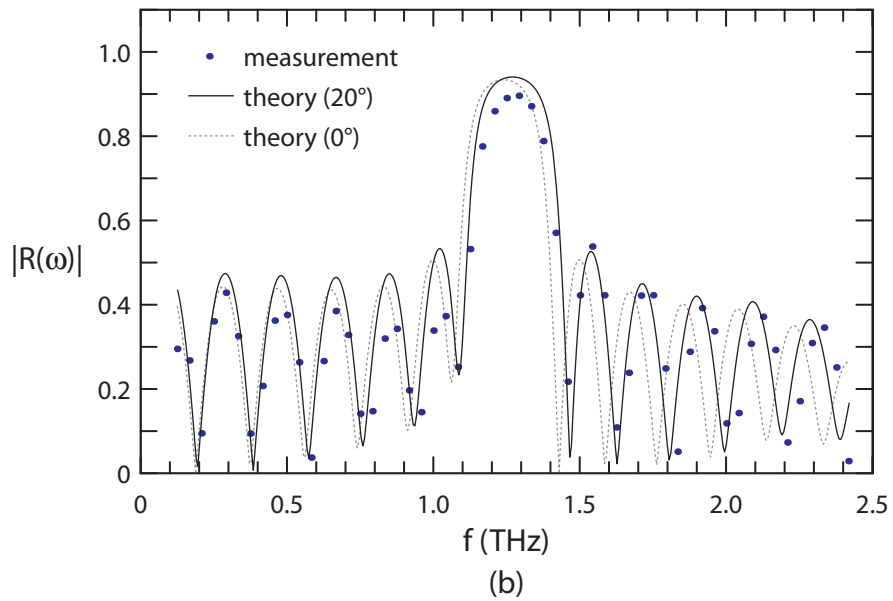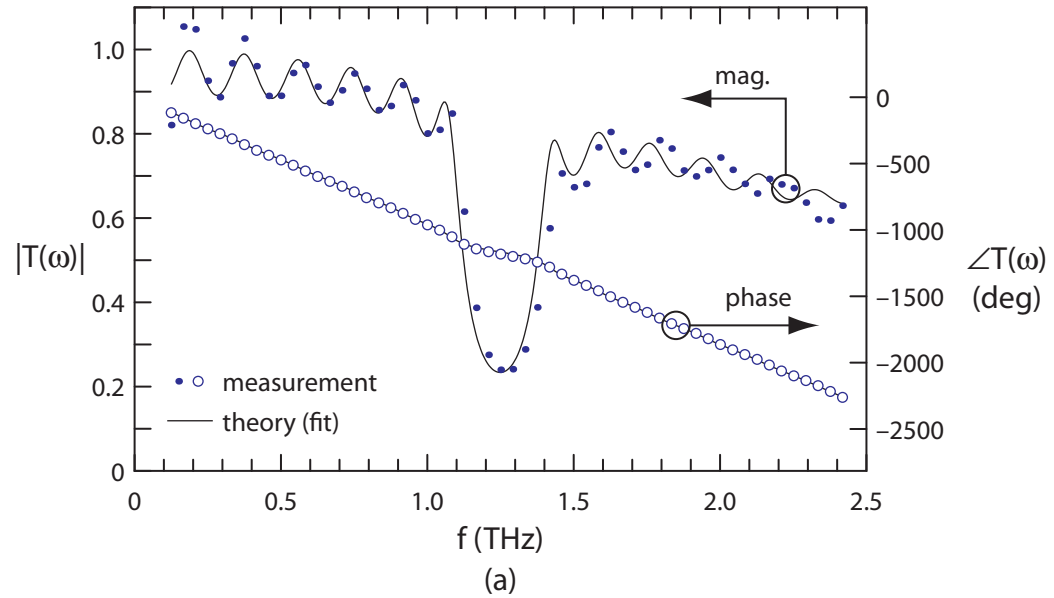
Figure 3.12: Terahertz transmission and reflection spectra of porous silicon Bragg filter. The solid curves indicate a theoretical calculation based on the measured film thicknesses and separately measured layer properties.

frequency range of our terahertz spectroscopy system. Nonetheless, the sample exhibits low loss of $< 10 \, \mathrm{cm}^{-1}$ in the detectable range of $0 - 2.5$ THz, hence there should be no foreseeable problem in filtering terahertz spectrum up to 2.5 THz. The behavior of the off-peak dielectric model seem to match with Ramani et. al. [146] at high frequency regime, although the corresponding conductivity is about one-tenths of what they reported. The vast different in conductivity is believed to be due to the thermal oxidation process.

Hence, we shown in this chapter that porous silicon is a viable material for fabrication of terahertz multilayered filter. As the porosity and the layer thickness can be easily controlled by switching etching currents, porous silicon based multilayered filter could serve an important part in manipulation of electromagnetic wave in terahertz regime.

Chapter 4

Terahertz Surface Plasmon Propagation in Nanoporous Layers

In this chapter, we report our demonstration of surface plasmon propagation on highly doped silicon wafers with and without porous silicon layers. We begin in Sec. 4.1 by explaining the familiar expression for surface plasmon propagation between a semi-infinite conductor and a semi-infinite dielectric medium. Having established the theoretical background, we repeated the earlier published works of Saxler et al. [179, 180] on the propagation of surface plasmon on gold and highly doped silicon. Ultimately our motivation is on utilizing the pore nature of porous silicon as a biosensing device, hence the main focus here is on creating a terahertz waveguide in which the radiation is confined in a nanoporous layer. In Sec. 4.2, we analyze the propagation of surface plasmons on a conductor that is covered with an additional dielectric layer. We will see that in this case, the dielectric layer causes dispersion of the surface plasmon wave. We compare experimental measurements of propagating surface plasmons to theoretical simulations, and show good agreement between the two.
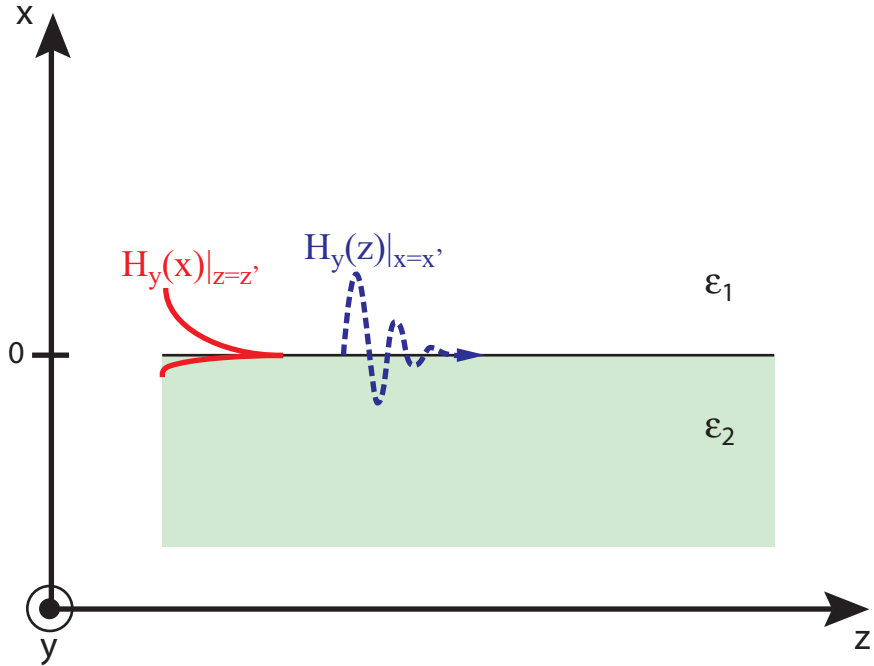
Figure 4.1: Surface plasmon field at the interface between a conductor and dielectric. The red line illustrates that the component of surface plasmon field that is evanescantly decays in the direction perpendicular to the surface. The blue dotted line shows that the propagating field propagates sinusoidally with an exponentially decayed envelope.

4.1 Surface Plasmons-Background

To begin, we consider the boundary between a conductor and dielectric, as shown in Fig. 4.1. We define the x axis as the direction perpendicular to the interface between the two media and the z axis as the direction of a propagating surface plasmon wave. We will first consider the case where EM wave is polarized in the x direction(TM) when the real part of the dielectric constant in medium 2 is negative (i.e. a conductor). Later on, we will mathematically prove a similar solution for TE (y-polarized) wave does not exist.

We begin with the classical Maxwell equations,

$$\nabla \times \mathbf{E} = -\frac{\partial}{\partial t}\mathbf{B}, \tag{4.1}$$

$$\nabla \cdot \mathbf{D} = \rho, \tag{4.2}$$

$$\nabla \times \mathbf{H} = \mathbf{j} + \frac{\partial}{\partial t}\mathbf{D}, \tag{4.3}$$

$$\nabla \cdot \mathbf{B} = 0, \tag{4.4}$$

Where the fields $\mathbf{D}$ and $\mathbf{H}$ are related to the electric field $\mathbf{E}$ and magnetic field $\mathbf{B}$ by $\mathbf{D} = \varepsilon \varepsilon_0 \mathbf{E}$ and $\mathbf{H} = \frac{1}{\mu \mu_0}\mathbf{B}$ respectively. In free space, the charge density ρ and current density $\mathbf{j}$ can be accounted for by making the dielectric constant complex. With this assumption of time varying component of the dielectric constant is much smaller then the time varying fields, Eqs. 4.1-4.4 can be reduced to two decoupled second order equations by substituting into one another and using the identity $\nabla \times (\nabla \times \mathbf{A}) = \nabla(\nabla \cdot \mathbf{A}) - \nabla^2 \mathbf{A}$,

$$\nabla^2 \mathbf{E} = -\frac{\mu \varepsilon}{c^2}\frac{\partial^2}{\partial t^2}\mathbf{E}, \tag{4.5}$$

$$\nabla^2 \mathbf{H} = -\frac{\mu \varepsilon}{c^2}\frac{\partial^2}{\partial t^2}\mathbf{H}. \tag{4.6}$$

As we are only interested in a propagating wave solution with TM polarization, we assume a general solution of the form

$$\mathbf{H}(x,z,t) = e^{i(\beta z - \omega t)}H_y(x)\hat{e}_y,$$

which described a propagating $\mathbf{H}$-field that is polarized in x direction with complex propagation constant of β, a mode envelope function of $H_y(x)$ and an angular frequency of $\omega = 2\pi f$. We can then substitute this trial solution into Eq. 4.6 and obtain the following equation for the envelope function $H_y(x)$,

$$\frac{d^2}{dz^2}H_y(x) + (\frac{\omega^2}{c^2}\varepsilon_j - \beta^2)H_y(x) = 0, \qquad j = 1, 2. \tag{4.7}$$

The solution of Eq. 4.7 is either an exponential function or a sinusoidal function. In order for the solution to be bounded and confined at the interface, the solution must be comprised of two exponentially decaying functions,

$$H_y(x) = \begin{cases} A_1 \exp(-\kappa_1 x), & x > 0 \\ \\ A_2 \exp(\kappa_2 x), & x < 0 \end{cases}, \tag{4.8}$$

Here we introduce the surface plasmon decay constant in the directions perpendicular to the interface, κ_j, with $j = 1, 2$ which are related to the propagation constant β by

$$\kappa_j = \sqrt{\beta^2 - \varepsilon_j \frac{\omega^2}{c^2}} \quad i = 1, 2 \tag{4.9}$$

At the interface, the magnetic field $\mathbf{H}_y$ is continuous for nonmagnetic medium. Similarly the electric field parallel to the interface $\mathbf{E}_x$ is also continuous. Using these boundary conditions, we have $H_y(0^-) = H_y(0^+)$, and $\frac{1}{\varepsilon_2}\frac{dH_y(x)}{dx}|_{x\to 0^-} = \frac{1}{\varepsilon_1}\frac{dH_y(x)}{dx}|_{x\to 0^+}$,. a relationship for κ_j and A_j of both sides can be found as

$$\kappa_2\varepsilon_1 + \kappa_1\varepsilon_2 = 0, \tag{4.10}$$

$$A_1 = A_2.$$

Finally, substituting Eq. 4.9 into 4.10, and rearranging terms, we obtain the familiar dispersion relation for the surface plasmon mode [181],

$$\beta = \frac{\omega}{c}\sqrt{\frac{\varepsilon_1\varepsilon_2}{\varepsilon_1 + \varepsilon_2}}, \tag{4.11}$$

Substituting Eq. 4.11 back into 4.9, we can also derive $\kappa_{1,2}$ as

$$\kappa_1 = \frac{\omega}{c}\sqrt{\frac{-\varepsilon_1^2}{\varepsilon_1 + \varepsilon_2}}$$

$$\kappa_2 = \frac{\omega}{c}\sqrt{\frac{-\varepsilon_2^2}{\varepsilon_1 + \varepsilon_2}} \tag{4.12}$$

A few implication can be immediately observed from Eqs. 4.10 and 4.11:

1. Because the real part of both κ_1 and κ_2 must be positive in order for the mode to remain bounded, the dielectric constants of the two media have to be of opposite sign and satisfy $-\varepsilon_2 > \varepsilon_1$ such that a propagating solution exist. As we see from the dielectric function of free carrier Eq. 2.11, this condition is satisfied if region 2 is a material with high conductivity. In terahertz domain, both metallic materials and highly doped semiconductor could satisfy this constraint.

2. As most metal and highly doped semiconductor have a relatively large negative dielectric constant $\varepsilon_2 \gg \varepsilon_1$, the real part of the propagation constant, β in Eq. 4.11 is typically very close to the refractive index of the dielectric medium 1, $\beta \approx \frac{\omega}{c}\sqrt{\varepsilon_1}$. A trivial example of air/metal interface would give an effective refractive index very close to 1.

3. As the absolute magnitude of the dielectric constant of medium 2 (metallic or highly conductive) is much larger than that of medium 1 (dielectric, typically air), the field is suppressed in medium 2 due to large $\Re(\kappa_2)$, with a typical decay length in medium 2 ($L_{x,2} = 1/2\Re(\kappa_2)$) of the order of nanometers to microns while the decay length ($L_{x,1} = 1/2\Re(\kappa_1)$) in the dielectric is typically of order of millimeters or hundreds of microns at terahertz frequencies.

4.1.1 Solution for TE wave

To derive the expression for TE wave, we use similar procedure but with electric field instead of magnetic field. First we substitute the trial expression for electric field $\mathbf{E} = \exp(\iota\beta z - \iota\omega t)E_y(x)\hat{e}_y$ into Eq. 4.5 and derive a equation for envelope function $E_y(x)$. Then the magnetic field can be calculated with Maxwell Eqs. 4.1-4.4 and by substituting the expression for the electric field together and applying the boundary conditions on the electric field $\mathbf{E}_\parallel$ and magnetic field $\mathbf{H}_\perp$ at the interface, we arrive at

$$
\begin{aligned}
A_1 &= A_2, \\
-\kappa_1 &= \kappa_2,
\end{aligned}
\tag{4.13}
$$

From Eq. 4.13, it is clear that a realistic solution for TE field is impossible, as one of the field component above or below the interface would have to exponentially increase away from the interface, as indicated by the second equation in Eqs. 4.13. In Sec. 4.2, we will find that if a dielectric layer is added to the interface, it is possible to support multiple guiding TE modes as well as multiple guiding TM modes, however as we will show, the TE modes modes would behave quite different from the surface plasmon mode and cutoff frequencies exist for all modes besides TM_0.

4.1.2 Experimental results

An experiment on the coupling of surface plasmon on top of highly doped silicon and gold mirror is conducted. The coupling from a free space terahertz wave to a surface plasmon is not possible without a coupling mechanism to slow the free space wave. Varies coupling methods had been reported with different characteristic. Grating [182] and attenuated total reflection in prism [183] are narrow band but high efficiency coupling methods. Diffraction from edges, either from the corner of prism [184] or from the tip of razor blades [180] are
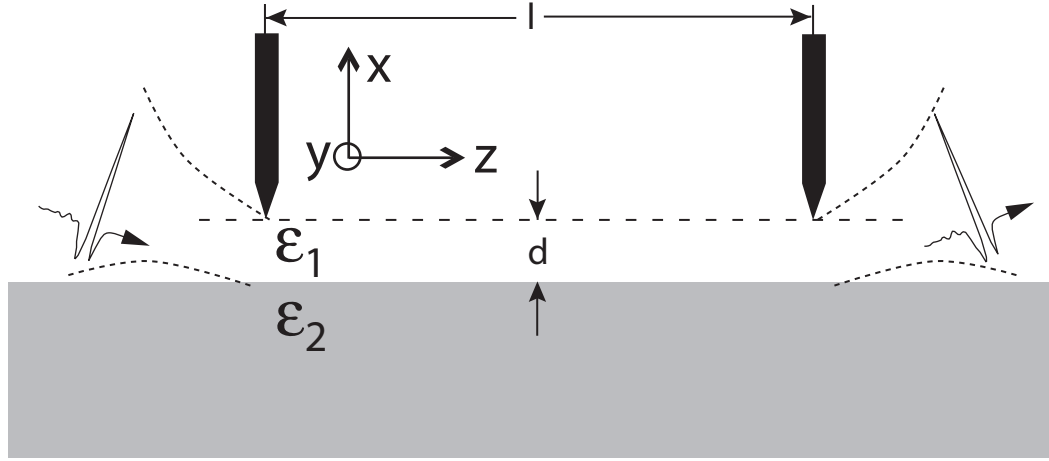
Figure 4.2: Coupling of terahertz wave to surface plasmon with razor blades. The terahertz wave is scattered by the input razor blade located at a distance d away from the surface in order to couple the incident terahertz pulse to surface plasmon propagating on the sample surface. The coupled surface plasmon then travels a distance of l and is then coupled out by another razor blade. In the one interface case shown here, the coupled surface plasmon would have similar spectrum and phase shift as the original terahertz wave as $\beta \approx k_0$ over the whole terahertz spectrum.

used for broadband coupling with low efficient. For this investigation, we adopted the razor blade method described in Refs. [179, 180, 185–187] as the coupling mechanism to slow the free space EM wave. In this scheme, the terahertz wave is focused in free space onto a slit aperture formed by a razor blade (or other scattering object) placed in close proximity to the surface. When the terahertz wave passes through the aperture, it is diffracted into a broad range of angles, allowing a wave with component in propagation direction that matches the speed of the surface plasmon to coupled to the surface as shown in Fig. 4.2.

In Fig. 4.3, we plot the dielectric function of gold from $0.1 - 1000$ THz is calculated from Eq. 2.11 with $\varepsilon_\infty = 1$, $\omega_p = 1.37 \times 10^{16}$ s^{-1} and $\Gamma = 4.05 \times 10^{13}$ s^{-1} from Ref. [188]. Fig. 4.4 shown the associated propagation length $L_z = 1/2\Im(\beta)$ and decay lengths above and below the air/gold surface $L_{x,i} = 1/2\Re(\kappa_i)$ calculated for a surface plasmon mode on gold, using Eqs. 4.11 and 4.12. Similarly, using the dielectric function of highly doped silicon, calculated in Sec. 2.1.2 and shown in Fig. 2.2 , we calculated L_z and $L_{x,i}$ for the surface plasmon mode on highly doped silicon in Fig. 4.5[1].

---

[1] Due to the fact that the carrier density depends on the doping concentration, this particular set of L_z and
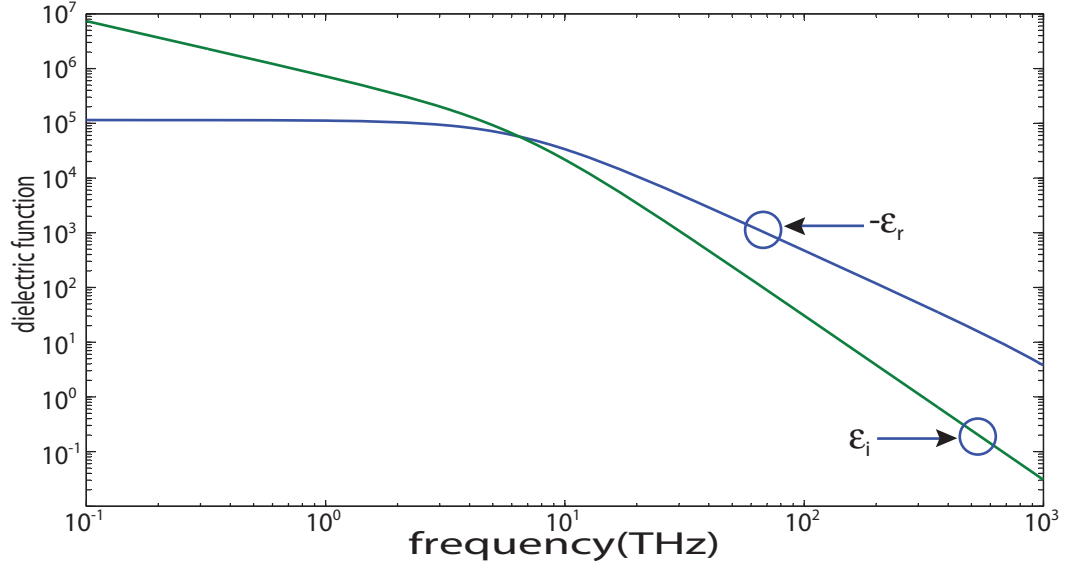
Figure 4.3: Dielectric function of gold calculated with Drude model in Eq. 2.11. From Ref. [188], $\omega_p = 1.37 \times 10^{16}$ s^{-1} , $\Gamma = 4.05 \times 10^{13}$ s^{-1} and $\varepsilon_\infty = 1$.
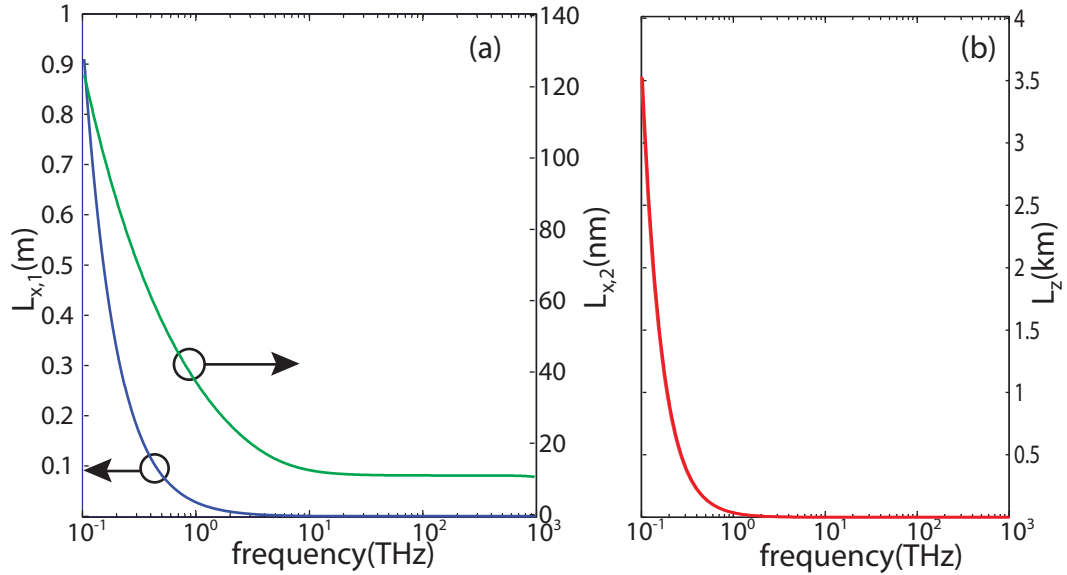
Figure 4.4: Propagation length and $1/e$ penetration depth of surface plasmon mode propagating with frequency of 1 THz on a gold surface using the dielectric function shown in Fig. 4.4. (a) The penetration depth in the direction perpendicular to the sample surface, $L_{x,1} = 26.7$ mm is the penetration depth in air and $L_{x,2} = 36.8$ nm is the penetration depth inside gold (b)The propagation decay length $L_z = 35.1$ m
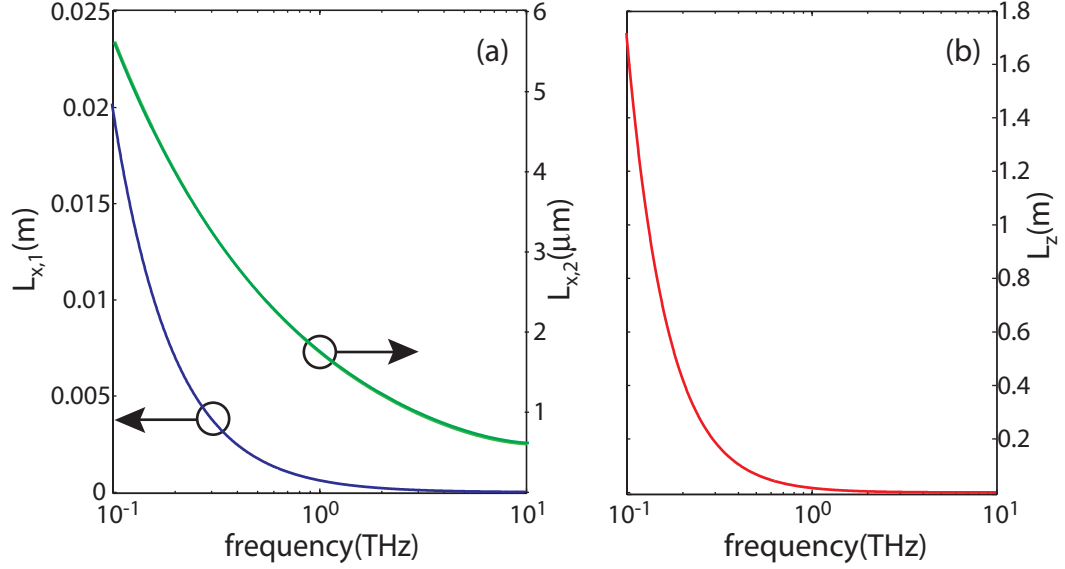
Figure 4.5: Propagation length and $1/e$ penetration depth of surface plasmon propagating with frequency of 1 THz on a silicon surface calculated using dielectric function shown in Fig. 2.11. (a) Penetration depth in direction perpendicular to the sample surface. $L_{x,1} = 0.62$ mm penetration depth in air and $L_{x,2} = 1.74$ μm penetration depth inside silicon.(b) The decay length in propagation direction $L_z = 17.0$ mm

We can immediately see from Fig. 4.4 and Fig. 4.5 that while surface plasmon modes on the highly doped silicon ($L_z = 17.0$ mm) are much lossy then those on gold ($L_z = 35.1$ m), the surface plasmon field is more confined on the silicon surface ($L_{x,1} = 0.62$ mm) than on gold ($L_{x,1} = 26.7$ mm). Such high confinement is useful for applications such as spectroscopy and film characterizing as the high confinement increases the sensitivity of the measurement. The real and imaginary part of β for both gold and silicon are plotted in Figs. 4.6 and 4.7. As the plasma frequencies of both samples are far above the terahertz regime, we see that the real part of β is essentially flat throughtout the terahertz band for both sample. As a result, the dispersion of the terahertz wave can typically be neglected for these modes.

We first seek to find out the optimun coupling gap for our surface plasmon setup. As the field distribution in perpendicular to the sample surface is exponential decayed, the two input and output blades is required to be as close to the surface as possible to increase the

---

$L_{x,i}$ is only valid for p-type doping with with $\rho = 5$ mΩ cm.
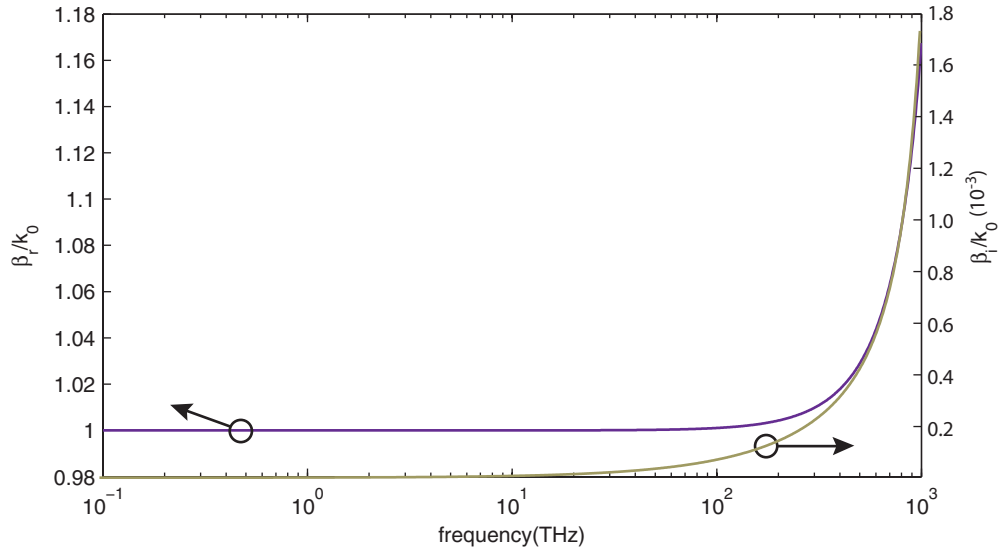
Figure 4.6: Effective refractive index of surface plasmon mode on gold, calculated using Eq. 4.11 and dielectric function curve shown in Fig. 4.3. For low frequencies, the real part of β/k_0 is very close to 1. Propagation of surface plasmon wave in low frequency regime is essentially dispersionless and lossless.

Figure 4.7: Effective refractive index of surface plasmon mode on silicon, calculated using Eq. 4.11 and dielectric function curve shown in Fig. 2.2. At low frequencies, the real part of β/k_0 is very close to 1. As a result, the propagation of silicon surface plasmon wave in low frequency regime is essentially dispersionless in the terahertz spectrum.
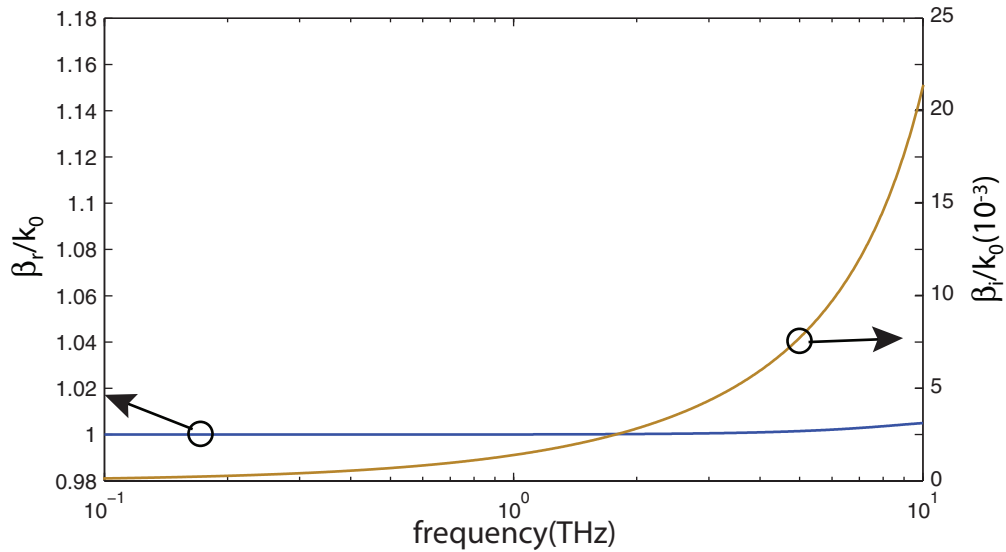
coupling between the diffracted terahertz wave to surface plasmon. On the other hand, the presence of the two blade would block the input terahertz wave, consequencely reducing the amplitude of the terahertz field and hence the optimum coupling point would be determined by these two contradictory effects. In Fig. 4.8, we plot the comparison of time domain measurement traces and the corresponding frequency traces of surface plasmon coupling with different input gap on gold surface. The output gap for this measurement was set to 500 μm and the distance between the two blades was set to be 25.21 mm. The input aperture is varied from 300 μm to a maximum 12.65 mm. On Fig. 4.9 we plot the integrated spectral power from 0.1 THz to 2.5 THz of spectra in Fig. 4.8, which is define as

$$fi(d) = \int_{0.1}^{2.5} |A(f,d)|^2 \, df,$$

where $|A(f,d)|^2$ is the spectral power for a particular frequency f and input gap spacing d. From this data, it is evident that optimal coupling occurs for an input gap of approximately 0.7 mm-0.9 mm. When the input gap is open beyond 1.1 mm (Fig. 4.8), the transmitted THz waveform includes some leakage of the reflected wave, in addition to the surface plasmon mode. Such leakage can be removed by either increase the separation between gaps or by using curved conductive surface with beam block as described in Ref. [189]. As the input gap is further increased, the surface plasmon peak decreases, and shifts slightly forward in delay while the leakage peak increases and stay at the same delay.

A similar experiment on highly doped silicon was also conducted. In this case the separation between the two blades was set to be 24.50 mm. The output aperture was set to 500 μm while the input aperture varied from 300 μm to 12.83 mm. Fig. 4.10 shows the time domain and spectral domain of these traces while Fig. 4.11 shows the corresponding integrated spectral power from 0.1 THz to 2.5 THz. As with the gold case, the optimum coupling gap is found to be in between $0.7 - 0.9$ mm. As with the gold sample, we see evidence that the reflected terahertz wave is leaking through when the input gap opened up above 1.1 mm.
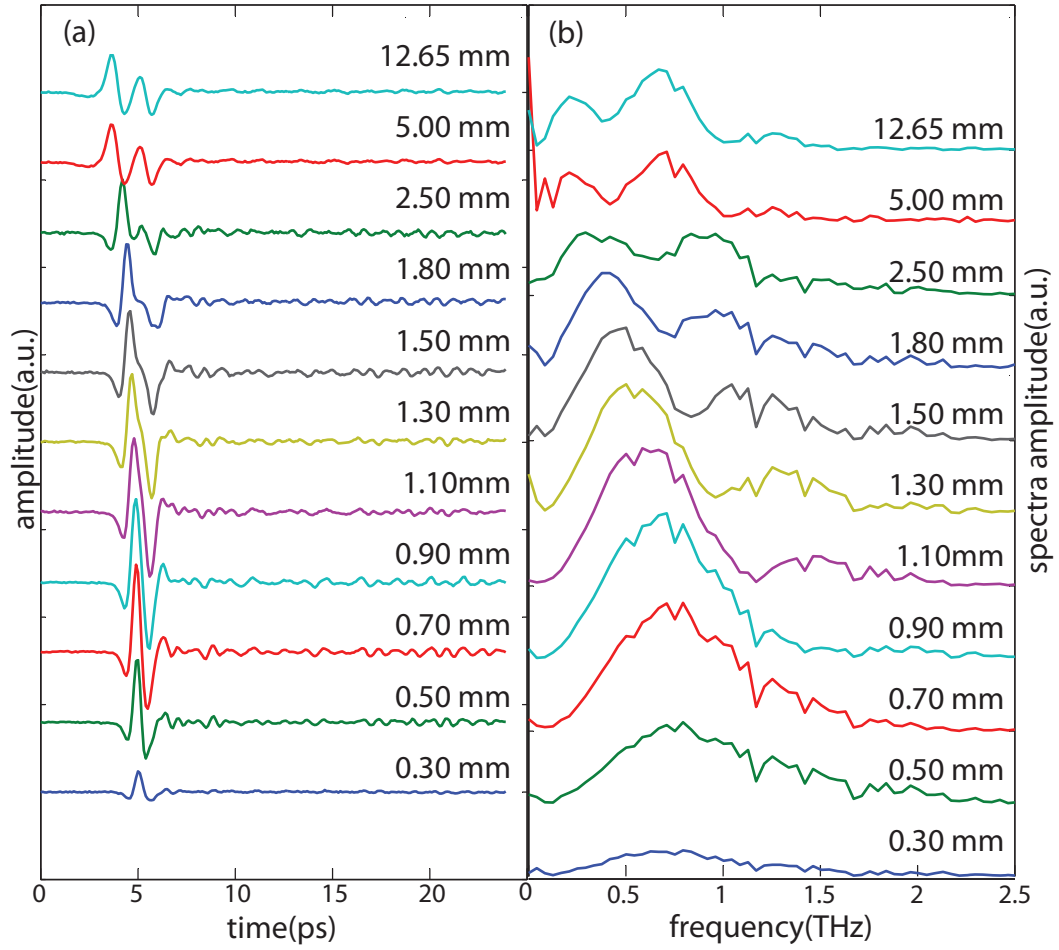
Figure 4.8: Surface plasmon propagation on gold surface. The blades spacing and the output blade gap are set to be 25.21 mm and 500 μm respectively, while the input is varied from 300 μm to 12.65 mm. (a) measured time domain signals for 11 different input gaps. (b) The corresponding frequency domain signals. In both cases, each plot is vertically offset for clarification
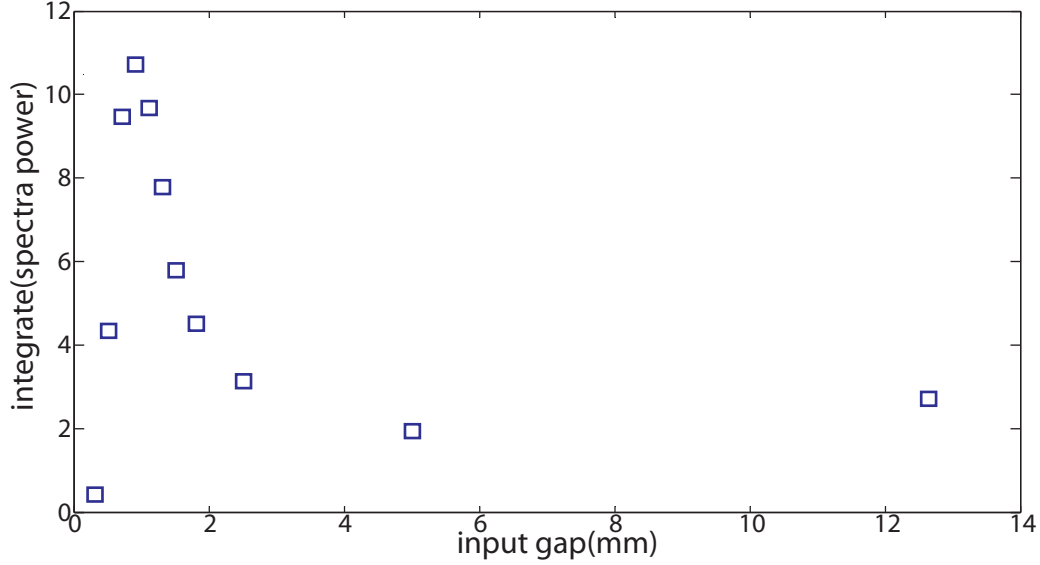
Figure 4.9: The integrated terahertz power of the spectral domain signals from 0.1 THz to 2.5 THz for the frequency domain traces shown in Fig. 4.8(b). A coupling peak is clearly visible in this plot for input coupling apertures between $0.7 - 0.9$ mm.

To ensure that we measured surface plasmon propagation on our sample rather than mere reflection, leakage, or scattering, we compare similar measurements with TE and TM incident polarizations. From the analysis presented earlier, we know that the surface plasmon mode only exists for the case of TM polarization, whereas we expect that diffraction and other leakage effects would presist for both polarization states. For these measurements, we set the blade separation to be 12.3 mm and varied input aperture from ~ 0 mm to 1.3 mm while keeping output blade at 0.5 mm from the surface. In Figs. 4.12 and 4.13, we show both the time domain and the corresponding frequency domain traces comparison. To compare both magnitude and behavior from the TE case to the TM case, we normalized the time domain traces of both TE and TM cases by the peak value of the trace that corresponding to input gap of 1.1 mm for TM polarization and the frequency domain traces by the peak for the frequency trace of 0.7 mm gap for TM polarization. In the TM case, even if the input gap is closed to ~ 0 mm, a signal is still visible, while in the TE case, we see nothing unless the input gap is opened to 1.1 mm, at which point the scattered radiation leaks through the system. We see a similar trend when we plot the cumulative transmitted

85
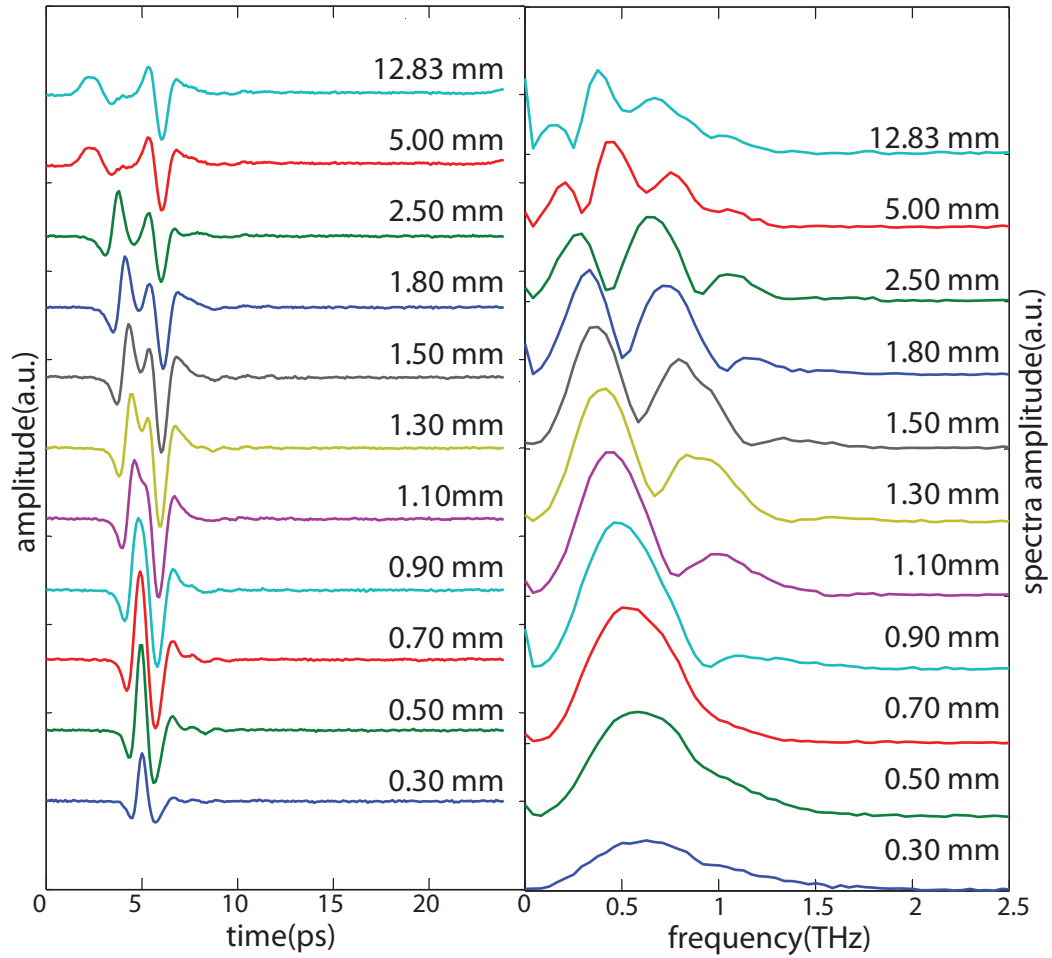
Figure 4.10: Surface plasmon propagation on highly doped silicon. The separation between blades and the output blade gap were kept at 24.50 mm and 0.5 mm respectively while the input gap varied from 0.3 mm to 12.83 mm.
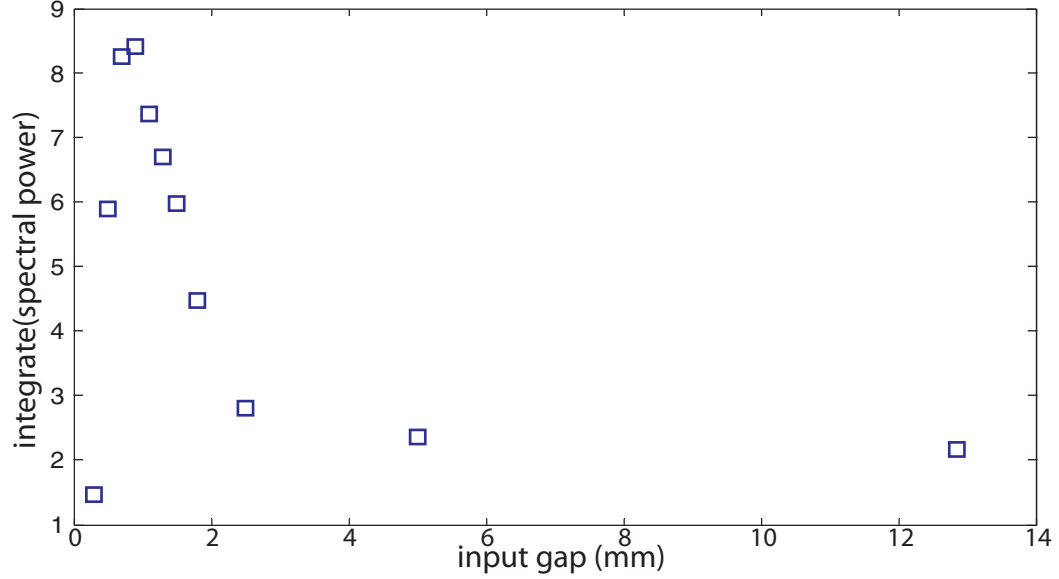
Figure 4.11: Transmitted terahertz power, obtained by intergrating the spectral power from 0.1 to 2.5 THz, for the traces shown in Fig. 4.10.

terahertz power, obtained by integrating the spectra, as shown in Fig. 4.14 .

While the decay length $L_{x,1}$ and $L_{x,2}$ are hard to measure in this configuration. The propagation loss of surface plasmon on highly doped silicon could be measured by changing the separation between the two blades while keeping the input and output gap constant. In this experiment, we fixed the input and output gaps at 0.5 mm and varied separation from 21.5 to 41 mm. In Fig. 4.15 we show the time and frequency domain traces for this measurement. The measured propagation length of 19 mm is of the same order of magnitude as the theoretical value in the terahertz spectrum.

4.2 Surface plasmon propagation on conductive surface with dielectric layer

We consider now the propagation of an electromagnetic wave alone the surface of a conductive surface with thin dielectric film as shown in Fig. 4.17. With the addition of a dielectric film, it is now possible for both TE modes and higher order TM modes to propagate on
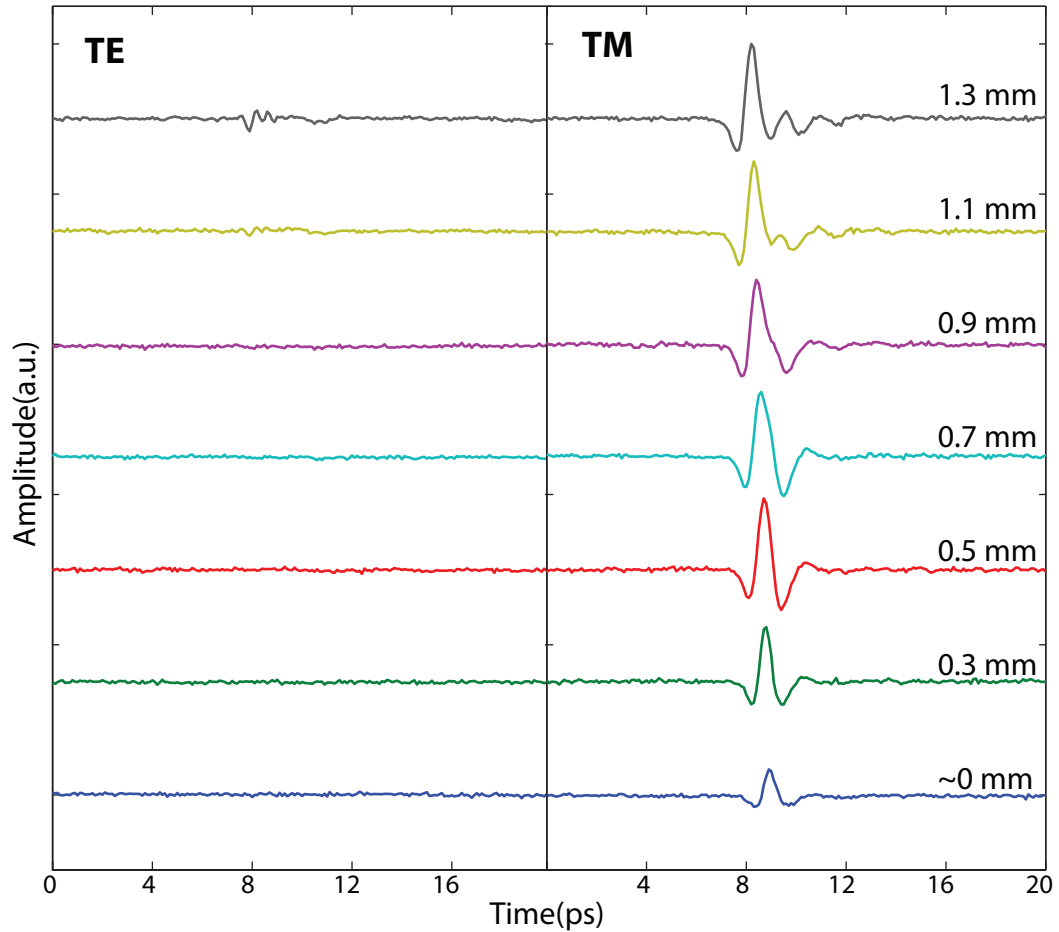
Figure 4.12: Time domain traces comparing the TE and TM incident polarization states. In all cases, the coupling apertures were separated by 12.3 mm from one another, the output aperture was held constant at 0.5 mm, and the input aperture was varied. The TE case shows no appreciable signal until the input gap is opened beyond 1.1 mm while the TM case shows a signal even at input gap of 0 mm, which is explained by coupling to a surface plasmon mode.
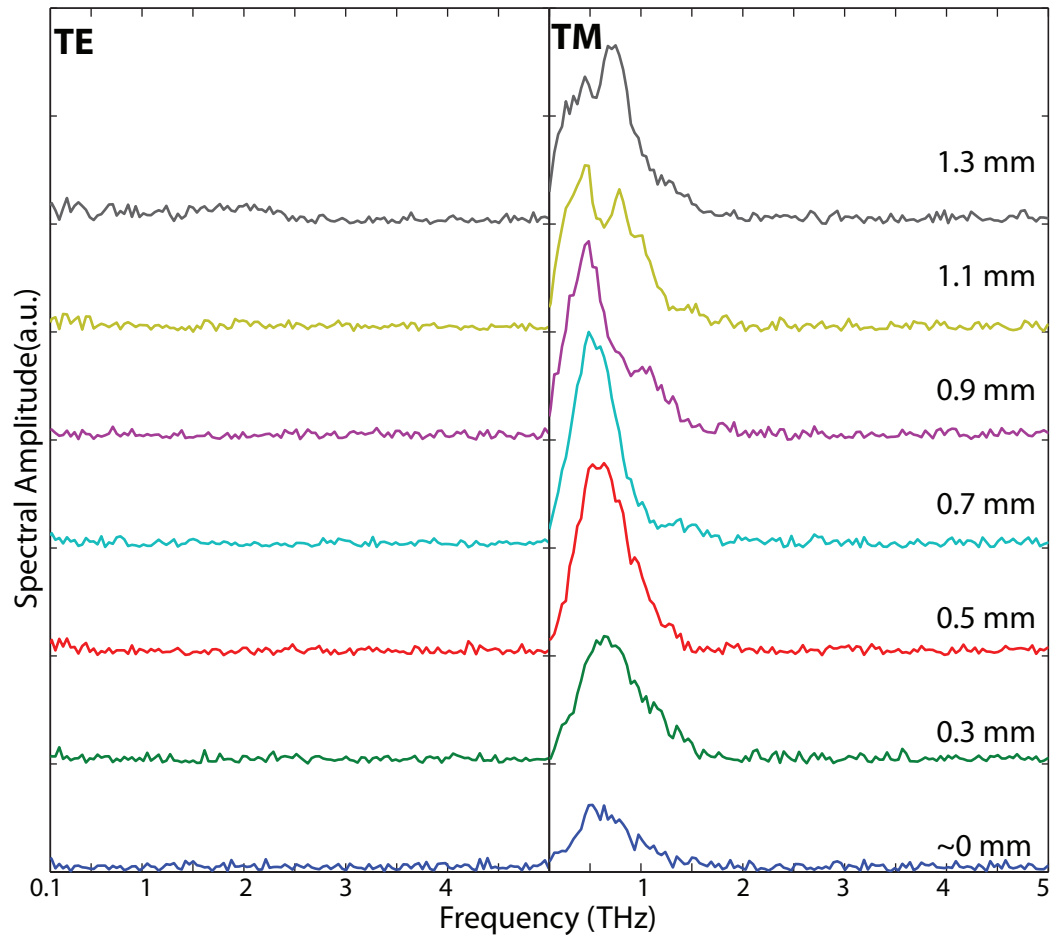
Figure 4.13: Fourier transform of time domain traces in Fig. 4.12.
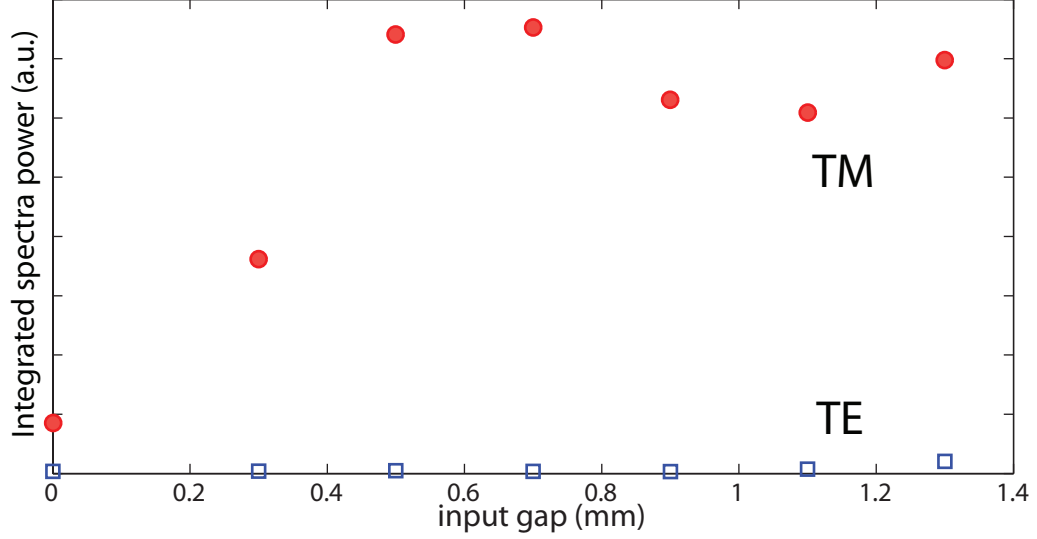
Figure 4.14: Cumulative transmitted THz power, obtained by integrating the spectra shown in Fig. 4.13. The closed circles illustrated the change in spectra power of TM coupled surface plasmon while the opened squares correspond to TE-polarized input. The TM signals continue to increase until it reach the coupling peak of 0.7 mm at which point it begin to saturated and further change above 1.1 mm is due to leakage signals.

the surface as the guiding mode supported by the dielectric, depending on the thickness of the dielectric layer. However, of the many possible modes of propagation, the fundamental TM_0 surface plasmon mode is the only one that does not have a finite cut-off frequency. As a consequence, by appropriately choosing the thickness of the middle dielectric layer, it is possible to construct a single-mode plasmon waveguide. Consider first the case of a TE wave, the general solution to Eq. 4.5 for a propagating mode in medium ε_2 is given by [190],

$$
E_y(x) = \begin{cases} Ae^{-\kappa_1 x}, & x > 0 \\ B\cos \kappa_2 x + C\sin \kappa_2 x, & -d < x < 0 \\ De^{\kappa_3 x}, & x < -d \end{cases} \tag{4.14}
$$

with a multiplication factor of $e^{i(\omega t - \beta z)}$ to take into account of the propagating phase shift and loss. Using boundary conditions for nonmagnetic materials at both interfaces, we have
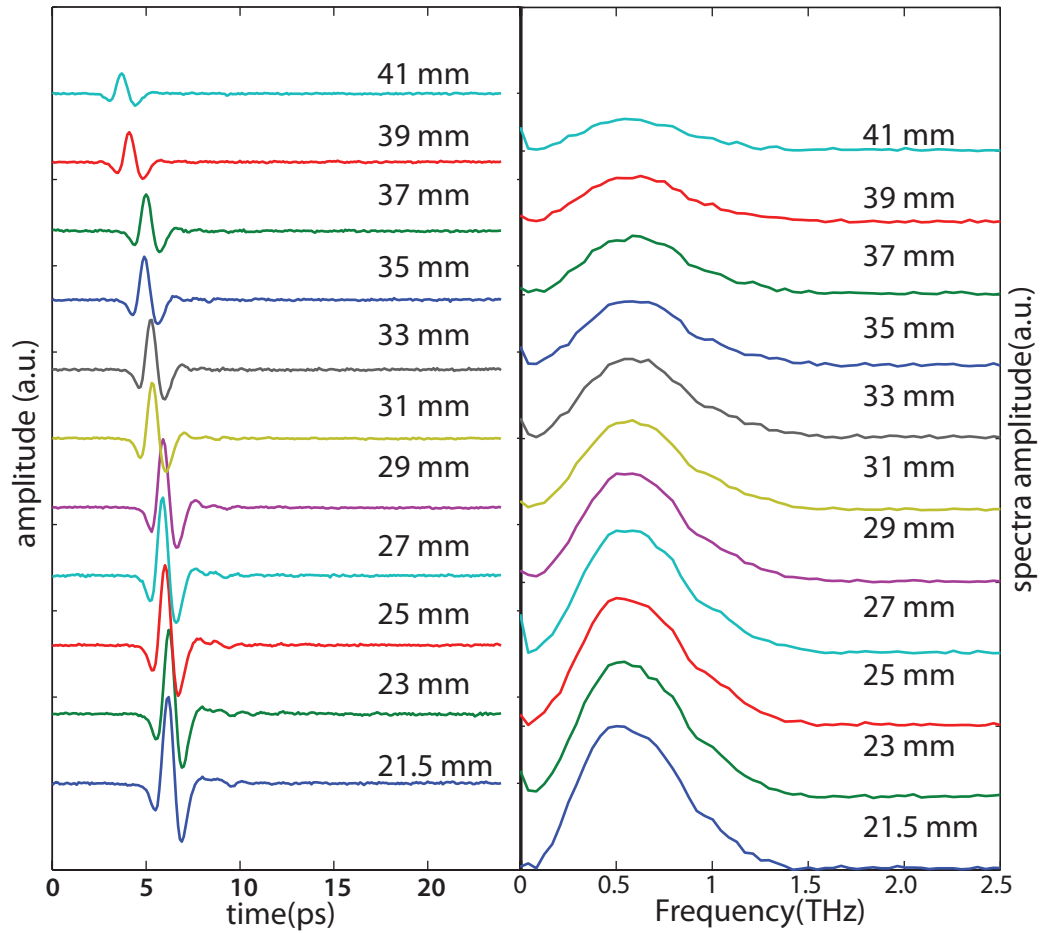
Figure 4.15: Change in surface plasmon transmitted power as the separation between the two razor blades changes from 21.5 to 41 mm. As the surface plasmon propagates for longer distances, the transmitted power falls exponentially due to propagation loss.
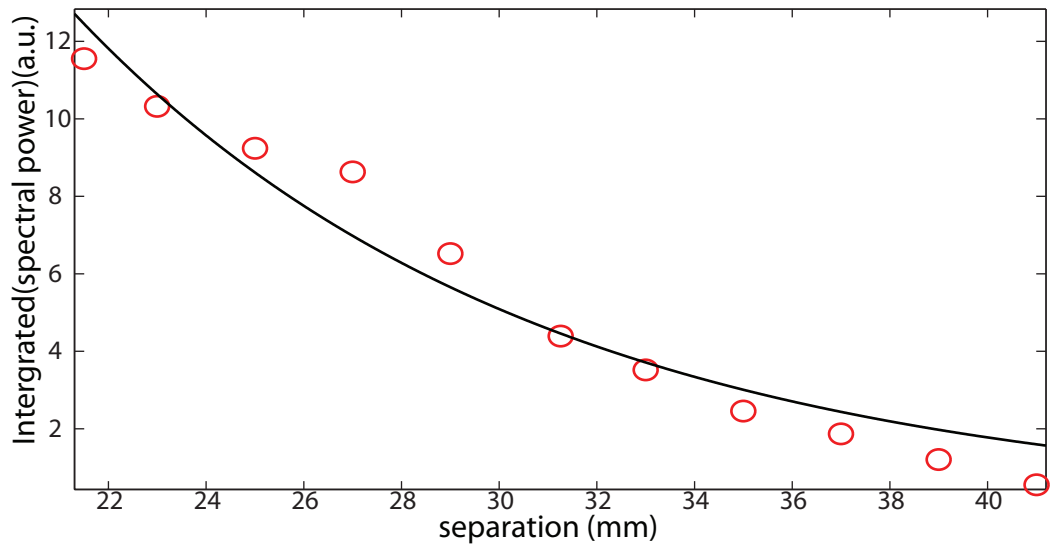
Figure 4.16: Transmitted terahertz power, obtained by integrating the spectral power of the traces plotted in Fig. 4.15 from 0.1 THz-2.5 THz. The black solid line shows an exponential fit. Based on the fitting, the propagation length is estimated as 19 mm
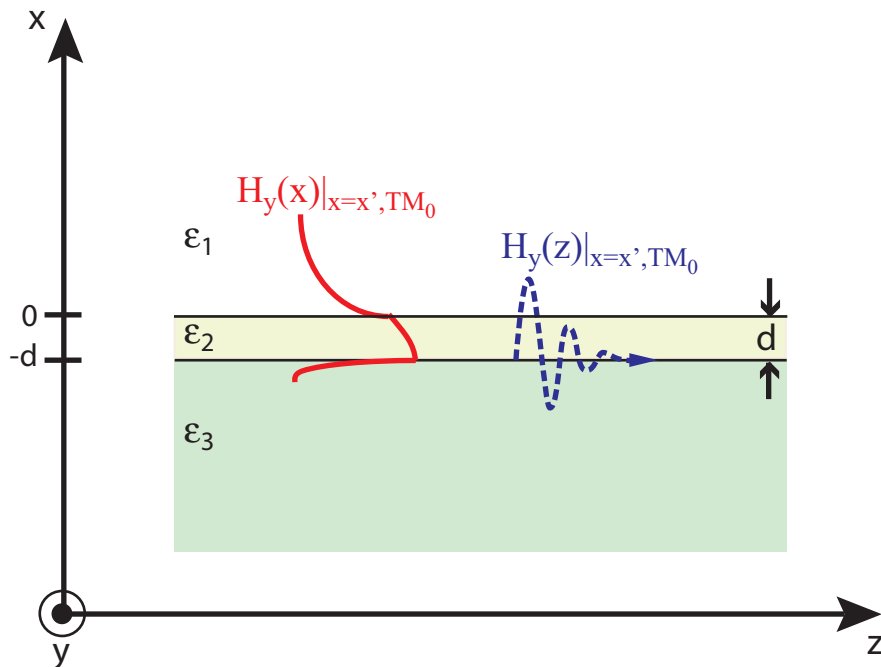
Figure 4.17: Propagation of a surface plasmon wave on the surface of a conductor that is covered with a thin layer of dielectric. The red line illustrates the field distribution of an TM_0 wave (surface plasmon wave) in the direction perpendicular to the interfaces. The blue dotted line shows how the same wave varies along the direction of propagation.

92

$$\left. \begin{array}{l} E_y(0^+) = E_y(0^-) \\ E_y(d^+) = E_y(d^-) \end{array} \right\} E_\parallel,$$

$$\left. \begin{array}{l} H_x(0^+) = H_x(0^-) \\ H_x(d^+) = H_x(d^-) \end{array} \right\} H_\perp,$$

$$\left. \begin{array}{l} H_z(0^+) = H_z(0^-) \\ H_z(d^+) = H_z(d^-) \end{array} \right\} H \parallel,$$

Applying these boundary conditions and the relationship between E_y, H_x and H_z,

$$H_x = - (j/\omega\mu_0)(\partial E_y/\partial z),$$

$$H_z = (j/\omega\mu_0)(\partial E_y/\partial x),$$

we have

$$A = B, \tag{4.15}$$

$$De^{-\kappa_3 d} = B\cos(-\kappa_2 d) + C\sin(-\kappa_2 d), \tag{4.16}$$

$$C = \frac{\kappa_1}{\kappa_2}A, \tag{4.17}$$

$$\kappa_3 De^{-\kappa_3 d} = -\kappa_2 B\sin(-\kappa_2 d) + \kappa_2 C\cos(-\kappa_2 d). \tag{4.18}$$

Hence the solutions of Eq. 4.14 , from Eqs. 4.15-4.17 are

$$E_y(x) = \begin{cases} Ae^{-\kappa_1 x}, & x > 0 \\ A(\cos \kappa_2 x - \frac{\kappa_1}{\kappa_2}\sin \kappa_2 x), & -d < x < 0 \\ A(\cos \kappa_2 d + \frac{\kappa_1}{\kappa_2}\sin \kappa_2 d)e^{\kappa_3(d+x)}. & x < -d \end{cases} \tag{4.19}$$

The three attenuation constants κ_1, κ_2 and κ_3 are related to the propagation constant β by Eq. 4.5 by

$$
\begin{aligned}
\kappa_1 &= \beta^2 - \frac{\varepsilon_1 \omega^2}{c^2} = \beta^2 - \varepsilon_1 k_0^2, \\
\kappa_2 &= \frac{\varepsilon_2 \omega^2}{c^2} - \beta^2 = \varepsilon_2 k_0^2 - \beta^2, \\
\kappa_3 &= \beta^2 - \frac{\varepsilon_3 \omega^2}{c^2} = \beta^2 - \varepsilon_3^2 k_0^2,
\end{aligned}
\tag{4.20}
$$

with $k_0 = \frac{\omega}{c}$. The relationship between $\kappa_1, \kappa_2, \kappa_3$ can be found by substituting Eqs. 4.15-4.17 into Eq. 4.18,

$$
\begin{aligned}
e^{\kappa_3 d}(B\cos \kappa_2 d - C\sin \kappa_2 d) &= e^{\kappa_3 d}\frac{B\kappa_2 \sin \kappa_2 d + C\kappa_2 \cos \kappa_2 d}{\kappa_3} \\
\Rightarrow (B - \frac{\kappa_2}{\kappa_3}C)\cos \kappa_2 d &= (\frac{\kappa_2}{\kappa_3}B + C)\sin \kappa_2 d \\
\Rightarrow \tan \kappa_2 d &= \frac{1 + \frac{\kappa_2}{\kappa_3}\frac{\kappa_1}{\kappa_2}}{\frac{\kappa_2}{\kappa_3} - \frac{\kappa_1}{\kappa_2}} \\
\Rightarrow \tan \kappa_2 d &= \kappa_2 \frac{\kappa_3 + \kappa_1}{\kappa_2^2 - \kappa_1 \kappa_3}.
\end{aligned}
\tag{4.21}
$$

Lastly the normalization factor A is given by $1/\sqrt{P}$, the power flow in the propagating direction with P given by

$$
\begin{aligned}
P &= \frac{1}{2}\Re \int_{-\infty}^{\infty}(\vec{E} \times \vec{H})\cdot \hat{n}dxdy \\
&= \frac{1}{2}\Re \left[\frac{\beta^*}{\omega\mu_0}\int_{-\infty}^{\infty}|E_y|^2 dx.\right]
\end{aligned}
\tag{4.22}
$$

In similar fashion, the magnetic field in the TM case is found to be

$$H_y = \begin{cases} Ae^{-\kappa_1 x}, & x > 0 \\ A(\cos \kappa_2 x - \frac{\kappa_1}{\kappa_2}\frac{\varepsilon_2}{\varepsilon_1}\sin \kappa_2 x), & -d < x < 0 \\ A(\cos \kappa_2 d + \frac{\kappa_1}{\kappa_2}\frac{\varepsilon_2}{\varepsilon_1}\sin \kappa_2 d)e^{\kappa_3(d+x)}. & x < -d \end{cases} \tag{4.23}$$

With the same κ_1, κ_2 and κ_3 relationship with β as Eq. 4.20. The relationship between κ_1, κ_2 and κ_3 is given by

$$\tan \kappa_2 d = \kappa_2 \frac{(\frac{\varepsilon_2}{\varepsilon_1}\kappa_1 + \frac{\varepsilon_2}{\varepsilon_3}\kappa_3)}{\kappa_2^2 - (\frac{\varepsilon_2}{\varepsilon_1}\kappa_1)(\frac{\varepsilon_2}{\varepsilon_3}\kappa_3)}. \tag{4.24}$$

The normalized factor $A = 1/\sqrt{P}$ for TM wave is given by

$$P = \frac{1}{2}\Re(\frac{\beta}{\omega\varepsilon_0}\int_{-\infty}^{\infty}\frac{1}{\varepsilon_j}|H_y|^2 dx)$$

with $j = 1, 2, 3$ the medium associated with the region. The field equations Eqs. 4.19 and 4.23 together with the relationship between the constantsl κ_j, Eqs. 4.21 and 4.24 can be collected in unified forms:

$$E_y, H_y = \begin{cases} Ae^{-\kappa_1 x}, & x > 0 \\ A(cos\kappa_2 x - f\frac{\kappa_1}{\kappa_2}\sin \kappa_2 x), & -d < x < 0 \\ A(\cos \kappa_2 d + f\frac{\kappa_1}{\kappa_2}\sin \kappa_2 d)e^{\kappa_3(d+x)}, & x < -d \end{cases} \tag{4.25}$$

$$\tan \kappa_2 d = \kappa_2 \frac{(f\kappa_1 + g\kappa_3)}{\kappa_2^2 - (f\kappa_1)(g\kappa_3)}, \tag{4.26}$$

and f, g are define as

$$f = \begin{cases} 1, & \text{TE case} \\ \frac{\varepsilon_2}{\varepsilon_1}, & \text{TM case} \end{cases}$$

95

$$
g = \begin{cases} 1 & \text{TE case} \\[2mm] \dfrac{\varepsilon_2}{\varepsilon_3} & \text{TM case} \end{cases}
$$

Eq. 4.26 can also be written as a function of k_0 and $\frac{\beta}{k_0}$ by Eq. 4.20,

$$
\begin{aligned}
\kappa_2 d &= \tan^{-1} \kappa_2 \frac{(f\kappa_1 + g\kappa_3)}{\kappa_2^2 - (f\kappa_1)(g\kappa_3)} + \nu\pi \\[3mm]
\Rightarrow \sqrt{\varepsilon_2 - \left(\frac{\beta}{k_0}\right)^2} \, k_0 d &= \tan^{-1} f \left[\frac{\left(\frac{\beta}{k_0}\right)^2 - \varepsilon_1}{\varepsilon_2 - \left(\frac{\beta}{k_0}\right)^2} \right]^{\frac{1}{2}} + \tan^{-1} g \left[\frac{\left(\frac{\beta}{k_0}\right)^2 - \varepsilon_3}{\varepsilon_2 - \left(\frac{\beta}{k_0}\right)^2} \right]^{\frac{1}{2}} + \nu\pi \\[3mm]
\Rightarrow k_0 d &= \frac{1}{\sqrt{\varepsilon_2 - \left(\frac{\beta}{k_0}\right)^2}} \\[3mm]
&\quad \times \left\{ \tan^{-1} f \left[\frac{\left(\frac{\beta}{k_0}\right)^2 - \varepsilon_1}{\varepsilon_2 - \left(\frac{\beta}{k_0}\right)^2} \right]^{\frac{1}{2}} + \tan^{-1} g \left[\frac{\left(\frac{\beta}{k_0}\right)^2 - \varepsilon_3}{\varepsilon_2 - \left(\frac{\beta}{k_0}\right)^2} \right]^{\frac{1}{2}} + \nu\pi \right\},
\end{aligned}
\tag{4.27}
$$

with $\nu = 0, 1, 2, \cdots$ as the index of different modes.

The implication of Eqs. 4.25 and 4.27 on the propagation of surface plasmon is hard to appreciate without a discussion of the propagation of guided modes in two interfaces dielectric waveguide. Consider the case of a symmetric dielectric waveguide consisting of three layers of dielectric with real and positive ε_j and $\varepsilon_2 > \varepsilon_1 = \varepsilon_3$. If we replace d by $d = 2d'$ in Eq. 4.26, then we find

$$
\begin{aligned}
\tan 2\kappa_2 d' &= \frac{2 \tan \kappa_2 d'}{1 - \tan^2 \kappa_2 d'} \\[3mm]
&= \frac{2 \frac{\kappa_1}{\kappa_2}}{1 - \frac{\kappa_1^2}{\kappa_2^2}}.
\end{aligned}
$$

96

After using trigonometric identity of $\tan 2\theta = \frac{2\tan\theta}{1-\tan^2\theta}$ and solve for the expression of $\kappa_1 d'$,

$$\kappa_2 d' \tan \kappa_2 d' = \kappa_1 d'$$

$$-\kappa_2 d' \cot \kappa_2 d' = \kappa_1 d'.$$

Which are the familiar expressions for symmetric waveguide in Ref. [191]

Consider now the case of the asymmetric real dielectric waveguide with $\varepsilon_1, \varepsilon_2, \varepsilon_3 \in \Re$ and $\varepsilon_2 > \varepsilon_3 > \varepsilon_1$. In this case the trend of $\frac{\beta}{k_0}$ for all modes would be bounded by $\varepsilon_2 \geq \frac{\beta}{k_0} \geq \varepsilon_3$ with the minimum cutoff value at $\frac{\beta}{k_0} = \varepsilon_3$,

$$(k_0 d)_{cutoff} = \frac{1}{\sqrt{\varepsilon_2 - \varepsilon_1}} \left\{ \tan^{-1} g \sqrt{\frac{\varepsilon_1 - \varepsilon_3}{\varepsilon_2 - \varepsilon_1}} + v\pi \right\}. \tag{4.28}$$

In Fig. 4.18, we plot the calculated relationbetween β and ω, for a real asymmetric waveguide of $\varepsilon_1 = 1$, $\varepsilon_2 = 2^2$ and $\varepsilon_3 = 1.5^2$. These curves were obtained by numerically solving Eq. 4.20. As $k_0 d \rightarrow \infty$, the effective refractive index $\beta/k_0 \rightarrow \sqrt{\varepsilon_2}$. On the other end, as the normalized frequency $k_0 d$ decreases, the trend for $\beta/k_0 \rightarrow \sqrt{\varepsilon_3}$ and eventually becomes cut off when the condition in Eq. 4.28 is reached. Between the TM modes and the TE modes with same v, the trends are very similar with TE mode slightly smaller for the same $k_0 d$ as $f = \frac{\varepsilon_2}{\varepsilon_1} > 1$ and $g = \frac{\varepsilon_2}{\varepsilon_3} > 1$. Fig. 4.19 shows the normalized field distribution for TE$_0$, TE$_1$, TM$_0$ and TM$_1$ for $k_0 d = 10$. In the case of real asymmetric waveguides, all modes are concentrated in the middle of medium 2. In all cases, mode overlap with medium 1 and 3 increases when $\sqrt{\varepsilon_3} \rightarrow \sqrt{\varepsilon_2}$ and $\sqrt{\varepsilon_1} \rightarrow \sqrt{\varepsilon_2}$ or when $k_0 d \rightarrow 0$.

On the other hand, if ε_3 is negative and $\varepsilon_1 < \varepsilon_2 < |\varepsilon_3|$, then all modes other then TM$_0$ are bounded by $\varepsilon_1 < \frac{\beta}{k_0} < \varepsilon_2$. The TM$_0$ mode, however behaves differently. At low frequency, as g is negative, there is a chance for the two $\tan^{-1}$ terms in Eq. 4.27 to cancel one another such that when $k_0 d \rightarrow 0$, a nonzero solution exists for $\frac{\beta}{k_0}$. From a physical point of view,
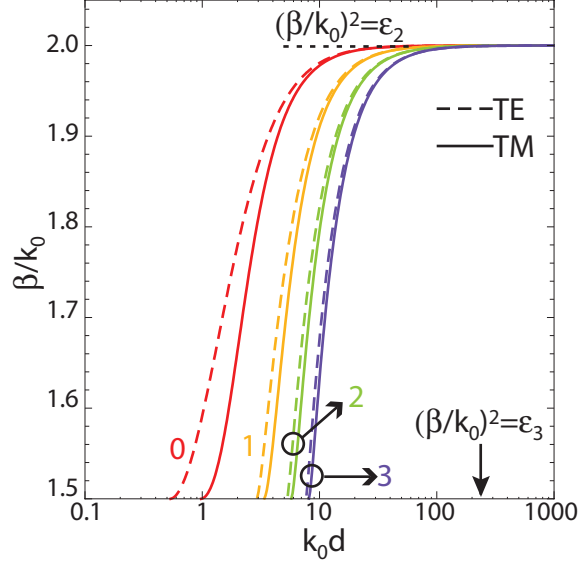
Figure 4.18: Effective refractive index, β/k_0 versus normalized frequency $k_0 d$ for $\varepsilon_1 = 1$, $\varepsilon_2 = 2^2$ and $\varepsilon_3 = 1.5^2$. The effective refractive indices for all mode are constrained by $\varepsilon_3 < \frac{\beta}{k_0} < \varepsilon_2$

as $k_0 d \to 0$, the field should behaves just as a single interface surface plasmon propagation in between the medium ε_1 and medium ε_3. Hence at very low $k_0 d$, Eq. 4.27 should have the same form as Eq. 4.11. Similarly at very high $k_0 d \to \infty$, the TM_0 field should behaves similar to a single interface surface plasmon propagation in between medium ε_2 and ε_3 and again Eq. 4.27 should approach Eq. 4.11. In mathematical form,

$$
\frac{\beta}{k_0} \to
\begin{cases}
\sqrt{\frac{\varepsilon_1 \cdot \varepsilon_3}{\varepsilon_1 + \varepsilon_3}}, & k_0 d \to 0 \\
\sqrt{\frac{\varepsilon_2 \cdot \varepsilon_3}{\varepsilon_2 + \varepsilon_3}}, & k_0 d \to \infty
\end{cases}.
\tag{4.29}
$$

A plot of effective dielectric function is plot for the case of $\varepsilon_1 = 1$, $\varepsilon_2 = 2^2$ and $\varepsilon_3 = -4^2$ is shown in Fig. 4.20.

Fig. 4.21 plots the corresponding field distributions for the first few modes of the three-layer plasmon waveguide. While all other modes are concentrated in the middle of the medium 2, the TM_0 mode is concentrated in the interface between medium 3 and medium 2 and falls exponentially away from this interface. Again we see that the TM_0 mode behaves more similarly to the single interface surface plasmon case discussed in Sec. 4.1.

98
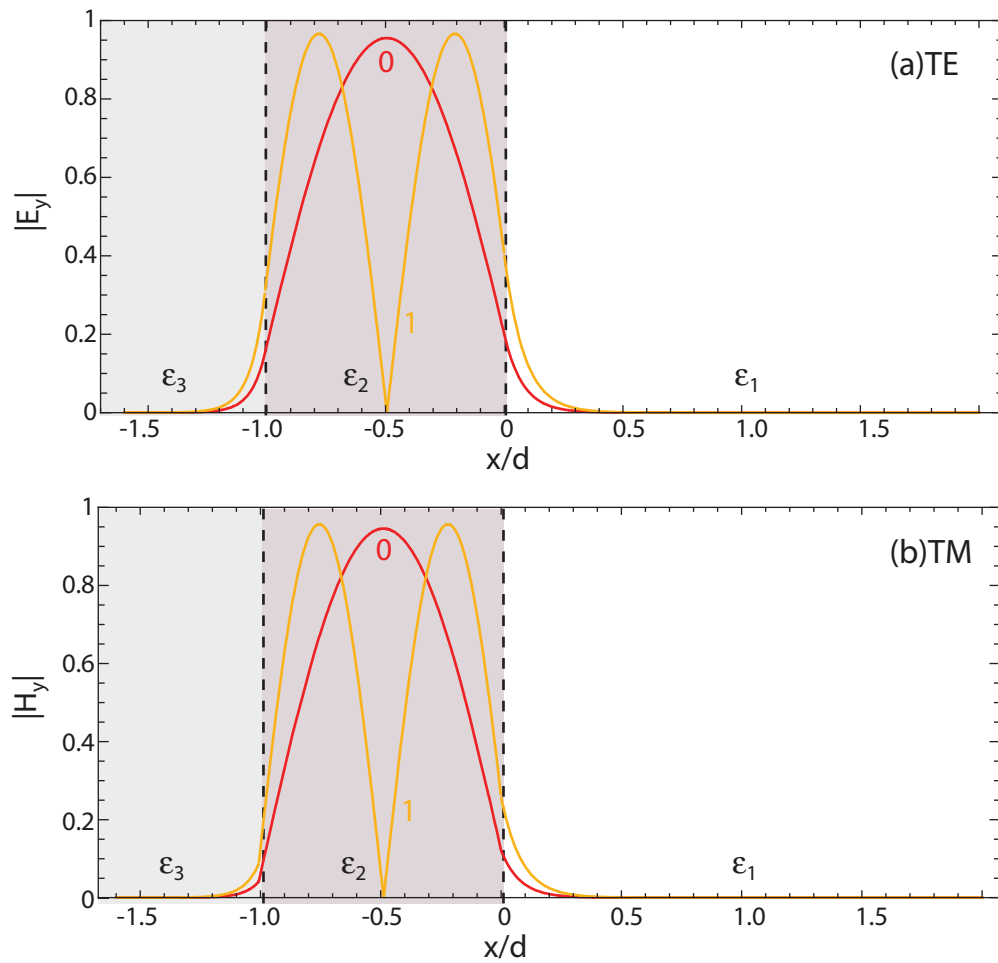
Figure 4.19: Normalized fields amplitudes for asymmetric waveguide $k_0 d = 0$ with $\varepsilon_1 = 1$, $\varepsilon_2 = 2^2$ and $\varepsilon_3 = 1.5^2$. (a) E fields of TE_0 and TE_1.(b) H fields of TM_0 and TM_1
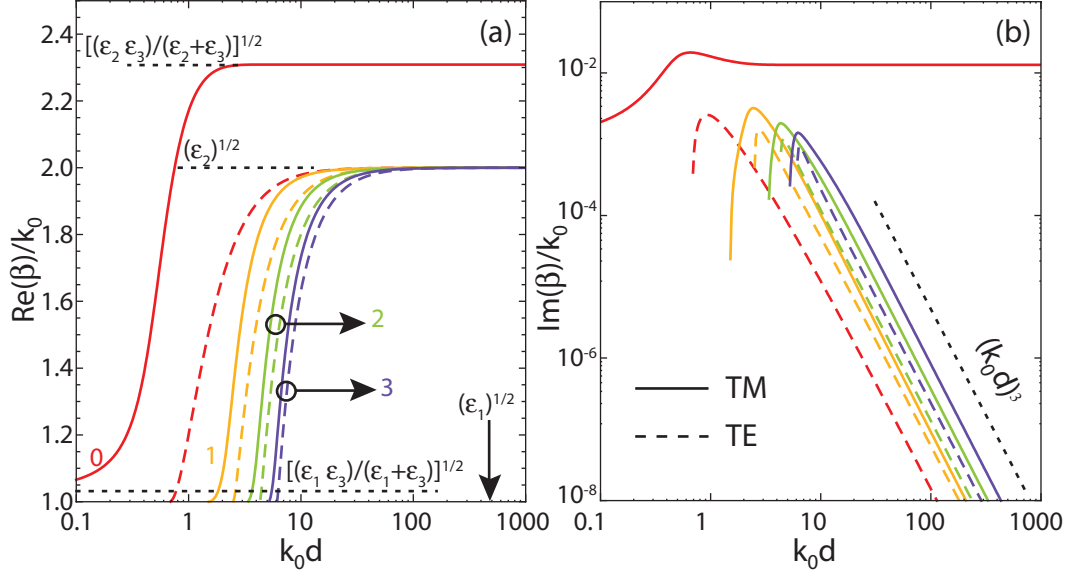
Figure 4.20: Effective refractive index β/k_0 versus normalized frequency $k_0 d$. (a) Real part. The TM_0 mode is bounded by $\sqrt{\frac{\varepsilon_1 \cdot \varepsilon_3}{\varepsilon_1 + \varepsilon_3}} \leq \frac{\beta}{k_0} \leq \sqrt{\frac{\varepsilon_2 \cdot \varepsilon_3}{\varepsilon_2 + \varepsilon_3}}$ and is not cut off over the entire $k_0 d$. For all other modes, the propagation constant is bounded by $\sqrt{\varepsilon_1} \leq \frac{\beta}{k_0} \leq \sqrt{\varepsilon_2}$ and have a cutoff point where $\frac{\beta}{k_0} = \sqrt{\varepsilon_1}$. (b) Imaginary part. The loss for TM_0 mode is constant when $k_0 d \to \infty$ while all other modes followed a $(k_0 d)^{-3}$ trend.

4.2.1 Experimental results

Three samples of porous silicon film on silicon wafer are fabricated for this experiment with applied current density of 90 mA/cm^2 using the same procedure described in in Sec. 3.2. The thickness of each samples were measured by SEM to be 10.6 μm, 28.3 μm and 56.4 μm and are shown in Fig. 4.22. The experimental setup is identical to that shown in Fig. 4.1 except for the change in sample. As we will see later, unlike the single interface case of silicon or gold sample, the surface plasmon mode for the three-layer waveguide exhibits significantly more dispersion and frequency dependent loss than in the single-interface case. This leads to significant pulse broadening, as depicted in Fig. 4.23

Using a separately-fabricated free standing porous silicon sample with similar applied etching current, we independently determined the refractive index of the porous silicon layer to be $n = 1.67$. Using this value, we numerically calculated the dispersion of the surface plasmon mode, which is plotted in Fig. 4.24, we plot the behavior of the TM_0
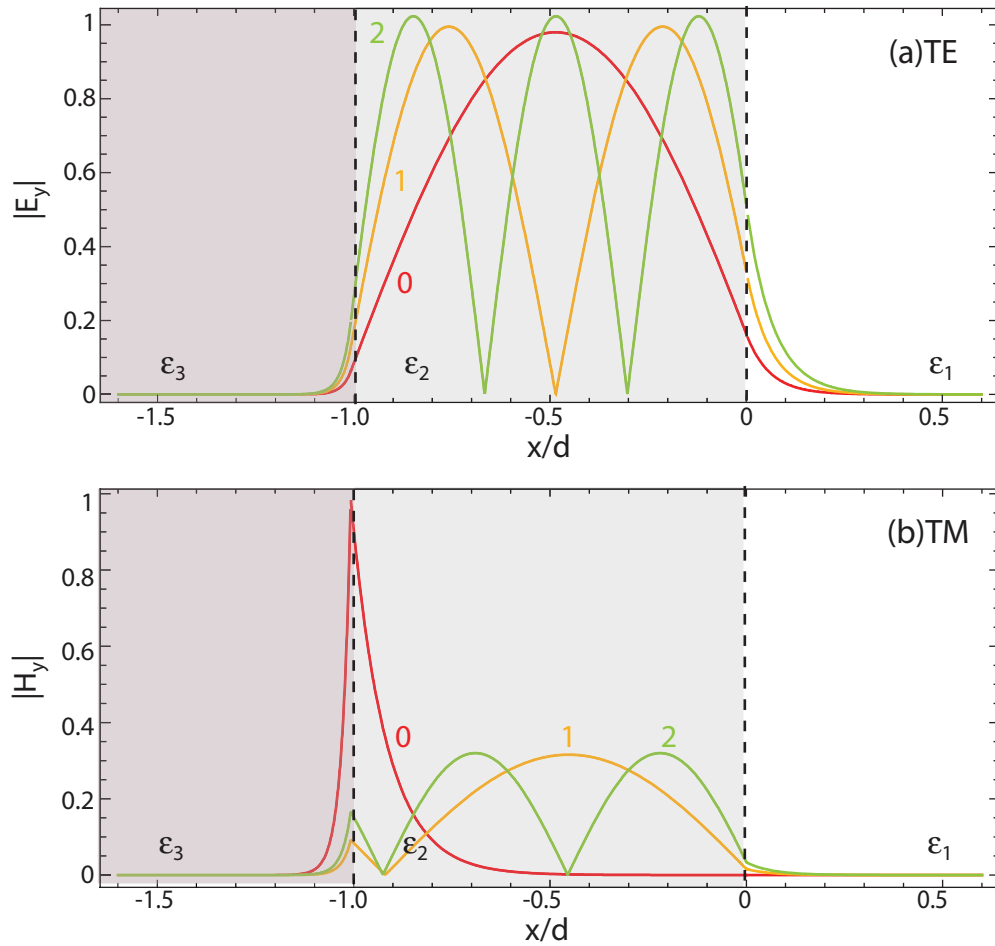
Figure 4.21: Calculated field distribution for the first few TE and TM modes with $\varepsilon_1 = 1, \varepsilon_2 = 2^2$ and $\varepsilon_3 = -4^2$ and $k_0 d = 10$. (a) TE modes 0,1,2. (b)TM modes 0,1,2
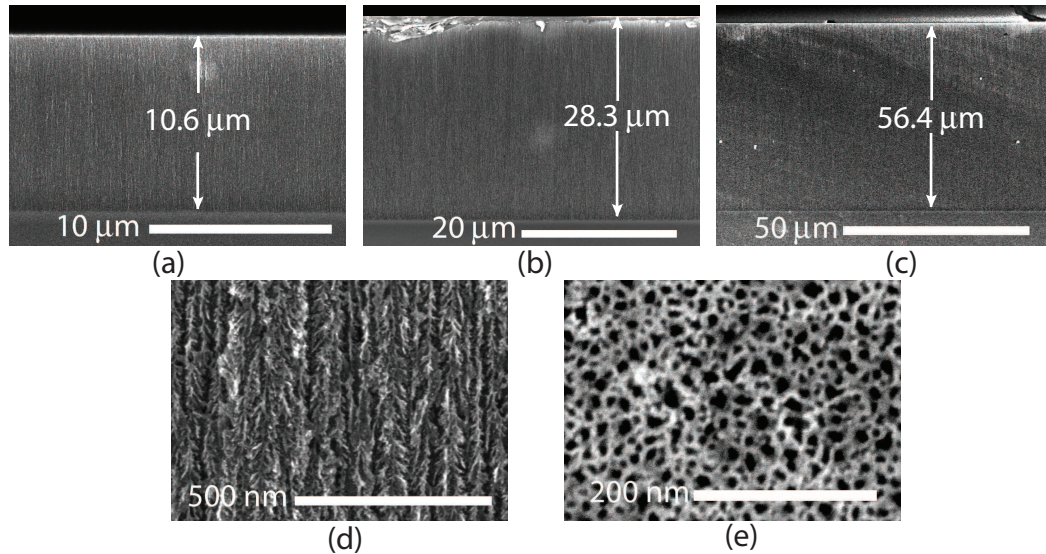
Figure 4.22: SEM pictures of three porous silicon samples used in surface plasmon propagation measurements. (a) 10.6 μm sample (b) 28.3 μm sample (c)56.4 μm sample.(d) Zoom in view of the 28.3 μm sample. (e) top down view of a typical porous silicon sample. All samples are fabricated with current densities of 90 mA/cm^2 and were determined to have an effective refractive index of 1.67.
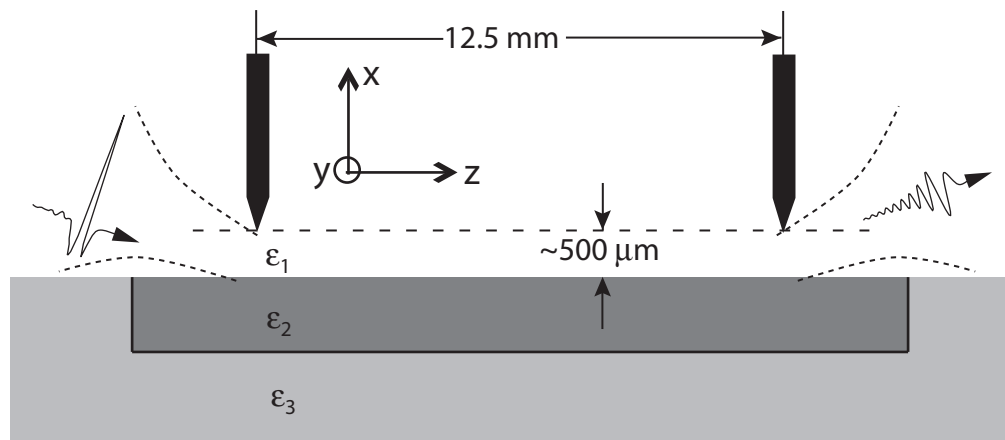
Figure 4.23: Experimental system used to couple terahertz pulses into and out of a porous silicon surface plasmon waveguide.
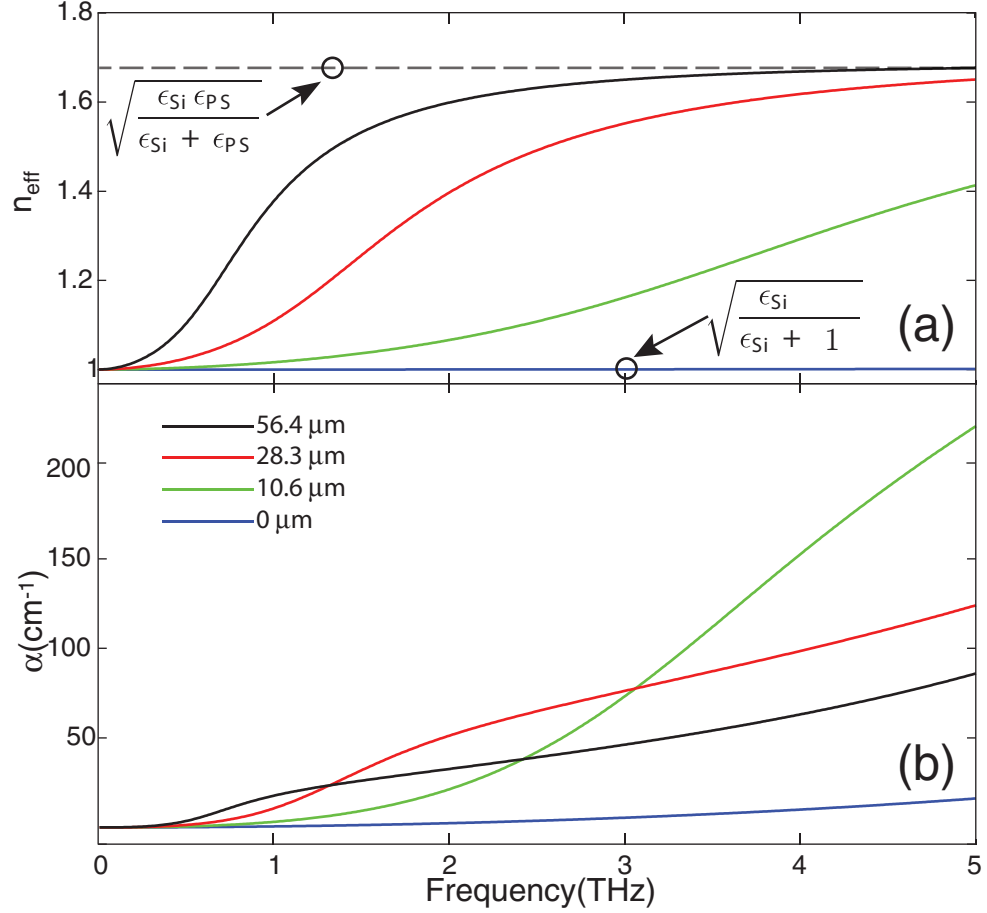
Figure 4.24: Effective refractive index and absorption of surface plasmon in porous silicon samples of thickness 0 μm,(blue solid line),10.6 μm (green solid line),28.3 μm(red solid line) and 56.4 μm (black solid line). The effective refractive indices are bounded by effective reflective indices of surface plasmon propagation in porous silicon/silicon (gray dashed line) and air/silicon (blue solid line) interface.

mode for these three samples. The cutoff frequencies $k_0 d$ for TE$_0$ and TM$_1$ modes is calculated to be $k_0 d = 1.05$ and 2.09 for our samples. Therefore, in the 56.4 μm sample, it is possible to excite the TE$_0$ mode at frequency above 0.89 THz and the TM$_1$ mode at frequencies above 1.76 THz. Similarly, it is possible to excite a TE$_0$ mode for frequencies higher then 1.76 THz for the 28.3 μm. In our measurement, however, we see no clear evidence of these modes. This is likely caused by the to the vastly different mode profile for these guided modes that prevent coupling to occured. Hence in our simulation, we did not include higher order modes when simulating the propagation.

In Fig. 4.25-4.28, we plot the calculated transvere magnetic field of the surface plas-

Figure 4.25: Normalized field distribution for sample with porous silicon thickness of $0\,\mu$m, $10.6\,\mu$m, $28.3\,\mu$m and $56.4\,\mu$m at 0.5 THz.

mon mode for porous layer thicknesses of 0, 10.6, 28.3 and 56.4 μm. These modes were calculated at a frequencies of 0.5, 1.0, 2.0, and 4.0 THz, and all are normalized to have the same optical power. In all cases, the surface plasmon mode reaches its maximum value at the interface between the substrate and the porous silicon layer. The propagation loss of the mode is strongly related to the mode intensity at the lossy silicon surface, which depends on the film thickness.

For all samples measured, we set both the input and output apertures to be 0.5 mm from the porous silicon surface. The separation between the coupling apertures was set to be $l = 12.5$ mm, which defines the propagation distance. Using the value of β, shown in Fig. 4.24, we calculated the group delay $\tau = \left(\frac{\partial \beta}{\partial \omega}\right)^{-1} l$ and the normalized spectral transmission $A = \left|e^{-i\beta l}\right|$, for the three samples, as shown in Fig. 4.29. We see from Fig. 4.29 that in all cases, the 12.5 mm surface plasmon waveguide acts as a low-pass filter that attenuates higher frequencies. The calculated bandwidth decreases as the porous layer is made thicker. For our samples, we calculate the $1/e$ bandwidth to be 1.66 THz for silicon without porous silicon layer, 0.77 THz for the 10.6 μm sample, 0.525 THz for 28.3 μm sample and 0.385 THz for the 56.4 μm sample. Over the frequency span from $0-0.5$ THz,
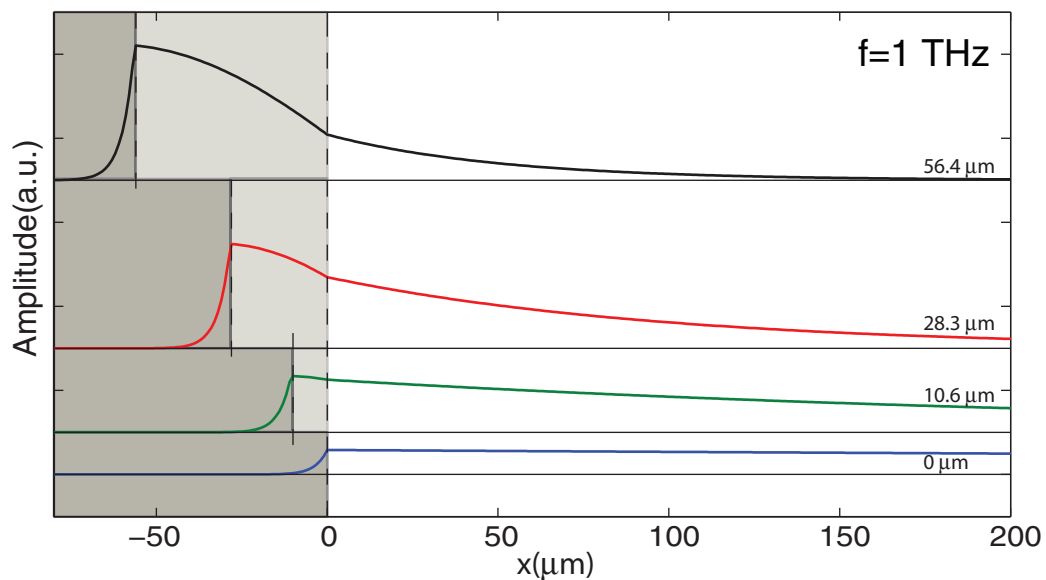
Figure 4.26: Normalized field distribution for sample with porous silicon thickness of 0 μm, 10.6 μm, 28.3 μm and 56.4 μm at 1 THz.

Figure 4.27: Normalized field distribution for sample with porous silicon thickness of 0 μm, 10.6 μm, 28.3 μm and 56.4 μm at 2 THz.
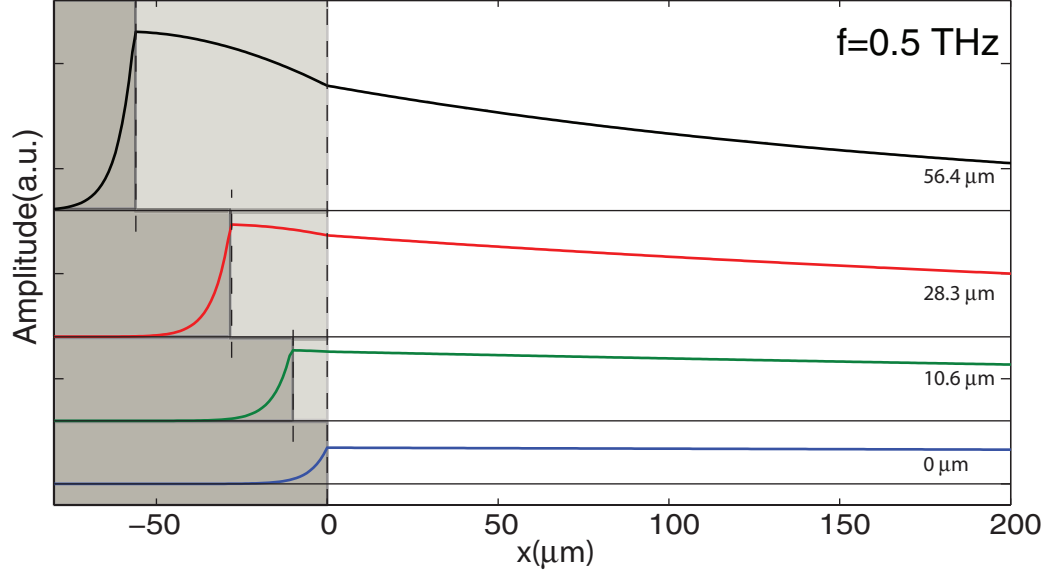
Figure 4.28: Normalized field distribution for sample with porous silicon thickness of 0 μm, 10.6 μm, 28.3 μm and 56.4 μm at 4 THz.

the silicon without porous silicon layer($d = 0$) does not show any significant variation in group delay while the group delay for the 10.6 μm, 28.3 μm and 56.4 μm samples are 0.53 ps, 3.18 ps and 13.88 ps respectively.

In Fig. 4.30, we show the comparison between the measured and calculated pulses in the time domain. The experimental traces were measured using experimental setup depicted in Fig. 4.23. When calculating the theoretical response, we obtained a reference time-domain trace by realigning the optics to bypass the waveguide entirely, giving an unobstructed transmitted waveform. We then fed this measured input signal into the calculated dispersion relation shown in Fig. 4.24 and numerically computed the expected time-domain traces after a propagation distance of 12.5 mm. For comparison, the calculated signals were normalized such that their peak amplitudes are the same as the peak amplitude of the corresponding measurements. Although the theoretical calculation does not take into account any spatial effects such as frequency-dependent coupling, the prediction of the theoretical calculation is surprisingly good especially for the thicker samples. The propagation of surface plasmon in the sample without the porous silicon is essentially dispersionless as predicted from our calculation in Fig. 4.29. On the other hand, we see
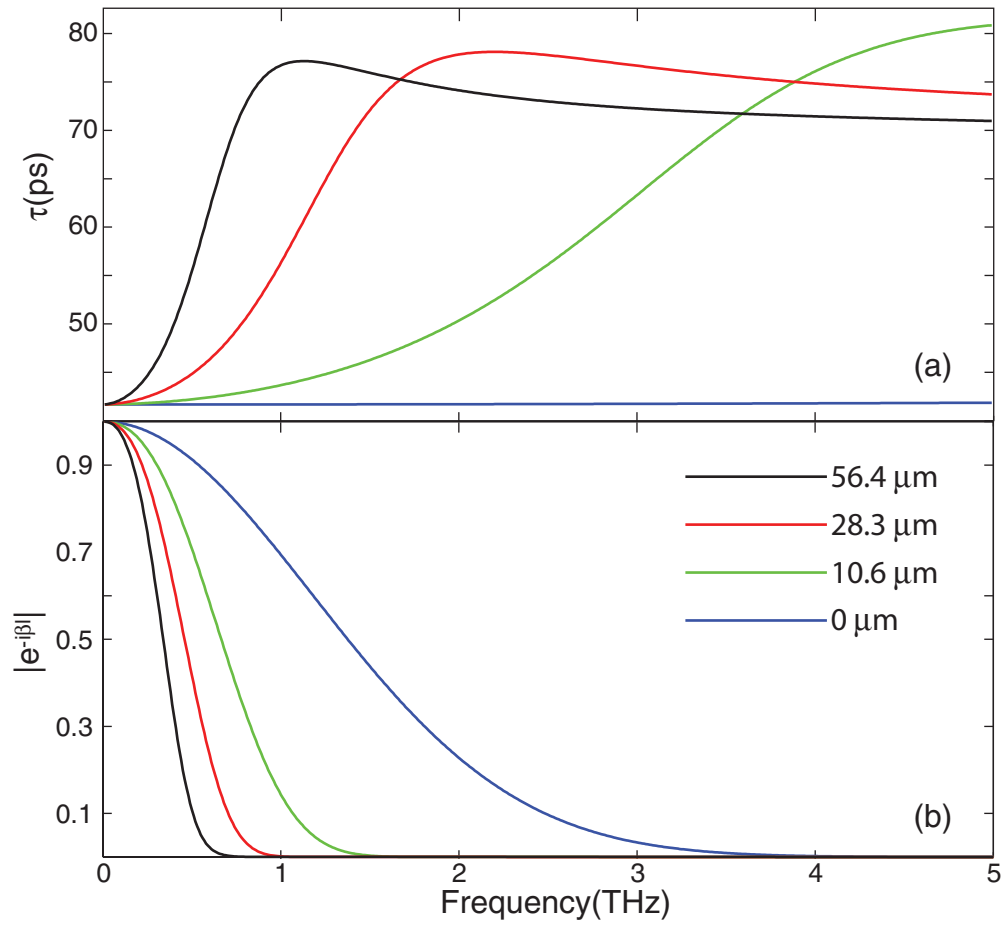
Figure 4.29: Calculated dispersed time and signal amplitude attenuation for samples with porous silicon film of thickness 0 μm, 10.6 μm, 28.3 μm and 56.4 μm over a propagation length of 12.5 mm(a) delayed time. (b) signal amplitude attenuation.

that as the porous silicon thickness increased for samples with porous silicon film, the high frequency component is attenuated with high dispersion in the time domain traces and also in the corresponding frequency domain plot of the signals shown in Fig. 4.31.

As obvious from the matching of the terahertz spectrum from the measured pulses in Fig. 4.31 and the prediction from Fig. 4.29(b), the spreading and attenuation of the measured signals is most likely due to the quick increase in attenuation that is explained by field confinement in Figs. 4.25-4.28.

4.3 Conclusion

In conclusion, we describe the fabrication and measurement of a new type of terahertz surface plasmon waveguide in which the terahertz mode is guided in a nanoporous silicon layer. We present calculations and measurements of the time-domain response that show the role of modal dispersion and frequency-dependent loss in the propagation. At terahertz frequencies, nanoporous layer behaves like an effective dielectric material, with the important difference that its entire volume could potentially be permeated by liquids or gases from the surrounding environment. Because of the large internal surface area inherent to porous materials, this structure holds promise for sensor and spectroscopy applications that rely on selective surface binding.
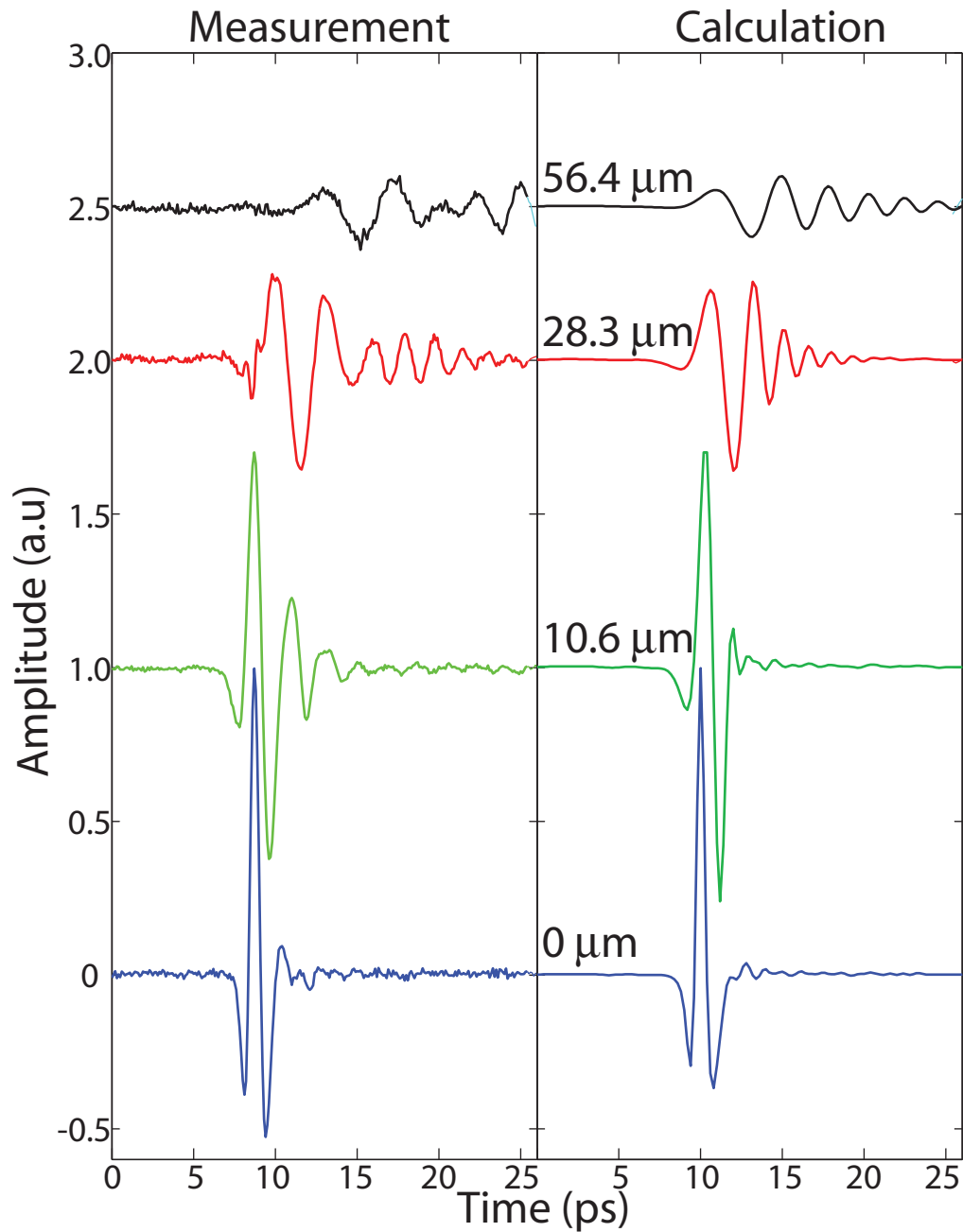
Figure 4.30: Time domain comparison between measured and calculated terahertz signal. The calculation is done by using an transmitted terahertz signal obtained without the sample, and calculating the response of the surface plasmon with propagation length of 12.5 mm. Each trace was normalizated such that the peak amplitude of the calculation is the same as the peak amplitude of the measurement.
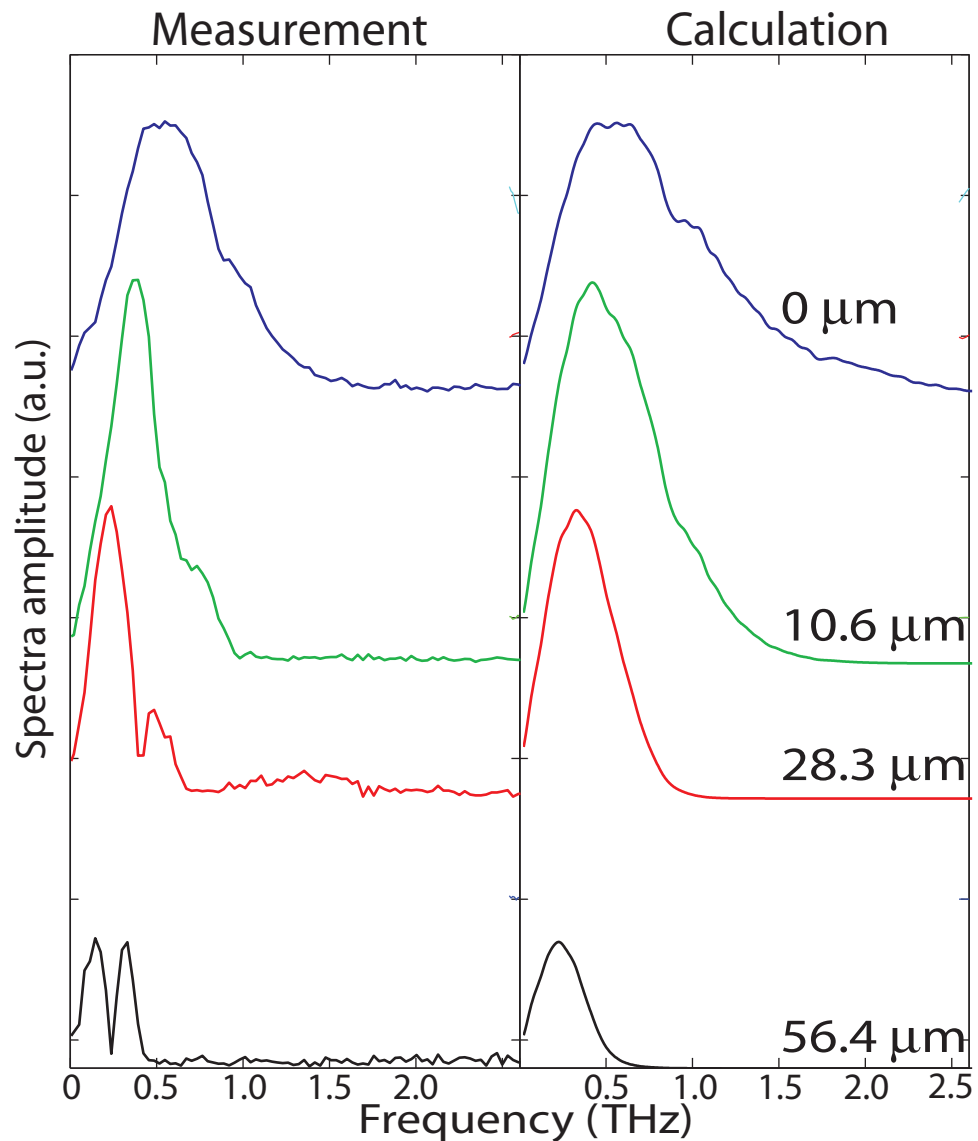
Figure 4.31: Frequency domain comparison between measured and calculated terahertz signal shown in Fig. 4.30. The calculated frequency domain signals were normalized by the peak amplitude of the measurement peak in frequency domain to take into account of the effect of coupling and alignment error. The dips in the measured signals for 28.3 μm and 56.4 μm samples are most likely due to small leakage signal seen in the time domain signals (small high frequency spikes in front of the main spread out pulse) in Fig. 4.30 .

Chapter 5

Conclusions and Future work

5.1 Conclusions

The key contributions of this work are summarized below:

1. We conducted an experimental measurement of the dielectric properties of p+ porous silicon in the terahertz (far infrared) spectral regime. In all cases, the free-standing porous silicon membranes exhibited less absorption than the heavily-doped crystalline silicon from which they were fabricated. However, we observed distinctly different behavior between the freshly-fabricated, hydrogen terminated porous membranes and oxidized porous samples. While freshly-fabricated samples have optical properties that are unstable and change with time, partially oxidized porous silicon samples exhibit excellent stability and almost negligible loss across a broad range of THz frequencies. This result suggests that oxidized porous silicon could serve as a useful and versatile material for fabricating multilayer terahertz devices.

2. We demonstrate that porous silicon could be a convenient and inexpensive platform for building multilayer terahertz devices. As a proof of concept, we fabricated a 13 layer porous silicon Bragg grating targeting center frequency of 1.17 THz. The peak power reflectivity is measured to be 93% with FWHM of 0.26 THz. Residual ab-

sorption of porous silicon is most likely attributed to the phonon confinement effect or scattering, therefore it is possible that lower loss could be achieved by changing the pore size with starting wafer of different doping concentration or by ensuring uniform field distribution in the etching cells. While the Bragg filter presented here used only two different porosities, in principle one could construct arbitrary refractive index profiles by simply adjusting the anodization current density as a function of time. This could enable more complex filters, cavities, antireflection coatings, and even graded-index dielectric waveguides. In comparison with other multilayered filtering techniques for terahertz application, our method has the advantages of simple fabrication procedure and capability of fabricating more sophisticated graded filter.

3. We describe the fabrication and measurement of a new type of terahertz surface plasmon waveguide in which the terahertz mode is guided in a nanoporous silicon layer. We present calculations and measurements of the time-domain response that show the role of modal dispersion and frequency-dependent loss in the propagation. Because of the large internal surface area inherent to porous materials, this structure holds promise for sensor and spectroscopy applications that rely on selective surface binding.

5.2   Future work

Throughout this thesis, we had shown that porous silicon is an interesting optical material for applications in terahertz regime. Our exploration of porous silicon is by no means exhausive and we are only at the beginning phase of exploring this versatile material. Future work is obviously required to fullfill the potential of this promising material. Below we list some of the potential future areas that could prove promising.

1. Improvement on signal to noise of our terahertz system. The current signal to noise of $10^4 - 10^5$, while high enough for experiments described in this thesis, is not suf-

ficient for future work in plasmonic and spectroscopy. In particular, for plasmonic devices, the razor blade coupling method only has an efficiency of $< 10\%$. Hence higher signal to noise of the terahertz system is obviously needed for broadband, high sensitivity application in plasmonic devices. One potential solution is to swith to photoconductive switch based system [192]. The high modulation frequency allowed by photoconductive switch would dramatically reduce $1/f$ noise in the system. Photoconductive based system had been known to have signal to noise ratio as high as $10^7 - 10^9$. Furthermore, the use of photoconductive based system also allow lower optical pump power which would allow diverging large portion of the pump beam for other uses such as optical pump terahertz probe measurement of carrier dynamic in semiconductor.

2. For biological application, the porous silicon surface could be functionalized with biomolecules and be used for label free biomolecular detection [127,129,131]. As the reactivity of the functionalized surface is dependent on the molecule size and the pore size [193], porous silicon of different pore sizes fabricated with silicon of different doping concentrations and types need to be investigated for the terahertz frequency. So far, microporous silicon fabricated from lightly doped p-type silicon had been investigated by Labbe-Lavigne et al [145]. We [194] and Ramani et al. [146] had investigated mesoporous silicon fabricated from highly doped silicon. Macroporous silicon, fabricated with lightly doped n-type silicon with optical illumination is a promising material that has remained uninvestigated.

3. In the application of terahertz filtering, so far we only investigated the passive filtering aspect of porous silicon. As our group demonstrated in Ref. [195], the carrier lifetime in porous silicon is around 200 ps. Hence, it may be possible to develop a fast optical switching terahertz filter by illumination of femtosecond laser pulse on a porous silicon filter or resonance cavity.
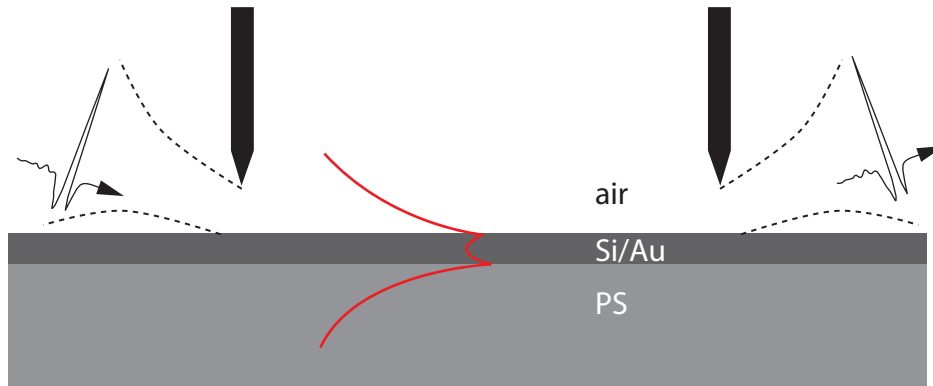
Figure 5.1: Porous silicon based surface plasmon waveguide with thin silicon or metal film.

4. Only porous silicon made from <100> silicon wafer is investigated in this work. By using other crystal orientations such as <110> silicon, it is possible to take advantage of the anisotropic nature of the porous silicon as birefringent filter [140–142]. It is also possible that this birefringence could be enhanced by coating the pores with thin metallic film [196].

5. In Chap. 4, we discussed a surface plasmon waveguide comprised of porous silicon layer on highly doped silicon. We had found that due to the presence of the thin porous silicon layer, the surface plasmon field is confined to the lossy bulk silicon interface. While this increases the confinement of the field near the surface, which is important for spectroscopy purpose, the waveguide also exhibits higher dispersion and absorption in the high frequency regime. In Fig. 5.1, we show an alternative approach with thin silicon or metal in between air and porous silicon. As have been investigated in similar experiment setup in optical domain, this configuration is believe to be low loss due to the thin thickness of the conducting surface [197]. Furthermore, by coupling the surface plasmon wave from the air side, the side with porous silicon becomes less mechanically restricted and could be filled with liquid without disturbing the experiment setup, which in turn allows for consistent coupling conditions for comparison between biomolecules filled and unfilled porous silicon.

6. Manipulation of terahertz coupled surface plasmon is of great interest. By patterning

the surface of a surface plasmon supporting device, the surface plasmon could be redirected, filtered and split in compact device [198, 199]. Porous silicon could be easily patterned [200–206] by laser-assisted oxidation after etching or lithographic pattern before etching. Hence porous silicon could potentially be versatile platform for exploring surface plasmon based devices.

Reference

[1] Daniel M. Mittleman, Rune H. Jacobsen, and Martin C. Nuss. T-ray imaging. *IEEE J. Sel. Top. Quantum Electron.*, 2(3):679–692, September 1996.

[2] Peter H. Siegel. Terahertz technology. *IEEE Transaction on Microwave Theory and Techniques*, 50(3):910–928, March 2002.

[3] Kiyomi Sakai. *Terahertz optoelectronics*. Springer, 2005.

[4] J. M. Chamberlain and R.E. Miles. *New directions in terahertz technology*. Kluwer Academic Publishers, 1997.

[5] E. R. Brown. Thz generation by photomixing in ultrafast photoconductors. *Int. J. High Speed Electron. Syst.*, 13(2):147–195, 2003.

[6] Daniel van der Weide. Applications and outlook for electronics terahertz technology. *Optics&Photonics News*, pages 48–53, April 2003.

[7] Jie Shan and Tony F. Heinz. *Ultrafast dynamical processes in semiconductors topics appl. phys.*, chapter Terahertz Radiation from Semiconductors, pages 1–59. Springer-Verlag Berlin Heidelberg, 2004.

[8] D. H. Auston, K. P. Chueng, and P. R. Smith. Picosecond photoconducting hertzian dipoles. *Appl. Phys. Lett*, 45:284–286, 1984.

[9] G. Mourou, C. V. Stancampiano, A. Antonetti, and A. Orszag. Picosecond microwave pulses generated with a sub-picosecond laser driven semiconductor switch. *Appl. Phys. Lett*, 39:295–296, 1981.

[10] P. R. Smith, D. H. Auston, and Martin C. Nuss. Subpicosecond photoconducting dipole antennas. *IEEE J. Quantum Electron.*, 24:255–260, 1988.

[11] D. H. Auston. *Ultrashort laser pulses*, chapter Ultrafast optoelectronics. Springer, Berlin, Heidelberg, 1993.

[12] D. R. Grischkowsky. *Frontiers in Nonlinear Optics*, chapter Nonlinear generation of sub-psec pulses of THz electromagnetic radiation by optoelectronics-application to time-domain spectroscopy. Institute of Physics, 1993.

[13] W. M. Robertson. *Optoelectronics techniques for microwave and milimeter wave engineering*. Artech House, Boston, 1995.

[14] Q. Chen, M. Tani, Z. Jiang, and X.-C. Zhang. Electro-optic transceivers for terahertz-wave applications. *J. Opt. Soc. Am. B*, 18(6):823–831, June 2001.

[15] M. Nagai, K. Tanaka, H. Ohtake, T. Bessho, T. Sugiura, and M. Hirosumi, T. Yoshida. Generation and detection of terehertz radiation by electro-optical process in gaas using $1.56\mu m$ fiber laser pulses. *Appl. Phys. Lett*, 85(18):3974–3976, 2004.

[16] Ping Gu and Masahiko Tani. *Terahertz optoelectronics*, chapter Terahertz radiation from semiconductor surfaces, pages 63–97. Springer, 2005.

[17] Ping Gu, Masahiko Tani, Shunsuke Kono, Kiyomi Sakai, and X.-C. Zhang. Study of terahertz radiation from inas and insb. *J. Appl. Phys.*, 91(9):55335537, May 2002.

[18] H. Ohtake, S. Ono, M. Sakai, Z. L. Liu, T. Tsukamoto, and N. Sarukura. Saturation of thz-radiation power from femtosecond-laser-irradiated inas in a high magnetic field. *Appl. Phys. Lett*, 76:1398, 2000.

[19] N. Sarukura, H. Ohtake, S. Izumida, and Z. L. Liu. High average-power thz radiation from femtosecond laser-irradiated inas in a magnetic field and its elliptical polarization characteristics. *J. Appl. Phys. Lett.*, 84:654, 1998.

[20] M. Nakajima, K. Uchida, M. Tani, and M. Hangyo. Strong enhancement of terahertz radiation from semiconductor surfaces using mgo hemispherical lens coupler. *Appl. Phys. Lett.*, 85:191–193, 2004.

[21] Peter U. Jepsen, Uffe Meller, Finn Etchhorn, Hannes Merbold, Jacob R. Folenberg, and Stewart Clark. Terahertz time-domain spectroscopy of crystalline and aqueous system. In *Proceeding of CLEO/QELS*, 2007.

[22] Gian Piero Gallerano. Thz-bridge. Technical report, ENEA, 2004.

[23] Amnon Yariv. *Optical Electronics in Modern Communications*. Oxford University Press, USA, 5 edition, March 1997.

[24] Shu-Zee A. Lo and Thomas E. Murphy. Nanoporous silicon multilayers for terahertz filtering. *Optics Letters*, 34(19):2921–2923, October 2009.

[25] G. Gallot, S. P. Jamison, R. W. McGowan, and D. Grischkowsky. Terahertz waveguides. *J. Opt. Soc. Am. B*, 17(5):851–863, May 2000.

[26] Chao-Yuan Chen, Ci-Ling Pan, Cho-Fan Hsieh, Yea-Feng Lin, and Ru-Pin Pan. Liquid-crystal-based terahertz tunable lyot filter. *Appl. Phys. Lett.*, 88(10):101107, 2006.

[27] Chao-Yuan Chen, Cho-Fan Hsieh, Yea-Feng Lin, Ru-Pin Pan, and Ci-Ling Pan. Magnetically tunable room-temperature 2 pi liquid crystal terahertz phase shifter. *Opt. Express*, 12(12):2625–2630, June 2004.

[28] Chao-Yuan Chen, Tsong-Ru Tsai, Ci-Ling Pan, and Ru-Pin Pan. Room temperature terahertz phase shifter based on magnetically controlled birefringence in liquid crystals. *Appl. Phys. Lett.*, 83(22):4497, 2003.

[29] L Fekete, F. Kadlec, H Nemec, and P. Kužel. Fast one-dimensional photonic crystal modulators for the terahertz range. *Opt. Express*, 15(14):8898–8912, July 2007.

[30] L. Fekete, F. Kadlec, P. Kužel, and H. Němec. Ultrafast opto-terahertz photonic crystal modulator. *Opt. Lett.*, 32(6):680–682, March 2007.

[31] Cho-Fan Hsieh, Ru-Pin Pan, Tsung-Ta Tang, Hung-Lung Chen, and Ci-Ling Pan. Voltage-controlled liquid-crystal terahertz phase shifter and quarter-wave plate. *Opt. Lett.*, 31(8):1112–1114, April 2006.

[32] Maleki A. R. Javan and N. Granpayeh. Fast terahertz wave Switch/Modulator based on photonic crystal structures. *J ELECTROMAGNET WAVE*, 23(2):203–212, 2009.

[33] P Kužel and F Kadlec. Tunable structures and modulators for THz light. *C. R. Phys.*, 9(2):197–214, 2008.

[34] K. C. Lim, J. D. Margerum, and A. M. Lackner. Liquid crystal millimeter wave electronic phase shifter. *Appl. Phys. Lett.*, 62(10):1065, 1993.

[35] P. Mounaix, E. Freysz, J. Degert, N. Daro, J.-F. Létard, P. Kužel, V. Vigneras, and L. Oyenhart. One-dimensional tunable photonic crystals with spin crossover material for the terahertz range. *Appl. Phys. Lett.*, 89(17):174105, 2006.

[36] S Savel'ev, A Rakhmanov, and F Nori. Tunable photonic crystal for THz radiation in layered superconductors: Strong magnetic-field dependence of the transmission coefficient. *Physica C: Superconductivity*, 445-448:180–182, 2006.

[37] Sergey Savel'ev, A. L. Rakhmanov, and Franco Nori. Josephson vortex lattices as scatterers of terahertz radiation: Giant magneto-optical effect and doppler effect using terahertz tunable photonic crystals. *Phys. Rev. B*, 74(18):184512, November 2006.

[38] Sergey Savel'ev, A. Rakhmanov, and Franco Nori. Using josephson vortex lattices to control terahertz radiation: Tunable transparency and terahertz photonic crystals. *Phys. Rev. Lett.*, 94(15):157004, 2005.

[39] Abul K. Azad, Hou-Tong Chen, Satish R. Kasarla, Antoinette J. Taylor, Zhen Tian, Xinchao Lu, Weili Zhang, Hong Lu, Arthur C. Gossard, and John F. O'Hara. Ultrafast optical control of terahertz surface plasmons in subwavelength hole arrays at room temperature. *Appl. Phys. Lett.*, 95(1):011105, 2009.

[40] J. Gómez Rivas, M. Kuttge, H. Kurz, P. Haring Bolivar, and J. A. Sánchez-Gil. Low-frequency active surface plasmon optics on semiconductors. *Appl. Phys. Lett.*, 88(8):082106–3, February 2006.

[41] J. Gómez Rivas, P. Haring Bolivar, and H. Kurz. Thermal switching of the enhanced transmission of terahertz radiationthrough subwavelength apertures. *Opt. Lett.*, 29(14):1680–1682, July 2004.

[42] E. Hendry, F. Garcia-Vidal, L. Martin-Moreno, J. Rivas, M. Bonn, A. Hibbins, and M. Lockyear. Optical control over Surface-Plasmon-Polariton-Assisted THz transmission through a slit aperture. *Phys. Rev. Lett.*, 100(12):123901, 2008.

[43] C. Janke, J. Gómez Rivas, P. Haring Bolivar, and H. Kurz. All-optical switching of the transmission of electromagnetic radiation through subwavelength apertures. *Opt. Lett.*, 30(18):2357–2359, 2005.

[44] Hou-Tong Chen, Willie J. Padilla, Joshua M. O. Zide, Arthur C. Gossard, Antoinette J. Taylor, and Richard D. Averitt. Active terahertz metamaterial devices. *Nature*, 444(7119):597–600, November 2006.

[45] Hou-Tong Chen, Willie J. Padilla, Michael J. Cich, Abul K. Azad, Richard D. Averitt, and Antoinette J. Taylor. A metamaterial solid-state terahertz phase modulator. *Nature Photon.*, 3(3):148–151, 2009.

[46] H.-T. Chen, W.J. Padilla, J.M.O. Zide, S.R. Bank, A.C. Gossard, A.J. Taylor, and R.D. Averitt. Ultrafast optical switching of terahertz metamaterials fabricated on ErAs/GaAs nanoisland superlattices. *Opt. Lett.*, 32(12):1620–1622, 2007.

[47] Natsuki Kanda, Kuniaki Konishi, and Makoto Kuwata-Gonokami. Light-induced terahertz optical activity. *Opt. Lett.*, 34(19):3000–3002, October 2009.

[48] J.-M. Manceau, N.-H. Shen, M. Kafesaki, C. M. Soukoulis, and S. Tzortzakis. Dynamic response of metamaterials in the terahertz regime: Blueshift tunability and broadband phase modulation. *Appl. Phys. Lett.*, 96(2):021111, 2010.

[49] K.R. Armstrong and F.J. Low. Far-infrared filters utilizing small particle scattering and antireflection coatings. *Appl. Opt.*, 13(2):425–430, 1974.

[50] K. R. Armstrong and F. J. Low. New techniques for Far-Infrared filters. *Appl. Opt.*, 12(9):2007–2009, 1973.

[51] A. F. Turner, L. Chang, and T. P. Martin. Enhanced reflectance of reststrahlen reflection filters. *Appl. Opt.*, 4(8):927–933, 1965.

[52] H. Nemec, P. Kuzel, L. Duvillaret, A. Pashkin, M. Dressel, and M.T. Sebastian. Highly tunable photonic crystal filter for the terahertz range. *Opt. Lett.*, 30(5):549–551, 2005.

[53] Hynek Nemec, P. Kuzel, Frederic Garet, and Lionel Duvillaret. Time-domain terahertz study of defect formation in one-dimensional photonic crystals. *Appl. Opt.*, 43(9):1965–1970, 2004.

[54] A. J. Gallant, M. A. Kaliteevski, D. Wood, M. C. Petty, R. A. Abram, S. Brand, G. P. Swift, D. A. Zeze, and J. M. Chamberlain. Passband filters for terahertz radiation based on dual metallic photonic structures. *Appl. Phys. Lett.*, 91(16):161115, 2007.

[55] M. A. Kaliteevski, S. Brand, J. Garvie-Cook, R. A. Abram, and J. M. Chamberlain. Terahertz filter based on refractive properties ofmetallic photonic crystal. *Opt. Express*, 16(10):7330–7335, May 2008.

[56] Benjamin Reinhard, Garik Torosyan, and René Beigang. Band structure of terahertz metallic photonic crystals with high metal filling factor. *Appl. Phys. Lett.*, 92(20):201107, 2008.

[57] Yuguang Zhao and Daniel R. Grischkowsky. 2-D terahertz metallic photonic crystals in Parallel-Plate waveguides. *IEEE Trans. Microwave Theory Tech.*, 55(4):656–663, 2007.

[58] Dongmin Wu, Nicholas Fang, Cheng Sun, Xiang Zhang, Willie J. Padilla, Dimitri N. Basov, David R. Smith, and Sheldon Schultz. Terahertz plasmonic high pass filter. *Appl. Phys. Lett.*, 83(1):201, 2003.

[59] A. J. Gallant, M. A. Kaliteevski, S. Brand, D. Wood, M. Petty, R. A. Abram, and J. M. Chamberlain. Terahertz frequency bandpass filters. *J. Appl. Phys.*, 102(2):023102, 2007.

[60] E. Özbay, E. Michel, G. Tuttle, R. Biswas, K. M. Ho, J. Bostak, and D. M. Bloom. Terahertz spectroscopy of three-dimensional photonic band-gap crystals. *Opt. Lett.*, 19(15):1155–1157, 1994.

[61] E. Özbay, E. Michel, G. Tuttle, R. Biswas, K. M. Ho, J. Bostak, and D. M. Bloom. Double-etch geometry for millimeter-wave photonic band-gap crystals. *Appl. Phys. Lett.*, 65(13):1617, 1994.

[62] Kenta Takagi and Akira Kawasaki. Fabrication of three-dimensional terahertz photonic crystals with diamond structure by particle manipulation assembly. *Appl. Phys. Lett.*, 94(2):021110, 2009.

[63] Amit Agrawal, Hua Cao, and Ajay Nahata. Excitation and scattering of surface plasmon-polaritons on structured metal films and their application to pulse shaping and enhanced transmission. *New J. Phys*, 7:249, 2005.

[64] Abul K. Azad, Y. Zhao, and W. Zhang. Transmission properties of terahertz pulses through an ultrathin subwavelength silicon hole array. *Appl. Phys. Lett.*, 86(14):141102–3, April 2005.

[65] J. Gómez Rivas, C. Schotsch, P. Haring Bolivar, and H. Kurz. Enhanced transmission of THz radiation through subwavelength holes. *Phys. Rev. B*, 68(20):201306, 2003.

[66] Jaime Gómez Rivas, Christof Janke, Peter Bolivar, and Heinrich Kurz. Transmission of THz radiation through InSb gratings of subwavelength apertures. *Opt. Express*, 13(3):847–859, February 2005.

[67] M Nazarov, F Garet, D Armand, A Shkurinov, and J Coutaz. Surface plasmon THz waves on gratings. *C. R. Phys.*, 9(2):232–247, 2008.

[68] R. D. Rawcliffe and C. M. Randall. Metal mesh interference filters for the far infrared. *Appl. Opt.*, 6(8):1353–1358, 1967.

[69] K. F. Renk and L. Genzel. Interference filters and Fabry-Perot interferometers for the far infrared. *Appl. Opt.*, 1(5):643–648, 1962.

[70] Reinhard Ulrich. Interference filters for the far infrared. *Appl. Opt.*, 7(10):1987–1996, October 1968.

[71] S. P. Varma and K. D. Möller. Far infrared interference filters. *Appl. Opt.*, 8(8):1663–1666, 1969.

[72] D. A. Weitz and W. J. Skocpol. Capacitive-mesh output couplers for optically pumped far-infrared lasers. *Opt. Lett.*, 3(1):13–15, July 1978.

[73] C. Winnewisser, F.T. Lewen, M. Schall, M. Walther, and H. Helm. Characterization and application of dichroic filters in the 0.1-3-THz region. *IEEE Trans. Microwave Theory Tech.*, 48(4):744–749, 2000.

[74] C. Winnewisser, F. Lewen, and H. Helm. Transmission characteristics of dichroic filters measured by THz time-domain spectroscopy. *Appl. Phys. A.*, 66(6):593–598, June 1998.

[75] Carsten Winnewisser, Frank Lewen, Jochen Weinzierl, and Hanspeter Helm. Transmission features of Frequency-Selective components in the far infrared determined by terahertz Time-Domain spectroscopy. *Appl. Opt.*, 38(18):3961–3967, June 1999.

[76] Yong Ma, A. Khalid, Timothy D. Drysdale, and David R. S. Cumming. Direct fabrication of terahertz optical devices on low-absorption polymer substrates. *Opt. Lett.*, 34(10):1555–1557, May 2009.

[77] Arline M. Melo, Mariano A. Kornberg, Pierre Kaufmann, Maria H. Piazzetta, Em???lio C. Bortolucci, Maria B. Zakia, Otto H. Bauer, Albrecht Poglitsch, and Alexandre M. P. Alves da Silva. Metal mesh resonant filters for terahertz frequencies. *Appl. Opt.*, 47(32):6064–6069, November 2008.

[78] Frank Baumann, Jr. Bailey, Ahmer Naweed, William D. Goodhue, and Andrew J. Gatesman. Wet-etch optimization of free-standing terahertz frequency-selective structures. *Opt. Lett.*, 28(11):938–940, June 2003.

[79] M.E. MacDonald, A. Alexanian, R.A. York, Z. Popovic, and E.N. Grossman. Spectral transmittance of lossy printed resonant-grid terahertz bandpass filters. *IEEE Trans. Microwave Theory Tech.*, 48(4):712–718, 2000.

[80] K. D. Möller, J. B. Warren, J. B. Heaney, and C. Kotecki. Cross-shaped bandpass filters for the near- and mid-infrared wavelength regions. *Appl. Opt.*, 35(31):6210–6215, November 1996.

[81] D. W. Porterfield, J. L. Hesler, R. Densing, E. R. Mueller, T. W. Crowe, and R. M. Weikle II. Resonant metal-mesh bandpass filters for the far infrared. *Appl. Opt.*, 33(25):6046–6052, 1994.

[82] Takeshi Tanaka, Masamichi Akazawa, and Eiichi Sano. Terahertz wave filter from cascaded Thin-Metal-Film meshes with a triangular array of hexagonal holes. *Jpn. J. Appl. Phys.*, 43(No. 2B):L287–L289, 2004.

[83] S. Biber, M. Bozzi, O. Gunther, L. Perregrini, and L.-P. Schmidt. Design and testing of Frequency-Selective surfaces on silicon substrates for Submillimeter-Wave applications. 54(9):2638–2645, 2006.

[84] R. Dickie, R. Cahill, H.S. Gamble, V.F. Fusco, B. Moyna, P.G. Huggard, N. Grant, and C. Philpot. Micromachined 300 ghz high q resonant slot frequency selective surface filter. *IEE Proceedings - Microwaves, Antennas and Propagation*, 151(1):31, 2004.

[85] Peter A. Krug, David H. Dawes, Ross C. McPhedran, W. Wright, John C. Macfarlane, and Lewis B. Whitbourn. Annular-slot arrays as far-infrared bandpass filters. *Opt. Lett.*, 14(17):931–933, 1989.

[86] B. Monacelli, J.B. Pryor, B.A. Munk, D. Kotter, and G.D. Boreman. Infrared frequency selective surface based on circuit-analog square loop design. 53(2):745–752, 2005.

[87] Hou-Tong Chen, John F. O'Hara, Antoinette J. Taylor, Richard D. Averitt, C. Highstrete, Mark Lee, and Willie J. Padilla. Complementary planar terahertz metamaterials. *Opt. Express*, 15(3):1084–1095, FEB 5 2007.

[88] John F. O'Hara, Evgenya Smirnova, Hou-Tong Chen, Antoinette J. Taylor, Richard D. Averitt, Clark Highstrete, Mark Lee, and Willie J. Padilla. Properties of planar electric metamaterials for novel terahertz applications. *JOURNAL OF NANOELECTRONICS AND OPTOELECTRONICS*, 2(1):90–95, APR 2007.

[89] Hu Tao, A. C. Strikwerda, K. Fan, C. M. Bingham, W. J. Padilla, Xin Zhang, and R. D. Averitt. Terahertz metamaterials on free-standing highly-flexible polyimide substrates. *JOURNAL OF PHYSICS D-APPLIED PHYSICS*, 41(23):232004, DEC 7 2008.

[90] X. G. Peralta, M. C. Wanke, C. L. Arrington, J. D. Williams, I. Brener, A. Strikwerda, R. D. Averitt, W. J. Padilla, E. Smirnova, A. J. Taylor, and J. F. O'Hara. Large-area metamaterials on thin membranes for multilayer and curved applications at terahertz and higher frequencies. *Appl. Phys. Lett.*, 94(16):161113, APR 20 2009.

[91] Christoph R. Englert, Manfred Birk, and Hansjorg Maurer. Antireflection coated, wedged, Single-Crystal silicon aircraft window for the Far-Infrared. 37(4):1997–2003, October 1998.

[92] A.J. Gatesman, J. Waldman, M. Ji, C. Musante, and S. Yngvesson. An Anti-Reflection coating for silicon optics at terahertz frequencies. 10(7):264–266, July 2000.

[93] Iwao Hosako. Antireflection coating formed by plasma-enhanced chemical-vapor deposition for terahertz-frequency germanium optics. *Appl. Opt.*, 42(19):4045–4048, 2003.

[94] Judy Lau, Joseph Fowler, Tobias Marriage, Lyman Page, Jon Leong, Edward Wishnow, Ross Henry, Ed Wollack, Mark Halpern, Danica Marsden, and Gaelen Marsden. Millimeter-wave antireflection coating for cryogenic silicon lenses. *Appl. Opt.*, 45(16):3746–3751, June 2006.

[95] Kodo Kawase and Norihisa Hiromoto. Terahertz-wave antireflection coating on ge and GaAs with fused quartz. *Appl. Opt.*, 37(10):1862–1866, April 1998.

[96] Kodo Kawase, Norihisa Hiromoto, and Mikio Fujiwara. Terahertz-Wave antireflection coating on ge wafer using optical lapping method. *Electronics and Communications in Japan*, 83(3):10–15, 2000.

[97] W Withayachumnankul, B Fischer, and D Abbott. Quarter-wavelength multilayer interference filter for terahertz waves. *Opt. Commun.*, 281(9):2374–2379, 2008.

[98] W Withayachumnankul, B. M. Fischer, S. P. Mickan, and D. Abbott. T-ray multilayer interference filter. *Infrared and Millimeter Waves 2007 and the 2007 15th International Conference on Terahertz Electronics. IRMMW-THz*, pages 307–308, 2007.

[99] Robert Schiwon, Gerhard Schwaab, Erik Brundermann, and Martina Havenith. Far-infrared multilayer mirrors. *Appl. Phys. Lett.*, 83(20):4119, 2003.

[100] Todd W. Du Bosq, Andrey V. Muravjov, Robert E. Peale, and Christopher J. Fredricksen. Multilayer silicon cavity mirrors for the far-infrared p-Ge laser. *Appl. Opt.*, 44(33):7191–7195, November 2005.

[101] Iwao Hosako. Multilayer optical thin films for use at terahertz frequencies: method of fabrication. *Appl. Opt.*, 44(18):3769–3773, June 2005.

[102] Naoki Matsumoto, Takuji Nakagawa, Keisuke Kageyama, Nobuyuki Wada, and Yukio Sakabe. Terahertz Band-Pass filter fabricated by multilayer ceramic technology. *Jpn. J. Appl. Phys.*, 45(9B):7499–7502, 2006.

[103] Frank Rutz, Martin Koch, Lorenzo Micele, and Goffredo de Portu. Ceramic dielectric mirrors for the terahertz range. *Appl. Opt.*, 45(31):8070–8073, 2006.

[104] D. Turchinovich, A. Kammoun, P. Knobloch, T. Dobbertin, and M. Koch. Flexible all-plastic mirrors for the THz range. *Appl. Phys. A.*, 74(2):291–293, 2002.

[105] Ibraheem A. Ibraheem, Norman Krumbholz, Daniel Mittleman, and Martin Koch. Low-Dispersive dielectric mirrors for future wireless terahertz communication systems. 18(1):67–69, 2008.

[106] N. Krumbholz, K. Gerlach, F. Rutz, M. Koch, R. Piesiewicz, T. Kurner, and D. Mittleman. Omnidirectional terahertz mirrors: A key element for future terahertz communication systems. *Appl. Phys. Lett.*, 88(20):202905, 2006.

[107] Christian Jansen, Frank Neubauer, Jens Helbig, and Daniel M. Mittleman. Flexible bragg reflectors for the terahertz regime composed of polymeric compounds. *Infrared and Millimeter Waves 2007 and the 2007 15th International Conference on Terahertz Electronics. IRMMW-THz*, pages 984–986, 2007.

[108] Joseph Lott, Chen Xia, Louis Kosnosky, Christoph Weder, and Jie Shan. Terahertz photonic crystals based on barium Titanate/Polymer nanocomposites. *Adv. Mat.*, 20:3649–3653, 2008.

[109] Jianxin Shao and J. A. Dobrowolski. Multilayer interference filters for the far-infrared and submillimeter regions. *Appl. Opt.*, 32(13):2361–2370, May 1993.

[110] Kai Liu, Jingzhou Xu, Tao Yuan, and X.-C. Zhang. Terahertz radiation from InAs induced by carrier diffusion and drift. *Physical Review B*, 73(15):155330, April 2006.

[111] R. Alan Cheville and D. Grischkowsky. Observation of pure rotational absorption spectra in the v2 band of hot h_2o in flames. *Optics Letters*, 23(7):531–533, April 1998.

[112] P. C. Searson and J. M. Macaulay. The fabrication of porous silicon structures. *Nanotechnology*, 3:188–191, 1992.

[113] R. L. Smith and S. D. Collins. Porous silicon formation mechanisms. *J. Appl. Phys.*, 71:R1–R22, 1992.

[114] U. Grüning, V. Lehmann, S. Ottow, and K. Busch. Macroporous silicon with a complete two-dimensional photonic band gap centered at 5 μm. *Applied Physics Letters*, 68(6):747, 1996.

[115] J. Schilling, F. Müller, S. Matthias, R. B. Wehrspohn, U. Gösele, and K. Busch. Three-dimensional photonic crystals based on macroporous silicon with modulated pore diameter. *Applied Physics Letters*, 78(9):1180, 2001.

[116] Stephen E. Lewis, John R. DeBoer, James L. Gole, and Peter J. Hesketh. Sensitive, selective, and analytical improvements to a porous silicon gas sensor. *Sensors and Actuators B: Chemical*, 110(1):54–65, September 2005.

[117] Luca Boarino, C. Baratto, F. Geobaldo, G. Amato, E. Comini, A. M. Rossi, G. Faglia, G. Lérondel, and G. Sberveglieri. NO2 monitoring at room temperature by a porous silicon gas sensor. *Materials Science and Engineering B*, 69-70:210–214, 2000.

[118] Z. M. Rittersma, A. Splinter, A. Bödecker, and W. Benecke. A novel surface-micromachined capacitive porous silicon humidity sensor. *Sensors and Actuators B: Chemical*, 68(1-3):210–217, August 2000.

[119] Lenward Seals, James L. Gole, Laam Angela Tse, and Peter J. Hesketh. Rapid, reversible, sensitive porous silicon gas sensor. *Journal of Applied Physics*, 91(4):2519, 2002.

[120] Monuko du Plessis. Nanoporous silicon explosive devices. *Materials Science and Engineering: B*, 147(2-3):226–229, February 2008.

[121] Monuko du Plessis. Properties of porous silicon nano-explosive devices. *Sensors and Actuators A: Physical*, 135(2):666–674, April 2007.

[122] U. Gosele and V. Lehmann. *Porous Silicon*, chapter Porous silicon quantum sponge structures formation mechanism, preparation methods and some properties, pages 17–40. World Scientific, 1994.

[123] T E Bell, P T J Gennissen, D DeMunter, and M Kuhl. Porous silicon as a sacrificial material. *Journal of Micromechanics and Microengineering*, 6(4):361, December 1996.

[124] G. Kaltsas and A. G. Nassiopoulos. Bulk silicon micromachining using porous silicon sacrificial layers. *Microelectron. Eng.*, 35(1-4):397–400, 1997.

[125] W. Kronast, B. M??ller, W. Siedel, and A. Stoffel. Single-chip condenser microphone using porous silicon as sacrificial layer for the air gap. *Sensors and Actuators A: Physical*, 87(3):188–193, 2001.

[126] M. Arroyo-Hernandez, Martin-Palma R. J, V. Torres-Costa, and J. M. Martinez Duart. Porous silicon optical filters for biosensing applications. *J. Non-Crystalline Solids*, 352:2457–2460, 2006.

[127] Keiki-Pua S. Dancil, Douglas P. greiner, and Michael J. Sailor. A porous silicon optical biosensor: detection of reversible binding of igg to a protein a-modified surface. *J. Am. Chem. Soc.*, 121:7925–7930, 1999.

[128] Luca De Stefano, I. Rea, Ivo Rendina, L. Rotiroti, Andrea Mario Rossi, and S. D'Auria. Resonant cavity enhanced optical microsensor for molecular interactions based on porous silicon. *Phys. Status Solidi A*, 203:886–891, 2006.

[129] Victor S.-Y Lin, Kianoush Motesharei, Keiki-Pua S. Dancil, Michael J. Sailor, and M. Reza Ghadiri. A porous silicon-based optical interferometric biosensor. *Science*, 278:840–843, 1997.

[130] Luca De Stefano, Ivo Rendina, Luigi Moretti, Stefania Tundo, and Andrea Mario Rossi. Smart optical sensors for chemical substances based on porous silicon technology. *Appl. Opt.*, 43:167–172, 2004.

[131] L. Tay, N. L. Rowell, D. J. Lockwood, and R. Boukherroub. In situ monitoring of protein adsorption on functionalized porous si surfaces. *J. Vac. Sci. Technol. A*, 24:747–751, 2006.

[132] M. G. Berger, C. M. Thonissen, L. Vescan, H. Luth, and H. Munder. Porosity superlattices: a new class of si heterostructures. *J. Phys. D: Appl. Phys.*, 27(6):1333–1336, 1994.

[133] S. Frohnhoff and M. G. M. G. Berger. Porous silicon superlattices. *Adv. Mater.*, 6(12):963–965, 2004.

[134] D. E. Aspnes and J. B. Theeten. Investigation of effective -medium models of microscopic surface roughness by spectroscopic ellipsometry. *Phys. Rev. B*, 20:3292–3302, 1979.

[135] J. E. Spanier and I. P. Herman. Use of hybrid phenomenological and statistical effective-medium theories of dielectric functions to model the infrared reflectance of porous SiC films. *Phys. Rev. B*, 61:10437–10450, 2000.

[136] E. Lorenzo, C. J. Oton, N. E. Capuj, M. Ghulinyan, D. Navarro-Urrios, Z. Gaburro, and L. Pavesi. Fabrication and optimization of rugate filters based on porous silicon. *Phys. Stat. Sol. (c)*, 2(9):3227–3231, 2005.

[137] Eduardo Lorenzo, Claudio J. Oton, Nestor E. Capuj, Mher Ghulinyan, Daniel Navarro-Urrois, Zeno Gaburro, and Lorenzo Pavesi. Porous silicon-based rugate filters. *Applied Optics*, 44(26):5415–5421, 2005.

[138] M. Qian, X. O. Bao, L. W. Wang, X. Lu, L. Shao, and X. S. Chen. Structural tailoring of multilayer porous silicon for photonic crystal application. *J. Crystal Growth*, 292:347–350, 2006.

[139] M. S. Salem, M. J. Sailor, T. Sakka, and Y. H. Ogata. Electrochemical preparation of a rugate filter in silicon and its deviation from the ideal structure. *J. Appl. Phys.*, 101:063503, 2007.

[140] J. Diener, N. Künzner, D. Kovalev, E. Gross, V. Yu. Timoshenko, G. Polisski, and F. Koch. Dichroic bragg reflectors based on birefringent porous silicon. *Applied Physics Letters*, 78(24):3887, 2001.

[141] J. Diener, N. Künzner, D. Kovalev, E. Gross, F. Koch, and M. Fujii. Dichroic behavior of multilayer structures based on anisotropically nanostructured silicon. *Journal of Applied Physics*, 91(10):6704, 2002.

[142] V. Timoshenko, L. Osminkina, A. Efimova, L. Golovan, P. Kashkarov, D. Kovalev, N. Künzner, E. Gross, J. Diener, and F. Koch. Anisotropy of optical absorption in birefringent porous silicon. *Physical Review B*, 67(11):113405, 2003.

[143] Didier Hamm, Junji Sasano, Tetsuo Sakka, and Yukio H. Ogata. Silicon anodization in hf ethanoic solutions. *J. Electrochem. Soc.*, 149:C331–C337, 2002.

[144] Didier Hamm, Tetsuo Sakka, and Yukio H. Ogata. Etching of porous silicon in basic solution. *Phys. Status Solidi A*, 197:175–179, 2003.

[145] S. Labbe-Lavigne, S. Barret, F. Garet, L. Duvillaret, and J.-L. Coutaz. Far-infrared dielectric constant of porous silicon layers measured by terahertz time-domain spectroscopy. *J. Appl. Phys.*, 83(11):6007–6010, June 1998.

[146] S. Ramani, Alan Cheville, J. Escorcia Garcia, and V. Agarwal. Conductivity of free-standing porous silicon layers using terahertz differential time-domain spectroscopy. *Phys. Stat. Sol. c*, 4(6):2111–2115, 2007.

[147] A. M. Campos, J. Torres, and J.J. Giraldo. POROUS SILICON DIELECTRIC FUNCTION MODELING FROM EFFECTIVE MEDIUM THEORIES. *Surf. Rev. Lett.*, 9(5-6):1631–1635, 2002.

[148] Peter Yu and Manuel Cardona. *Fundamentals of semiconductors : physics and materials properties*. Springer, Berlin ;;New York, 1996.

[149] F. A. Johnson. Lattice absorption bands in silicon. *Proc. Phys. Soc.*, 73(2):265–272, 1959.

[150] Jianming Dai, Jiangquan Zhang, Weili Zhang, and D. Grischkowsky. Terahertz time-domain spectroscopy characterization of the far-infrared absorption and index of refraction of high-resistivity, float-zone silicon. *J. Opt. Soc. Am. B*, 21(7):1379–1386, July 2004.

[151] A.K.Wan Abdullah, K.A. Maslin, and T.J. Parker. Observation of two-phonon difference bands in the FIR transmission spectrum of si. *Infrared Phys.*, 24(2-3):185–188, May 1984.

[152] C. Jagannath, Z. W. Grabowski, and A. K. Ramdas. Linewidths of the electronic excitation spectra of donors in silicon. *Phys. Rev. B*, 23(5):2082, March 1981.

[153] D. Grischkowsky, Si¿œren Keiding, Martin van Exter, and Ch. Fattinger. Far-infrared time-domain spectroscopy with terahertz beams of dielectrics and semiconductors. *J. Opt. Soc. Am. B*, 7(10):2006–2015, October 1990.

[154] Takeshi Nagashima and Masanori Hangyo. Measurement of complex optical constants of a highly doped si wafer using terahertz ellipsometry. *Appl. Phys. Lett.*, 79(24):3917–3919, December 2001.

[155] S. Nashima, O. Morikawa, K. Takata, and M. Hangyo. Measurement of optical properties of highly doped silicon by terahertz time domain reflection spectroscopy. *Appl. Phys. Lett.*, 79(24):3923–3925, December 2001.

[156] A. G. U. Perera, W. Z. Shen, W. C. Mallard, M. O. Tanner, and K. L. Wang. Far-infrared free-hole absorption in epitaxial silicon films for homojunction detectors. *Appl. Phys. Lett.*, 71(4):515–517, July 1997.

[157] S. K. Ray, T. N. Adam, R. T. Troeger, J. Kolodzey, G. Looney, and A. Rosen. Characteristics of THz waves and carrier scattering in boron-doped epitaxial si and si[sub 1 - x]Ge[sub x] films. *J. Appl. Phys.*, 95(10):5301–5304, May 2004.

[158] Martin van Exter and D. Grischkowsky. Carrier dynamics of electrons and holes in moderately doped silicon. *Phys. Rev. B*, 41(17):12140, June 1990.

[159] Narain D. Arora, John R. Hauser, and David J. Roulston. Electron and hole mobilities in silicon as a function of concentration and temperature. ED-29(2):292–295, February 1982.

[160] Rolfe C. Anderson, Richard S. Muller, and Charles W. Tobias. Chemical surface modification of porous silicon. *J. Electrochem. Soc.*, 140(5):1393–1396, May 1993.

[161] Akhilesh K. Arora, M. Rajalakshmi, T. R. Ravindran, and V. Sivasubramanian. Raman spectroscopy of optical phonon confinement in nanostructured materials. *J. Raman Spectrosc.*, 38(6):604–617, 2007.

[162] I.H. Campbell and P.M. Fauchet. The effects of microcrystal size and shape on the one phonon raman spectra of crystalline semiconductors. *Solid State Commun.*, 58(10):739–741, 1986.

[163] Rajesh Kumar, Yasuo Kitoh, and Kunihiko Hara. Effect of surface treatment on visible luminescence of porous silicon: Correlation with hydrogen and oxygen terminators. *Appl. Phys. Lett.*, 63(22):3032–3034, November 1993.

[164] R Kumar and A Shukla. Temperature dependent phonon confinement in silicon nanostructures. *Phys. Lett. A*, 373(1):133–135, 2008.

[165] A. K. Sood, K. Jayaram, and D. Victor S. Muthu. Raman and high-pressure photoluminescence studies on porous silicon. *J. Appl. Phys.*, 72(10):4963–4965, November 1992.

[166] Douglas B. Mawhinney, John A. Glass, and John T. Yates. FTIR study of the oxidation of porous silicon. *The Journal of Physical Chemistry B*, 101(7):1202–1206, February 1997.

[167] V. Timoshenko, Th. Dittrich, V. Lysenko, M. Lisachenko, and F. Koch. Free charge carriers in mesoporous silicon. *Phys. Rev. B*, 64(8):085314, 2001.

[168] J. Salonen, V.-P. Lehto, and E. Laine. Thermal oxidation of free-standing porous silicon films. *Appl. Phys. Lett.*, 70(5):637–639, February 1997.

[169] Shuji Komuro, Takashi Kato, Takitaro Morikawa, Patrick O'Keeffe, and Yoshinobu Aoyagi. Carrier dynamics in oxidized porous silicon. *J. Appl. Phys.*, 80(3):1749–1756, 1996.

[170] Jessica Harper and Michael J. Sailor. Photoluminescence quenching and the photochemical oxidation of porous silicon by molecular oxygen. *Langmuir*, 13:4652–4658, 1997.

[171] M. A. Tischler, R. T. Collins, J. H. Stathis, and J.C. Tsang. Luminescence degradation in porous silicon. *Appl. Phys. Lett.*, 60:639–641, 1992.

[172] J. L. Batstone, M. A. Tischler, and R. T. Collins. Stability of visible luminescence from porous silicon. *Appl. Phys. Lett.*, 62:2667–2669, 1993.

[173] E. S. Zhukova, A. S. Prokhorov, I. E. Spektor, V. A. Karavanskiĭ, N. N. Mel'nik, T. N. Zavaritskaya, and B. P. Gorshunov. Electrodynamic properties of nanoporous silicon in the range from terahertz to infrared frequencies. *Phys. Solid State*, 49(12):2242–2250, 2007.

[174] Rolfe C. Anderson, Richard S. Muller, and Charles W. Tobias. Investigations of the electrical properties of porous silicon. *J. Electrochem. Soc.*, 138(11):3406–3411, November 1991.

[175] M. Ben-Chorin, F. Möller, F. Koch, W. Schirmacher, and M. Eberhard. Hopping transport on a fractal: ac conductivity of porous silicon. *Phys. Rev. B*, 51(4):2199, 1995.

[176] Sophocles Orfanidis. Electromagnetic waves and antennas, February 2008. http://www.ece.rutgers.edu/ orfanidi/ewa/.

[177] Vladimir Kochergin. *Omnidirectional Optical Filters*. Kluwer Academic Publishers, 2003.

[178] Max Born. *Principles of optics : electromagnetic theory of propagation, interference and diffraction of light*. Cambridge University Press, Cambridge, 7. (expanded) ed. edition, 2003.

[179] Jorg Saxler. *Surface Plasmon Polaritons at Terahertz Frequencies on Metal and Semiconductor Surfaces*. Diploma thesis in physics, Aachen University, Aachen, Germany, November 2003.

[180] J. Saxler, J. Gómez Rivas, C. Janke, H. Pellemans, P. Bolívar, and H. Kurz. Time-domain measurements of surface plasmon polaritons in the terahertz frequency range. *Phys. Rev. B*, 69(15):155427, 2004.

[181] A Zayats, I Smolyaninov, and A Maradudin. Nano-optics of surface plasmon polaritons. *Physics Reports*, 408(3-4):131–314, 2005.

[182] John O'Hara, R. Averitt, and A. Taylor. Terahertz surface plasmon polariton coupling on metallic gratings. *Opt. Express*, 12(25):6397–6402, December 2004.

[183] Hideki Hirori, Masaya Nagai, and Koichiro Tanaka. Destructive interference effect on surface plasmon resonance in terahertz attenuated total reflection. *Optics Express*, 13(26):10801–10814, December 2005.

[184] John O'Hara, Richard Averitt, and Antoinette Taylor. Prism coupling to terahertz surface plasmon polaritons. *Optics Express*, 13(16):6117–6126, 2005.

[185] J. Gómez Rivas, M. Kuttge, P. Bolivar, H. Kurz, and J. Sánchez-Gil. Propagation of surface plasmon polaritons on semiconductor gratings. *Phys. Rev. Lett.*, 93(25):256804, 2004.

[186] T. H. Isaac, W. L. Barnes, and E. Hendry. Determining the terahertz optical properties of subwavelength films using semiconductor surface plasmons. *Appl. Phys. Lett.*, 93(24):241115–3, December 2008.

[187] M. Kuttge, H. Kurz, J. Gómez Rivas, J. A. Sánchez-Gil, and P. Haring Bolivar. Analysis of the propagation of terahertz surface plasmon polaritons on semiconductor groove gratings. *J. Appl. Phys.*, 101(2):023707–6, 2007.

[188] M. A. Ordal, Robert J. Bell, Jr Alexander, L. L. Long, and M. R. Querry. Optical properties of fourteen metals in the infrared and far infrared: Al, co, cu, au, fe, pb, mo, ni, pd, pt, ag, ti, v, and w. *Applied Optics*, 24(24):4493–4499, December 1985.

[189] Tae-In Jeon and D. Grischkowsky. THz zenneck surface wave (THz surface plasmon) propagation on a metal sheet. *Applied Physics Letters*, 88(6):061113–3, February 2006.

[190] I. P. Kaminow, W. L. Mammel, and H. P. Weber. Metal-Clad optical waveguides: Analytical and experimental study. *Appl. Opt.*, 13(2):396–405, February 1974.

[191] Amnon Yariv. *Optical Electronics in Modern Communications*. Oxford University Press, 1997.

[192] Martin van Exter, Ch. Fattinger, and D. R. Grischkowsky. Terahertz time-domain spectroscopy of water vapor. *Opt. Lett.*, 14:1128–1130, 1989.

[193] Guoguang Rong and Sharon M. Weiss. Biomolecule size-dependent sensitivity of porous silicon sensors. *physica status solidi (a)*, 206(6):1365–1368, 2009.

[194] Shu-Zee A. Lo, Andrea M. Rossi, and Thomas E. Murphy. Terahertz transmission through p+ porous silicon membranes. *physica status solidi (a)*, 206(6):1273–1277, 2009.

[195] Paveen Apiratikul, Andrea M. Rossi, and Thomas E. Murphy. Nonlinearities in porous silicon optical waveguides at 1550 nm. *Optics Express*, 17(5):3396, 2009.

[196] V. Kochergin, M. Christophersen, and H. Föll. Surface plasmon enhancement of an optical anisotropy in porous silicon/metal composite. *Applied Physics B*, 80(1):81–87, 2004.

[197] J. J. Burke, G. I. Stegeman, and T. Tamir. Surface-polariton-like waves guided by thin, lossy metal films. *Physical Review B*, 33(8):5186, April 1986.

[198] R. J. Bell, C. A. Goben, M. Davarpanah, K. Bhasin, D. L. Begley, and A. C. Bauer. Two-dimensional optics with surface electromagnetic waves. *Applied Optics*, 14(6):1322–1325, June 1975.

[199] H. Ditlbacher, J. R. Krenn, G. Schider, A. Leitner, and F. R. Aussenegg. Two-dimensional optics with surface plasmon polaritons. *Applied Physics Letters*, 81(10):1762, 2002.

[200] Andrea M. Rossi, Giampiero Amato, Vittorio Camarchia, Luca Boarino, and Stefano Borini. High-quality porous-silicon buried waveguide. *Appl. Phys. Lett.*, 78:20, 2001.

[201] Andrea. M. Rossi, Lili Wang, Vytas Reipa, and T. E. Murphy. Porous silicon biosensor for detection of viruses. *Biosensors and Bioelectronics*, 23:741–745, 2007.

[202] Guoguang Rong, Judson D. Ryckman, Raymond L. Mernaugh, and Sharon M. Weiss. Label-free porous silicon membrane waveguide for dna sensing. *Appl. Phys. Lett.*, 93:161109, 2008.

[203] A Loni, L.T. Canham, M.G. Berger, R. Arens-Fischer, H. Munder, H. Luth, H.F. Arrand, and T.M. Benson. Porous silicon multilayer optical waveguides. *Thin Solid Films*, 276:143–146, 1996.

[204] Ilaria Rea, Antigone Marino, Mario Iodice, Giuseppe Coppola, Ivo Rendina, and Luca De Stefano. A porous silicon bragg grating waveguide by direct laser writing. *J. Phys.: Condens. Matter*, 20:365203, 2008.

[205] Guoguang Rong, Ali Najmaie, John E. Sipe, and Sharon M. Weiss. Nanoscale porous silicon waveguide for label-free dna sensing. *Biosens. Bioelectron.*, 23:1572, 2008.

[206] S.M. Weiss, G. Rong, and J.L. Lawrie. Current status and outlook for silicon-based optical biosensors. *Physica*, E 41:1071–1075, 2009.